Fragmentation in frustrated pyrochlore magnets : theory and experiment

Flavien Museur

THÈSE

Pour obtenir le grade de

DOCTEUR DE L'UNIVERSITÉ GRENOBLE ALPES

École doctorale : PHYS - Physique
Spécialité : Physique de la Matière Condensée et du Rayonnement
Unité de recherche : Institut Néel

Fragmentation dans les aimants pyrochlore frustrés : théorie et expérience

Fragmentation in frustrated pyrochlore magnets: theory and experiment

Présentée par :

Flavien MUSEUR

Direction de thèse :

Elsa LHOTEL — Directrice de thèse
Directeur de recherche, CNRS Délégation Alpes

Peter HOLDSWORTH — Co-directeur de thèse
Professeur des Universités, ENS de Lyon

Rapporteurs :

PATRIK HENELIUS
Professeur, KTH Royal Institute of Technology

FRANÇOISE DAMAY
Directeur de recherche, CNRS DELEGATION ILE-DE-FRANCE SUD

Thèse soutenue publiquement le **26 mai 2023**, devant le jury composé de :

PATRIK HENELIUS Professeur, KTH Royal Institute of Technology	Rapporteur
FRANÇOISE DAMAY Directeur de recherche, CNRS DELEGATION ILE-DE-FRANCE SUD	Rapporteure
RADU COLDEA Professeur, University of Oxford	Examinateur
MICHEL KENZELMANN Professeur, Universität Basel	Président
ARNAUD RALKO Maître de conférences HDR, UNIVERSITE GRENOBLE ALPES	Examinateur

Université Grenoble Alpes

PhD thesis

Fragmentation in frustrated pyrochlore magnets: theory and experiment

Author:
Flavien Museur

Supervisors
Peter C. W. Holdsworth

and Elsa Lhotel

Defended on the 26th of May, 2023

Declaration of Authorship

I declare that the work presented here is original and the result of my own investigations.
Formulations, ideas or pictures taken from other sources are cited as such.
It has not been submitted, either in part or whole, for a degree at this or any other university.

_____ _____

Remerciements

Ces mots sont les derniers que j'écris mais je sais qu'ils seront parmi les premiers lus, alors je souhaiterais faire passer le message le plus important à mes yeux ici : *la recherche scientifique est une aventure collective.* Ce manuscrit n'est signé que par une seule personne mais cela ne pourrait pas être moins représentatif de la manière dont ma thèse s'est déroulée, et je souhaiterais remercier toutes les personnes qui y ont contribué de près ou de loin.

Ce travail n'aurait pas pu voir le jour sans mes deux directeurs de thèse, **Peter Holdsworth** et **Elsa Lhotel**. Votre enthousiasme, votre gentillesse à toute épreuve et votre vision d'ensemble m'ont été d'une aide inestimable. Je vous suis extrêmement reconnaissant d'avoir été autant disponibles à tout instant pour répondre à toutes mes questions. Vous avez su me motiver dans les moments plus difficiles, et surtout mettre mes idées en perspective quand je m'emballais un peu trop ! Merci de m'avoir fait confiance pendant ces presque 4 années et de m'avoir appris autant.

Je voudrais également remercier les éminents chercheurs qui ont accepté d'évaluer mon travail et de faire partie de mon jury: **Patrik Henelius**, **Françoise Damay**, **Michel Kenzelmann**, **Radu Coldea** et **Arnaud Ralko**. La séance de questions que vous avez menée pendant ma soutenance, ainsi que les discussions que j'ai eues avec vous après, ont été autant agréables qu'instructives sur mon travail et la suite de ma carrière.

Au cours de ma thèse, j'ai eu le plaisir de discuter avec des chercheurs et chercheuses passionnantes, qui m'ont énormément aidé directement ou non. Je vais faire de mon mieux pour tous vous remercier ci-dessous.

Virginie Simonet, pour m'avoir appris les rudiments de la diffusion de neutrons, et m'avoir aidé à gérer les caprices de FullProf. **Julien Robert**, pour nos discussions sur la théorie des représentations, pour avoir accepté de simuler autant de combinaisons d'échanges que je pouvais imaginer, et pour avoir persévérer pour intégrer ce satané terme quartique. **Sylvain Petit**, pour nos expériences de diffraction de neutrons sous pression si frustrantes mais si intéressantes. **Daniel Braithwaite**, pour nos mesures de chaleur spécifique sous pression et pour avoir accepté de m'apprendre à préparer une cellule diamant. **Thierry Klein** pour avoir accepté de réaliser ces mesures AC de chaleur spécifique sur un nouveau composé et m'avoir formé à utiliser ta très belle expérience. **Élise Pachoud** et **Abdellali Hadj-Azzem** pour la difficile synthèse de ruthénate d'holmium, et pour nos discussions sur la diffraction de rayons X après que ce composé a décidé de vieillir. Je voudrais remercie également **Thomas Hansen**, **Claire Colin**, **Pascal Manuel** et **Ross Stewart** pour avoir tenté autant que possible de réaliser nos rêves les plus fous à l'occasion des différences expériences de neutrons à l'ILL et à ISIS. Merci également à **Sophie De Brion**, **Carley Paulsen**, **Rafik Ballou**, **Marie-Aude Méasson**, **Lucile Savary** pour toutes nos discussions scientifiques ou non. Merci également à **Élodie Ferrara**, **Mathilde**

Bérard, **Stéphanie Thépot** et **Caroline Bartoli** pour vous être pliées en quatre quand je rencontrais un problème administratif ou financier.

Évidemment la thèse serait beaucoup moins agréable si on ne pouvait pas partager son expérience avec d'autres doctorants et post-doctorants, à la fantastique salle café du bâtiment E, au traditionnel *pub* du vendredi soir ou dans la montagne l'hiver ou l'été. Un grand merci donc à **Owen**, **Edward**, **Félix**, **Grégory**, **Nathan**, **Corentin**, **Jasmine**, **Ilya**, **Mads**, **Kylia**, **Richard**, **Antoine**, **Léo**, **Mathilde**, **Clément**... et à tous les autres que j'ai rencontré en conférence à Santa Barbara, Paris, Amsterdam ou Lyon, ou au séminaire des non-permanents.

Enfin, merci du fond du cœur à ma famille et à mes parents en particulier pour leur soutien sans faille, et pour m'avoir toujours fourni des conseils avisés.

Contents

Introduction

Frustrated magnets are a fascinating class of both theoretical models and materials. They have been a fruitful playground to test the limits of standard paradigms in statistical physics, as well as identify exotic magnetic transitions. Some of the most striking examples are the Holmium and Dysprosium titanate pyrochlores, which were proven to be realizations of so-called spin ices. In these materials, Ising-like spins occupy sites of a pyrochlore lattice, a corner sharing array of tetrahedra. The spins point into and out of the centres of the tetrahedra which frustrates the ferromagnetic interaction. In the lowest energy configuration the spins satisfy a two spins in and two spins out ice-rule, which gives rise to a disordered but correlated phase called spin ice. In Dysprosium and Holmium iridate pyrochlores, the Iridium atoms order antiferromagnetically at about 130 K and provide a staggered local field to the rare-earth spins. The competition with the ferromagnetic exchange shifts the ground state towards a phase where the local rule is three spins in and one spin out. The physics of Ising pyrochlores can then be brought together in the framework of magnetic fragmentation, which will be the central concept of this work. It makes it possible to understand how the same material can host a coexistence of an ordered and disordered phase, each contributing to one half of the magnetic moment. This thesis work focuses on expand the knowledge of the fragmentation phase diagram, with an emphasis on a close collaboration between theory and experiment.

In the first chapter we present the general physics of Ising pyrochlores, highlighting the phenomenon of fragmentation. We first explain the important concepts using a simple nearest-neighbor model, then introduce the relevant pyrochlore materials and their properties. Finally we give an overview of the other magnetic phases which can exist on the pyrochlore lattice, and present a simple formalism to study the effects of quantum fluctuations. The second chapter we introduce the various experimental techniques we have used in the study of frustrated pyrochlore magnets. The next three chapters are dedicated to the results of this thesis work.

In Chapter 3 we study the persistence of the fragmented phase at low temperatures where quantum fluctuations could become relevant. Using a mapping to a dimer model rendered straightforward by the fragmentation formalism, we first investigate the case of a simpler two-dimensional example of fragmentation and identify two possible phases and a measurable order parameter to tell them apart. Using the same method, we conclude that fragmentation would be destroyed in the three-dimensional case because quantum fluctuations would drive the system to fully order.

In Chapter 4, we study the Holmium ruthenate pyrochlore in which Ho magnetic moments exhibit a transition at 1.5 K. We perform low temperature magnetic, specific heat and neutron diffraction measurements and find that the Holmium ions have a partial ordered moment, a small residual entropy and peculiar diffuse scattering patterns. We interpret these results within

the framework of fragmentation as a new fragmented structure, where the ordered fragment is this time of ferromagnetic nature.

In Chapter 5, we perform challenging neutron diffraction and AC specific heat measurements under pressure on pyrochlore iridates, in order to probe the phase diagram and identify predicted transitions. While the experimental results proved difficult to analyse, we provide a more complete mean-field description of the phase diagram to help interpret the observations.

Chapter 1

Spin ices: models, materials and fragmentation

Contents

1.1 Introduction to nearest-neighbor pyrochlore spin ice

The starting point of this thesis is the concept of *magnetic frustration*. It is defined as a situation where all pairwise interactions between neighboring spins cannot be satisfied at the same time. A a simple example, consider a set of Ising spins σ_i with nearest-neighbor coupling J:

$$\mathscr{H} = -J \sum_{\langle i,j \rangle} \sigma_i^z \sigma_j^z \tag{1.1.1}$$

which are then placed on a triangular pattern as pictured in Figure 1.1.1 (left). If the coupling is ferromagnetic $J > 0$ the ground state is straightforward with all spins pointing in the same direction. If it is antiferromagnetic however, there ends up being two distinct states with the same lowest energy. In this instance the frustration has a geometric origin, namely the fact that the triangle is not bipartite. It also highlights that frustration can create a degeneracy. However, it is also possible to create frustration on a bipartite lattice by adding next-nearest-neighbor couplings, for example with the $J_1 - J_2$ model on the square as pictured in Figure 1.1.1 (right). Lets assume that the standard first-neighbor exchange is ferromagnetic; then an antiferromagnetic second-neighbor exchange on the diagonal can compete in a way that makes it impossible to satisfy all links, and find a single ground state. Of course these examples are heavily simplified, and in more realistic situations frustration can usually be relieved by considering spins of a more complex nature. For example, the classical XY antiferromagnet on the triangular lattice orders in a peculiar 120° state with an enlarged unit cell. Therefore, the existence of frustration depends both on the lattice geometry, the nature of the spins and the specifics of the interactions.

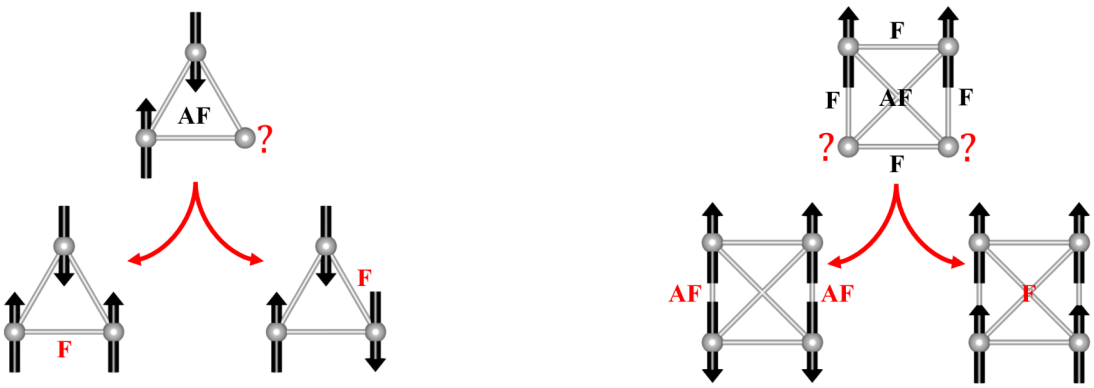

Figure 1.1.1: Simple examples of frustration. (Left) Antiferromagnetic Hamiltonian on a triangle. (Right) $J_1 - J_2$ model on a square, with opposite exchanges.

Pyrochlore Spin ices are a subset of frustrated systems that have attracted considerable attention due to their puzzling experimental and theoretical signatures [Harris et al., 1997; Ramirez et al., 1999]. In this first section we will present the most important properties of spin ices and the concept of fragmentation using only a simple nearest-neighbor Ising model, which will be

our reference point all along the thesis. In a second part we will introduce the relevant materials and a more refined long-range model to describe their behavior. Finally we will present the magnetic phases allowed of the pyrochlore lattice beyond the Ising case, and introduce the formalisms to study quantum fluctuations.

1.1.1 Frustration on the pyrochlore lattice

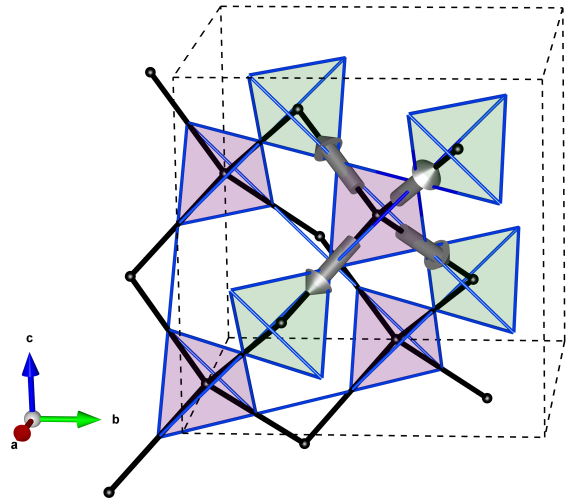

Figure 1.1.2: Pyrochlore lattice (blue) and its dual diamond diamond lattice (black). Tetrahedra of type A (B) are shown in shaded purple (green) respectively. The cubic unit cell is delimited by the dashed lines and contains sixteen sites. The grey arrows show the four $\vec{d}$ vectors defined in the text.

A pyrochlore lattice is built from corner-sharing tetrahedra, forming a four-sublattice face centred cubic structure. A convention in discussing this system is to use the overlying cube of side a_c containing sixteen sites, as shown in Fig. (1.1.2). A laboratory frame $[\hat{a},\hat{b},\hat{c}]$ is then defined with respect to the basis vectors of the cube. On this lattice we define local axes pointing in the four $\langle 111\rangle$ directions. They are

$$\begin{aligned} \mathbf{z}_1 &= \frac{1}{\sqrt{3}}[1,1,1], & \mathbf{z}_2 &= \frac{1}{\sqrt{3}}[1,-1,-1] \\ \mathbf{z}_3 &= \frac{1}{\sqrt{3}}[-1,-1,1], & \mathbf{z}_4 &= \frac{1}{\sqrt{3}}[-1,1,-1]. \end{aligned} \tag{1.1.2}$$

and are also called the local z axes. The centers of each tetrahedron form a diamond lattice. The pyrochlore and diamond lattice sites are labeled i,j and I,J respectively. As the diamond lattice is bipartite, we can separate it in A and B sublattices which we represent with purple and green tetrahedra respectively. From a modelling point of view this defines an index η_I equal to $+1,-1$ for the A,B sublattice respectively.

We now place Ising variables $\sigma_i = \pm 1$ on the vertices on the pyrochlore lattice, pointing along

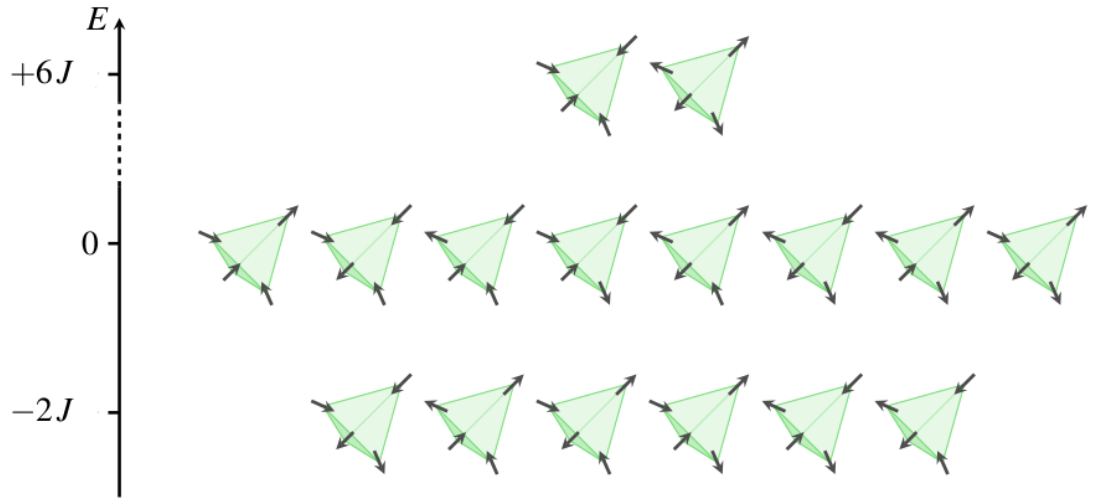

Figure 1.1.3: Energy of the different configurations of a tetrahedron in the nearest-neighbor spin ice model. From bottom to top: ice rule (no defect), single defects, double defects.

the local axes **d**, such that +1 spins all point out of an A type tetrahedron. Consider the following nearest-neighbor Hamiltonian:

$$\mathscr{H}_{\mathrm{NN}} = -3J \sum_{\langle i,j \rangle} (\sigma_i \mathbf{z}_i) \cdot (\sigma_j \mathbf{z}_j) = J \sum_{\langle i,j \rangle} \sigma_i \sigma_j \tag{1.1.3}$$

It can be rewritten as the sum over tetrahedra:

$$\mathscr{H}_{\mathrm{NN}} = \frac{J}{2} \sum_I Q_I^2 + \mathrm{cte} \text{ with } Q_I = \eta_I \sum_{i \in \text{ tet } I} \sigma_i \tag{1.1.4}$$

We consider the case where the coupling is ferromagnetic $J > 0$. The ground state is therefore found by minimizing the value of $|Q|$ on every tetrahedron, namely imposing $Q = 0$ everywhere. This is called the *ice rule*: two spins point in and two spins point out [Harris et al., 1997]; the case where $Q \neq 0$ will be investigated below. As a consequence, among the $2^4 = 16$ states of a single tetrahedron, one finds that $\binom{4}{2} = 6$ have the same lowest energy: the frustration has created a degeneracy. The other possible energies and their multiplicities for a single tetrahedron are summarized in Figure 1.1.3.

The local constraint was first highlighted in the case of cubic water ice, where the "ice rule" refers to the local constraint for the ground state: 2 protons close / 2 protons far from and Oxygen; hence the name "spin ice" for our system. What is the consequence of this degeneracy on the scale of the entire lattice ? Let us compute an approximation of the number of states satisfying the ice rule for a lattice of N tetrahedra, meaning $2N$ spins [Ryzhkin, 2005]. We assume that tetrahedra can be considered independent of one another, meaning that each of the 6 distinct 2 in / 2 out configurations $\{N_1, \ldots, N_6\}$ are occupied with the same probability: $N_1 = \cdots = N_6 = N/6$. However they still have to be compatible, in the sense that a spin pointing

out of a tetrahedron has to be pointing into its neighbor; so each of the $2N$ spins only has a $1/2$ probability of being accepted in the lattice tiling. The number of states W is then

$$W = \left(\frac{1}{2}\right)^{2N} \frac{N!}{N_1!\dots N_6!} = \left(\frac{1}{4}\right)^{N} \frac{N!}{\left(\frac{N}{6}\right)!^6} \tag{1.1.5}$$

and the entropy per tetrahedron is, using Stirling's formula:

$$\frac{S}{N} = k_B \ln\left(\frac{3}{2}\right) \approx 0.405\, k_B \tag{1.1.6}$$

This approximation is called Pauling entropy and is very close to the more rigorous calculation involving an analytical series [Nagle, 2004]. As temperature goes to 0, the systems retains an entropy associated to the extensive number of 2 in / 2 out configurations. From an experimental standpoint this zero-point entropy was first measured by Ramirez et. al. [Ramirez et al., 1999], by performing specific heat measurements.

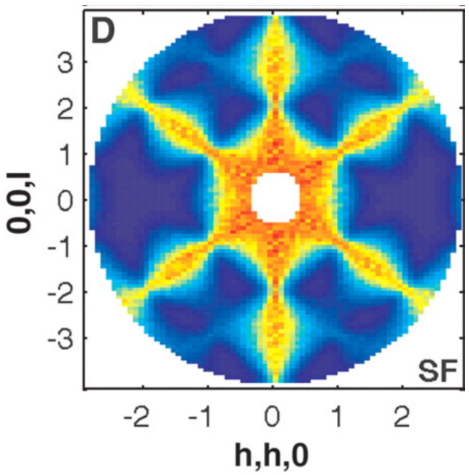

Figure 1.1.4: Pinch-points neutron scattering pattern simulated in the nearest-neighbor spin ice model. Figure reproduced from [Fennell et al., 2009]

Another way of understanding what happens in spin ice at low temperature is to note that the system doesn't order, but stays correlated through the ice rule. To derive the general shape of the correlations we define a lattice field between two adjacent diamond lattice sites I, J from the Ising variable σ_j between them [Lhotel et al., 2020]:

$$M_{IJ} = \eta_I \sigma_j, \text{ such that } M_{JI} = -M_{IJ} \tag{1.1.7}$$

which we coarse-grain over a mesoscopic volume to obtain a continuous vector field $\mathbf{M}(\mathbf{r})$. Using this field the ice rule takes the form of a zero divergence constraint:

$$\nabla \cdot \mathbf{M}(\mathbf{r}) = 0, \text{ or in reciprocal space } \mathbf{k} \cdot \mathbf{M}(\mathbf{k}) = 0 \tag{1.1.8}$$

Therefore **M** behaves as the curl of an emergent gauge field

$$\mathbf{M} = \nabla \times \mathbf{A} \tag{1.1.9}$$

The various phases of condensed matter which can be mapped onto such a field are called *Coulomb Phases*, for the following reason. The fluctuations of **M** at a certain wave vector **k** are strongly constrained by the fact that they have to be transverse, that is to say perpendicular to **k**. In a long wavelength limit the correlations functions take the following forms in reciprocal and real space respectively [Henley, 2010]:

$$\begin{aligned} \langle M_\mu(-\mathbf{k}) M_\nu(\mathbf{k}')\rangle &\propto \delta_{\mathbf{k}\mathbf{k}'}\left(\delta_{\mu\nu} - \frac{k_\mu k_\nu}{k^2}\right) \\ \langle M_\mu(0) M_\nu(\mathbf{r})\rangle &\propto \delta_{\mathbf{r}} + \frac{1}{r^3}\left(\delta_{\mu\nu} - \frac{r_\mu r_\nu}{r^2}\right) \end{aligned} \tag{1.1.10}$$

The first expression implies that in reciprocal space the correlations are singular in one direction and continuous on a perpendicular one. These specific patterns resemble bow ties, as pictured in Figure 1.1.4 and are called pinch points. This type of diffuse elastic scattering is another type of important signature of the spin ice phase. The second expression shows that the correlations have the spatial dependence of dipole-dipole interactions. In particular, they decrease as $1/r^d$ with d the dimension of the system.

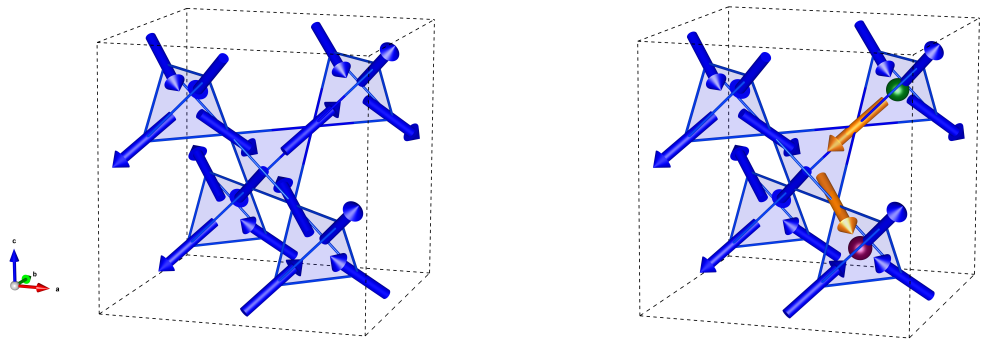

Figure 1.1.5: (left) Pyrochlore spin ice (right) A breaking of the local ice rules leads to two deconfined excitations dubbed magnetic monopoles. The two sublattices A and B are shaded in blue and yellow.

What happens now if we break the ice rule? A spin flip on the pyrochlore lattice breaks the ice rule on two adjacent tetrahedra: one ends up with three spins in and one out, and the other with three out and one in. These tetrahedra actually host excitations which can propagate through the diamond lattice by subsequent spin flips: the ice rule is restored on one tetrahedron but broken on the next one. The two opposite charges are then linked by a string of flipped spins, shown in yellow in Figure 1.1.5 (right). The quantity Q defined in Equation (1.1.4) acquires the nature of a topological charge, indexing the type of excitation. Indeed definition of the M_{IJ} field

relates it to the charge with a lattice Gauss law:

$$\sum_{J=1}^{4} M_{IJ} = Q_I \tag{1.1.11}$$

These observations led to such excitations of pyrochlore spin ice being dubbed *monopoles*, simple when $Q = \pm 1$ and double when $Q = \pm 2$. Using this language we can also describe the nearest-neighbor model in Equation (1.1.4) when $J < 0$. The model is then unfrustrated, because it has only 2 ground states which are defined by maximizing the value of Q everywhere. It corresponds to an antiferromagnetic structure where every tetrahedron has all its spins either in or out, which creates an alternating pattern of $+2$ and -2 charges. Hence this state is called all in / all out (AIAO) or a crystal of double monopoles.

1.1.2 Fragmentation

The concept of magnetic fragmentation relies on the application of the Helmholtz decomposition to the magnetization of a Ising pyrochlore magnet [Brooks-Bartlett et al., 2014]. Under suitable boundary conditions, any vector $3D$ field $\mathbf{M}$ can be decomposed into two terms:

$$\mathbf{M} = \mathbf{M_m} + \mathbf{M_d} = \nabla\Psi + \nabla \times \mathbf{A} \tag{1.1.12}$$

$\nabla\Psi$ is a divergence-full term, also called the *longitudinal field*, and $\mathbf{A}$ is the emergent field divergence-free field defined above, also called the *transverse field*. This decomposition might seem innocuous, and in the case of a generic distribution of monopoles it is not straightforward to perform. Through the lattice Gauss law described above, Ψ can be related to the monopole density via a Poisson equation. Creating a pair of monopoles by flipping a spin transfers some weight from the transverse to the longitudinal field but not all, as we will explain below.

Let us consider a "ionic" crystal of monopoles in a pyrochlore lattice, meaning ± 1 monopoles on sublattices A/B respectively (Figure 1.1.6 top). Such a phase can be stabilized in the nearest-neighbor model by adding a local field Δ along the $\mathbf{d}$ directions, which translates to a staggered chemical potential for the monopoles:

$$\begin{aligned} \mathcal{H}_{\text{Frag}} &= J \sum_{\langle i,j \rangle} \sigma_i \sigma_j - \Delta \sum_i \sigma_i \\ &= \frac{J}{2} \sum_I Q_I^2 - \Delta \sum_I \eta_I Q_I \end{aligned} \tag{1.1.13}$$

which favors $+/-$ monopoles on sublattice A/B respectively. The ground state of this Hamiltonian is a simple monopole crystal, where every tetrahedron is either three out / one in or three in / one out. Such a state is extremely enlightening to study within the framework of fragmentation because the decomposition can be done on the scale of a single tetrahedron, which we represent by the vector of Ising variables $[\sigma_i]$. Taking into example a 3 in / 1 out state, we can write:

$$\mathbf{M} = [-1,-1,-1,1] = [-\frac{1}{2},-\frac{1}{2},-\frac{1}{2},-\frac{1}{2}]_{\mathbf{m}} + [-\frac{1}{2},-\frac{1}{2},-\frac{1}{2},+\frac{3}{2}]_{\mathbf{d}} \tag{1.1.14}$$

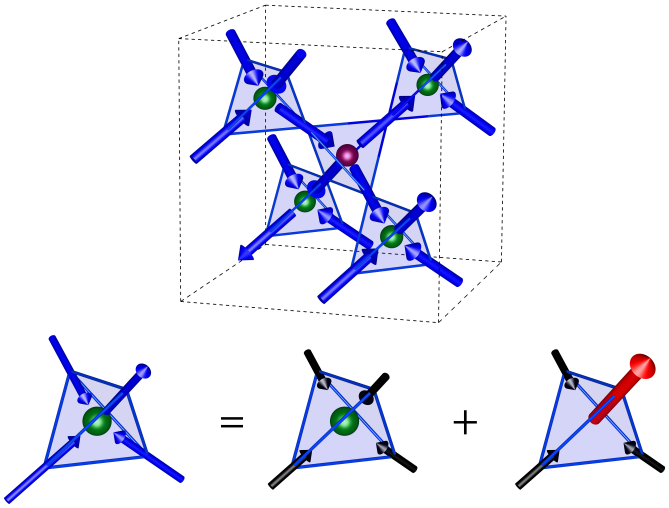

Figure 1.1.6: (top) Monopole crystal on the pyrochlore lattice. (bottom) Decomposition in longitudinal/divergence-full and transverse/divergence-free components on a single tetrahedron. The 3/2 field element of the transverse part is pictured in bright red

where the first component is divergence-full (containing all the monopole charge) and second is divergence-free (it contains no monopole charge). This is pictured graphically on figure 1.1.6 (bottom). Because of this decomposition, we will call the monopole crystal phase the fragmented phase. The longitudinal fragment is ordered all in / all out but with elements of field of length 1/2. In other words, this state exhibits antiferromagnetic ordering but with only half of the magnetic moment. The rest of the moment is in the transverse emergent field. This example is peculiar in that it has element of field of different lengths ($-1/2$ and $+3/2$) to ensure it is divergence-free. More specifically, it has exactly one element $+3/2$ per tetrahedron, meaning that it can be mapped to a dimer model on the diamond lattice. Links with $+3/2$ bear a dimer and links with $-1/2$ are empty, so that there is exactly one dimer touching each vertex. This mapping is represented on figure 1.1.6 with $+3/2$ field elements / dimers in bright red. Since there are actually two ways to define the emergent field (as in being along or being opposite to the $+3/2$ field element), it is formally said that the transverse field maps onto one $\mathbb{Z}_2$ sector of the dimer model [Huse et al., 2003]. On the diamond lattice, the dimer model also has a residual entropy, which cannot be computed with a Pauling-like argument but needs more involved combinatorial techniques [Nagle, 1966]. It is slightly reduced compared to spin ice: $S_{\text{Frag}} \approx k_B \ln(1.3)$ per tetrahedron [Brooks-Bartlett et al., 2014; Raban et al., 2019].

We can now update the experimental signatures of spin ice phases to include the monopole crystal. In this example, the signatures of magnetic fragmentation lie in the fact that the longitudinal fragment is ordered, while the transverse fragment remains disordered. Similarly to the spin ice phase, the emergent field has dipolar correlations because of its divergence-free constraint. Therefore, the monopole crystal exhibits a coexistence of order and disorder. This can be seen first and foremost in neutron scattering, where a pinch point diffuse scattering coexist with magnetic Bragg peaks. Specific heat can be used to measure the non-zero residual entropy

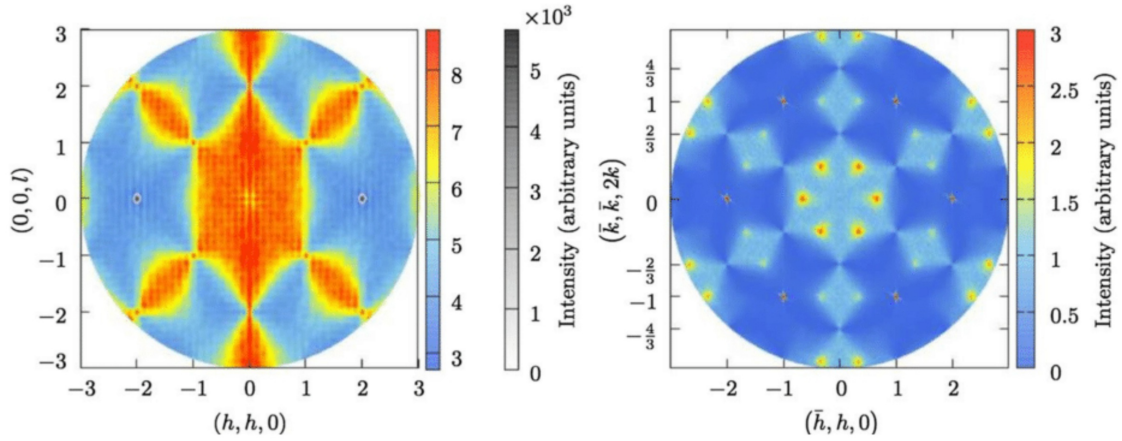

Figure 1.1.7: Simulated neutron scattering intensity for pyrochlore monopole crystal (left) and kagome ice (right). The intensity of the magnetic Bragg peaks for the pyrochlore is plotted in gray scale. Figure reproduced from [Brooks-Bartlett et al., 2014]

[Cathelin et al., 2020].

1.1.3 Spin ice under field and kagome ice

The last preliminary physics we will explore within the nearest-neighbor model is the behavior of spin ice under field. There are three main behaviors depending on the direction in which the field is applied, shown in Figure 1.1.8

- Field along [100]: the state reached at saturation has all A-type tetrahedra in the same two in / two out state, such that they all have their magnetization aligned with the field. The magnetization per spin at saturation is $M_{\text{sat}}/\sqrt{3}$;
- Field along [110]: at saturation, all tetrahedra have two spins pinned along the field, pictured in green. The two remaining spin are perpendicular to the field and therefore do not contribute to the Zeeman energy, but must still satisfy the ice rule. They form chains of spins along $[1\bar{1}0]$ which can take either of two orientations. The magnetization per spin at saturation is $M_{\text{sat}}/\sqrt{6}$;
- Field along [111]: at low temperature, the magnetization as a function of field first exhibits a plateau before reaching saturation. On this plateau, one spin per tetrahedron is pinned along the field and is called the apical spin. The three other spins are left to satisfy the ice rules. The magnetization per spin on this plateau $M_{\text{sat}}/3$. As the field increases, the Zeeman energy ends up dominating over the exchange so all spins align with the projection of the field along their local axes. This breaks the ice rules and as an example the state at saturation has every A-type tetrahedron in a three in / one out state. The magnetization per spin at saturation is $M_{\text{sat}}/2$.

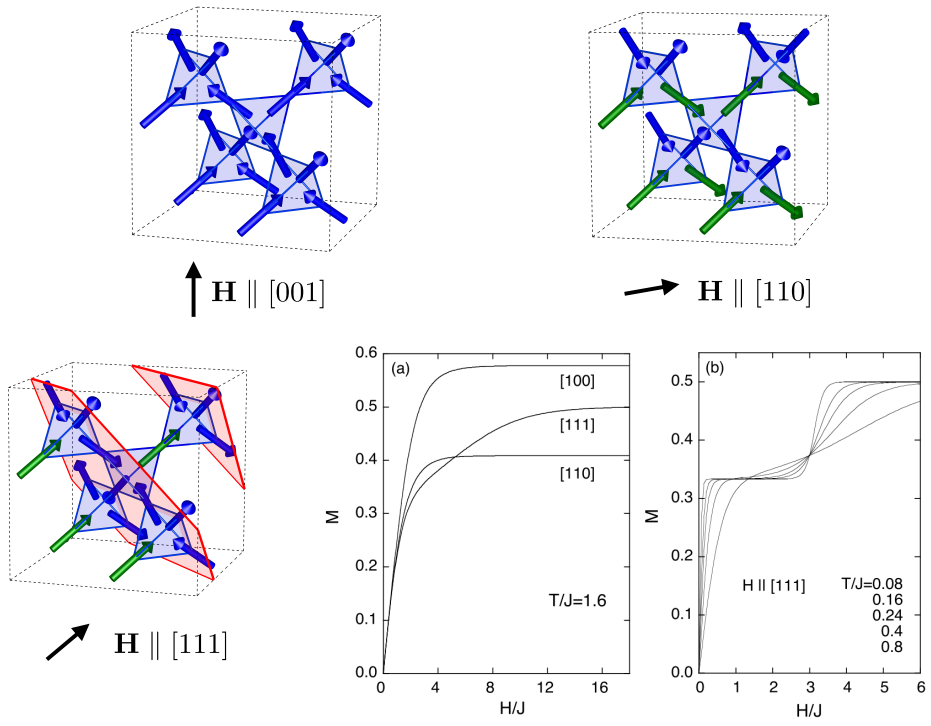

Figure 1.1.8: Pyrochlore spin ice under a field in different directions. (Top left) Field along [001] (Top right) Field along [110]. Two spins per tetrahedron are pinned along the field, pictured in green. (Bottom left) Field along [111], of moderate strength so that the system is on the kagome plateau. Apical spins, pinned along the field, are shown in green. Kagome planes are shown in red. (Bottom right) Calculated magnetization per spin for an isolated tetrahedron under field. The left graph shows the magnetization for the three field directions at a fixed temperature, the right one shows the plateau that occurs for small field along [111] at low temperature. Graphs reproduced from [Udagawa et al., 2021]

Let us focus on the magnetization plateau under a moderate [111] field. The pyrochlore lattice can be decomposed perpendicularly to the [111] direction into a series of triangular planes formed by the apical spins (the ones whose local axes are parallel to the field), and a series of kagome planes on which the three other spins reside. The kagome lattice is formed of corner sharing triangles and like the pyrochlore lattice, it can be separated into A/B-type triangles. As an example, suppose the apical spin is pinned in on a A-type tetrahedron. It turns out that there is a degenerate number of states which satisfy the pyrochlore ice rules with one spin per tetrahedron fixed. The kagome spins of an A-type tetrahedron must be in a one in / two out configuration. On the neighboring B-type tetrahedron where the apical spin is out, they will be two in / one out. Therefore the magnetization plateau is characterized by a different set of ice rules, which apply only to the kagome spins and are hence called the *kagome ice rules*. More specifically, because of the regular alternance between A and B sites this phase is called the KII

kagome spin ice [Moessner et al., 2003a]. It is pictured in Figure 1.1.9.

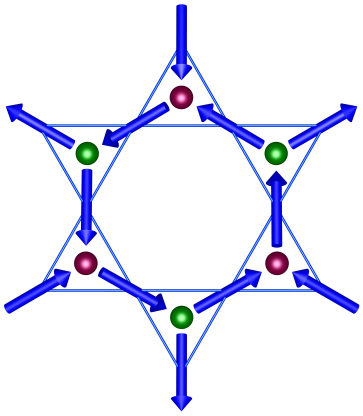

Figure 1.1.9: KII kagome spin ice. It is charge-ordered but spin disordered.

Similarly to the pyrochlore case, we now apply the fragmentation formalism to one A-type triangle:

$$\mathbf{M} = [-1,-1,1] = [-\frac{1}{3},-\frac{1}{3},-\frac{1}{3}]_{\mathbf{m}} + [-\frac{2}{3},-\frac{2}{3},+\frac{4}{3}]_{\mathbf{d}} \tag{1.1.15}$$

Similarly to the pyrochlore case, the first term is an all in / all out field which is divergence-full. It corresponds to a charge crystal on the hexagonal lattice. However the excitations indexed by this charge are not deconfined and are therefore not called monopoles. On the other hand, the transverse emergent field has exactly one element of length $+4/3$ per triangle, the rest being of length $-2/3$ to ensure it has zero divergence. This makes it possible to map this field onto another dimer model, where a dimer is placed on the sites with $+4/3$ field value. The dimers end up connecting the center of two adjacent triangles on the kagome lattice, which form a hexagonal lattice. This dimer model also has a degenerate ground state, meaning that kagome ice remains spin-disordered despite being charge-ordered and has an extensive residual entropy. In the case of pyrochlore spin ice under a moderate [111] field the residual entropy per tetrahedron is $S \approx k_B \ln(1.17)$, which can again be measured by specific heat measurements under field. As far as neutron scattering signatures are concerned, the AIAO longitudinal field is associated to antiferromagnetic Bragg peaks whereas the divergence free constraint on the emergent field translates into pinch-point patterns. This coexistence of order and disorder is shown in Figure 1.1.7 (right). KII kagome ice therefore spontaneously exhibits fragmentation, without needing any staggered chemical potential, namely because of the odd number of spins per triangle.

1.2 Materials and models

1.2.1 Rare-earth pyrochlore oxides

The materials we will study in this thesis are part of the family of rare-earth pyrochlore oxides $R_2M_2O_7$. In this crystal structure the rare-earth R and metal M each occupy a distinct pyrochlore

lattice which interpenetrate, shown in Figure 1.2.1. The lattice constant a is of the order of 10 Å. The Oxygens create a local octahedral environment on the two other species. One Oxygen position is free and noted by a parameter x, in the range $0.32 - 0.34$. The space group of the entire structure is $Fd\bar{3}m$.

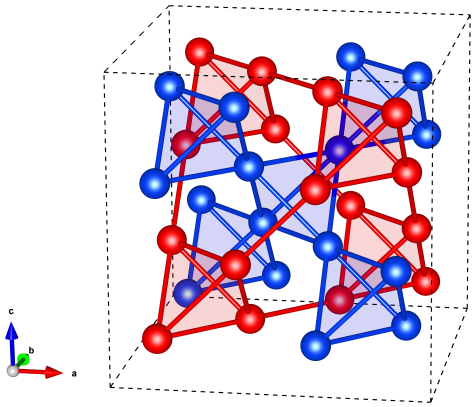

Figure 1.2.1: Interpenetrating pyrochlore lattices of the rare-earth (in blue) and the metal (in red).

The valence of the rare-earth is 3+, leaving an unfilled $4f$ shell. The interactions from the environment are screened by the $5s$, $5p$ and $6s$ shells so the dominant interaction on the $4f$ electron is the spin-orbit, followed by the crystal field created by the Oxygen environment. Therefore it is natural to consider a perturbative picture where the crystal field acts on the multiplets $|J,M\rangle$.

Rare earth are defined by an unfilled $4f$ level whose electrons are very localized and have a large angular momentum. Therefore the interactions they experience first is the spin-orbit coupling, then the crystal field from the tetragonal environment of Oxygen atoms as a perturbation. In the case of Holmium and Dysprosium, which will be our rare-earth of interest, the ground state is formed from almost only the $|+J\rangle, |-J\rangle$ doublet, with a moment pointing along the local z axes, separated from the first excited states by an energy of about 200 to 300 K [Jaubert et al., 2011]. It ensures at temperatures below 10 K, the doublet behaves like a classical, dipolar Ising spin.

The magnetic moment operator is:

$$\hat{\mu} = g_J \frac{-e}{2m_e}\hat{\mathbf{J}} = -g_J \frac{\mu_B}{\hbar}\hat{\mathbf{J}} \tag{1.2.1}$$

with the standard g-factor formula

$$g_J = 1 + \frac{J(J+1) + S(S+1) - L(L+1)}{2J(J+1)} \tag{1.2.2}$$

In the case of a simple $|+J\rangle, |-J\rangle$ doublet, the value of the magnetic moment projected along

the local z axes is

$$\mu_{/\!/} = g_J \mu_B J \tag{1.2.3}$$

It can be related to the magnetic moment measured at saturation, and will be slightly different to the effective paramagnetic moment $\mu_{\text{eff}} = g_J \mu_B \sqrt{J(J+1)}$. In the rest of this text we will use the projected magnetic moment $\mu_{/\!/}$ for the definition of interactions and the measurements. The properties of the Ho^{3+} and Dy^{3+} ions are summed up in Table 1.2.1. Their main difference is that Dy^{3+} is a Kramers ion (with an odd number of electrons), while Ho^{3+} is non-Kramers (even number of electrons). It means that time-independent perturbations like defects in the lattice can split the Holmium ground state doublet, while the Dysprosium will be more robust.

Ion	Configuration	S	L	J	$\mu_{/\!/}$
Dy^{3+}	$[Xe]4f^9$	5/2	5	15/2	$\approx 10\ \mu_B$
Ho^{3+}	$[Xe]4f^{10}$	2	6	8	$\approx 10\ \mu_B$

Table 1.2.1: Single-ion parameters for Dy^{3+} and Ho^{3+}. Their actual magnetic moments will be slightly lower than 10 μ_B due to the actual components of the wavefunction. Table adapted from [Jaubert et al., 2011]

1.2.2 Dipolar Spin Ice

In Ising pyrochlores like $Dy_2Ti_2O_7$ or $Ho_2Ti_2O_7$, the dipolar interaction cannot be neglected due to the large dipole moment of the effective spin. Furthermore, the exchange interaction is usually antiferromagnetic, which seems to contradict the minimal model considered before. The full Hamiltonian of the system, called dipolar spin ice (DSI), reads [Melko et al., 2001]:

$$\mathcal{H}_{\text{DSI}} = -J \sum_{\langle i,j \rangle} \mathbf{S}_i \cdot \mathbf{S}_j + D \frac{r_{nn}^3}{2} \sum_{i \neq j} \frac{(\mathbf{S}_i \cdot \mathbf{S}_j) \cdot (\mathbf{r}_{ij} \cdot \mathbf{r}_{ij}) - 3(\mathbf{S}_i \cdot \mathbf{r}_{ij})(\mathbf{S}_j \cdot \mathbf{r}_{ij})}{| \mathbf{r}_{ij}^5 |} \tag{1.2.4}$$

where J is the direct exchange constant and D is the dipolar constant. It is defined from the amplitude of the dipoles μ and the pyrochlore nearest-neighbor distance r_{nn} by

$$D = \frac{\mu_0 \mu^2}{4\pi r_{nn}^3} \tag{1.2.5}$$

It is natural to ask how the spin-ice physics can arise from a Hamiltonian of this complexity. The first piece of the answer lies in the truncation of the dipolar term to its nearest-neighbor part. From the discussion of the crystal field theory above we know that the spins can be very accurately represented by Ising dipoles. The result is the following nearest-neighbor Hamiltonian, where the spins $\mathbf{S}$ are replaced with Ising variables σ along the local $< 111 >$ axes:

$$\mathcal{H}_{\text{NN}} = \frac{J + 5D}{3} \sum_{\langle i,j \rangle} \sigma_i \sigma_j \tag{1.2.6}$$

On the table we summarize the approximate numerical values of the DSI model for both dysprosium and holmium titanates, with $J_{\text{eff}} = \frac{J+5D}{3}$. The numerical factors are due to the geometrical projection to the local axes. In some texts the projected values of the exchange and dipolar constants are referred to as $J_{nn} = J/3$ and $D_{nn} = 5D/3$. For both material J_{eff} ends up

	J	D	J_{eff} (K)
$Dy_2Ti_2O_7$	−3.7	1.4	1.1
$Ho_2Ti_2O_7$	−1.6	1.4	1.8

Table 1.2.2: Approximated values of the DSI model obtained for $Dy_2Ti_2O_7$ and $Ho_2Ti_2O_7$, from [Gardner et al., 2010; Bramwell et al., 2001; Gingras et al., 2000]

being positive, so we recover an effective spin ice Hamiltonian. This highlights the paramount importance of dipolar interactions in the stabilization of a spin ice Coulomb phase. However this does not answer the question of the validity of discarding the long-range interactions beyond nearest-neighbor. In [Melko et al., 2001] the authors investigated the precise effect of the dipolar interactions on the spin ice manifold. They computed the eigenvalues of the dipolar interactions for various ordering wave-vectors and found that it is remarkably flat thanks to the geometry of the pyrochlore lattice. This explains why the dipolar interactions only affect the spin ice ground state at very low temperatures, driving a transition to an (001) ordered structure called Melko-den Hertog-Gingras order below $T/D \approx 0.07$ or $T \approx 100$ mK. However this order has not definitely been observed in real materials. Indeed, in spin ice materials the characteristic spin relaxation times becomes macroscopically long below about 700 mK because of the sometimes very high energy cost of some spin move needed to get rid of all monopole defects. This makes such materials challenging to correctly thermalize below those temperatures, a fact that we will be particularly relevant in all experiments performed for this thesis.

The differences between the nearest-neighbor and dipolar spin ice models can be summarized on the phase diagram in Figure 1.2.2, adapted from [Guruciaga et al., 2014]. The nearest-neighbor model predicts an ordered AIAO phase for $J_{nn}/D_{nn} < -1$ (in blue), separated from a paramagnetic phase by a second order transition (dot-dashed lines). The spin ice regime is entered through a crossover (dotted lines) for $J_{nn}/D_{nn} < -1$. By contrast, the DSI model predicts a first-order transition (black lines) between the double monopole crystal (in grey) and spin ice phase. Surprisingly, it occurs at $J_{nn}/D_{nn} \approx -0.91$ so an effectively ferromagnetic J_{eff}, because the long-range Coulomb attraction between monopoles of opposite charge makes it energetically favorable to create and order them. Finally, we added to the original graph the first order transition in the spin ice phase to the Melko order which is seen in well-equilibrated simulations of the DSI model.

1.2.3 Dumbbell Model

Because the dipolar interactions only have an effect on the spin ice manifold at low temperatures, some authors have sought a way to include their effect in a more experimentally relevant way. In [Castelnovo et al., 2008], they successfully performed such approximation by introduc-

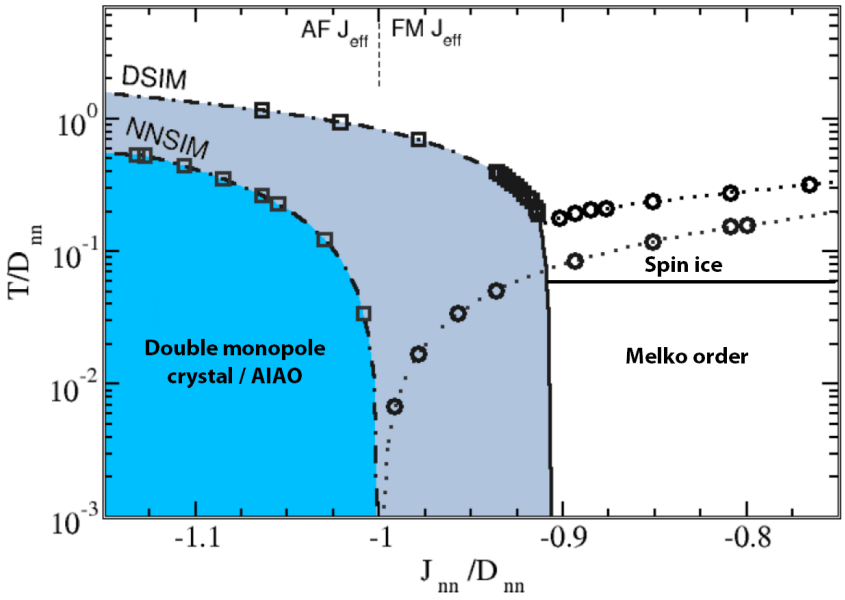

Figure 1.2.2: Comparative phase diagram of the nearest-neighbor and dipolar spin ice model, adapted from [Guruciaga et al., 2014].

ing the *Dumbbell model*. Their core idea, pictured in Figure 1.2.3, is to promote the point dipoles of the DSI model to dipoles spanning the distance between two diamond sites, which carry at each of their ends a magnetic charge of value $q = \pm\mu/a$. We recall that $a = \frac{2}{\sqrt{3}} r_{nn}$. Therefore, defects carry a total charge $Q = \pm 2q$ for the simple defects or $Q = \pm 4q$ for the double defects. Using this picture, they found that the interaction energy between defects decreased proportionally to the distance between them, akin to a Coulomb law; thus the monopoles acquire a magnetic charge in addition to the topological one they carry in the nearest-neighbor model and are from then dubbed *magnetic monopoles*. The authors proposed the following dumbbell Hamiltonian, acting only on the monopole degrees of freedom on a diamond lattice:

$$\mathscr{H}_{\text{Dumbbell}} = \frac{1}{2} v_0 \sum_r Q_I^2 + \frac{\mu_0}{4\pi} \frac{1}{2} \sum_{I \neq J} \frac{Q_I Q_J}{|\mathbf{r}_{IJ}|} \tag{1.2.7}$$

$$= -v \sum_I n_I^2 + \frac{\mu_0 Q^2}{8\pi} \sum_{I \neq J} \frac{n_I n_J}{|\mathbf{r}_{IJ}|} \tag{1.2.8}$$

where $n_I = 0, \pm 1, \pm 2$ is the monopole occupation of site I. This expression seems similar to the study of a lattice Coulomb gas in the grand canonical ensemble. The first term corresponds to the creation cost of monopoles, following the chemistry convention of a negative chemical potential v ($4v$) for the simple (double) monopoles respectively. The second term corresponds to the Coulombic interaction energy between the monopoles. The authors showed how the chemical potential can be expressed as a function of the DSI model parameters, taking into

account the geometry of the dumbbells:

$$\nu = -\frac{1}{2}\nu_0 Q^2 = -2\left[\frac{J+5D}{3} + \left(-1+\sqrt{\frac{2}{3}}\right)\frac{D}{3}\right] = -\frac{2J}{3} - \frac{8}{3}\left(1+\sqrt{\frac{2}{3}}\right)D \tag{1.2.9}$$

This Hamiltonian looks very similar to the one of the one of a Coulomb gas of particles in the grand canonical ensemble, but it is important to keep in mind that it is actually one of a fixed number of spins in the canonical ensemble. The spins degrees of freedom can be integrated out the partition function to leave only the monopole degrees of freedom [Nisoli, 2020; Nisoli, 2020], but that is exactly what results in the residual entropy characteristic of spin ice. For these reasons, the lattice gas of monopoles in the dumbbell picture is not a standard electrolyte and was instead called a magnetolyte [Kaiser et al., 2018]. In this article, the authors studied how the effective creation cost of monopoles changes with respect to temperature. As monopoles are created through thermal excitations, the effective chemical potential $\nu_{eff} = -\partial U/\partial n$ is modified by the shielding of the long distance interactions. The authors were able to use the self-consistent Debye-Hückel theory to model this effect and accurately reproduce experimental measurements of the specific heat with no adjustable parameters.

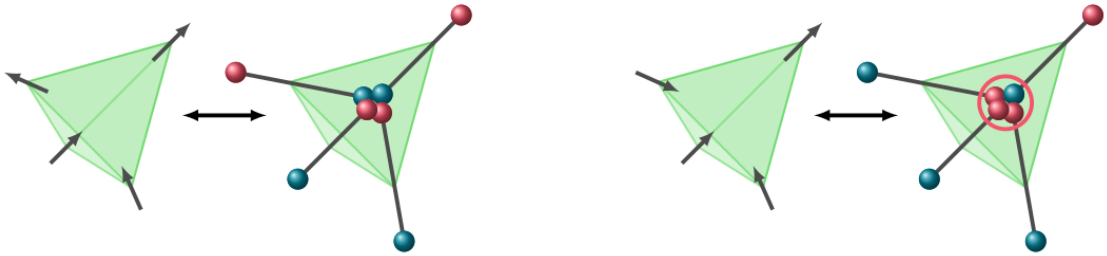

Figure 1.2.3: Dumbbell model: (left) the spins are promoted as dumbbells with one magnetic "north" charge and one "south" charge. (right) When the ice rule is broken, the sum of the magnetic charges on the tetrahedron is not zero, creating a monopole which moves on the diamond lattice. From [Raban, 2018]

Let us now focus on the energetics of the dumbbell model at $T = 0$ K to understand the effect of Coulomb interactions on the competition between a vacuum of monopoles (i.e. spin ice) and a crystal of monopoles. The coulombic internal energy of a crystal of monopoles can be computed exactly as

$$\mathrm{U_c} = \frac{\mu_0 Q^2}{8\pi}\sum_r\left(\sum_{I\neq J}\frac{(-1)^{\eta_J}}{|\mathbf{r}_{IJ}|}\right) \tag{1.2.10}$$

where η_r is an index which is even (odd) on the A (B) diamond sublattice respectively. The sum in between parenthesis is purely geometric and only depends on the lattice structure. It can be expressed as a function of the diamond lattice constant a as

$$\sum_{q\neq r}\frac{(-1)^{\eta_J}}{|\mathbf{r}_{IJ}|} = -\frac{a}{\alpha} \tag{1.2.11}$$

where α is called the Madelung constant of the lattice and has an approximate value of 1.638 for the diamond lattice. Therefore the energy for a system of N tetrahedra reads

$$\mathrm{U_c} = \alpha \frac{\mu_0 Q^2}{8\pi a} N \tag{1.2.12}$$

On the other hand the Coulomb interaction between two nearest neighbors monopoles is

$$u(a) = -\frac{\mu_0 Q^2}{4\pi a} = -\frac{8}{3}\sqrt{\frac{2}{3}} D \tag{1.2.13}$$

hence the energy of the monopole crystal can be rewritten as

$$\mathrm{U_c} = \frac{1}{2} u(a) \alpha N \tag{1.2.14}$$

This negative energy competes with the energy cost of creating a monopole crystal $-\nu N$ (> 0) such that the spin ice states prevails for

$$\nu \leqslant \frac{1}{2} u(a) \alpha \tag{1.2.15}$$

$$\frac{-\nu}{|u(a)|\alpha} \geqslant \frac{1}{2} \tag{1.2.16}$$

Finally we express this condition in terms of the DSI model parameters by using the relevant Equations (1.2.9) and (1.2.13) and rearranging the terms:

$$\frac{J_{nn}}{D_{nn}} = \frac{J}{5D} \geqslant -\frac{4}{5}\left[1 + \sqrt{\frac{2}{3}}\left(1 - \frac{\alpha}{2}\right)\right] \approx -0.92 \tag{1.2.17}$$

This is in excellent agreement with the Monte-Carlo simulations of the DSI model [Melko et al., 2001], which yielded a critical $J_{nn}/D_{nn} \approx -0.91$ as shown in Figure 1.2.2. The origin of the difference is the manifold of spin ice states which are all assumed to have the same energy in the dumbbell model. This discussion proves that in addition to being necessary to stabilize a spin ice phase in $Ho_2Ti_2O_7$ and $Dy_2Ti_2O_7$, long-range dipolar interactions are also important to understand the magnetically ordered simple or double monopole crystal phases. However they can not lead to a fragmented ground state by themselves: as $-\nu/|u(a)|\alpha$ is lowered below 1/2 (or equivalently J_{nn}/D_{nn} is lowered below -0.91), the Coulomb energy favors the double monopole crystal as it is always 4 times larger than that of a single monopole crystal. In order to find the fragmented monopole crystal, several options have been considered. One proposal was to study a weak double monopole crystal near its second order transition to a paramagnet, where the fragmented phase would be stabilized by thermal fluctuations [Guruciaga et al., 2014]. Another was to find a material where the quantum fluctuations would be strong enough in the ground state to lift the $\nu_2 = 4\nu$ in the ground state [Brooks-Bartlett et al., 2014].

1.2.4 Fragmentation in pyrochlore iridates

As in all pyrochlore materials, the Ti^{4+} ions in $Dy_2Ti_2O_7$ and $Ho_2Ti_2O_7$ lie on their own pyrochlore lattice intercalated in the rare-earth lattice. Populating this second lattice with magnetic atoms instead offers an opportunity to manipulate the rare-earth spins with local fields rather than external magnetic fields, thus preserving more of the lattice's symmetries and the geometrical frustration. This was realized in $Ho_2Ir_2O_7$ and $Dy_2Ir_2O_7$ [Lefrançois et al., 2017; Cathelin et al., 2020; Lhotel et al., 2020]. Iridium is a $5d$ metal which in its 4+ valence has a $5d^5$ configuration. In Figure 1.2.4 we show the various splittings acting on this orbital in a perturbative picture. The $5d$ orbital is first split by the crystal field from the octahedral Oxygen environment into t_{2g} and e_g orbitals, of which only the former is occupied. It is then further split by the spin-orbit coupling into two degenerate non-magnetic $j_{\text{eff}} = 3/2$ orbitals, and one $j_{\text{eff}} = 1/2$ orbital occupied by a single electron and therefore magnetic. The electronic correlations between Ir^{4+} ions are of the same order of magnitude as the spin orbit coupling. They drive the iridium sublattice to order into a magnetic insulating state, through a metal-insulator transition at a temperature of about 140 K which is much higher than the rare-earth interactions. The structure is an antiferromagnetic all-in / all-out one, where each ion carry a spin $\frac{1}{2}$ along the local $\langle 111 \rangle$ axes.

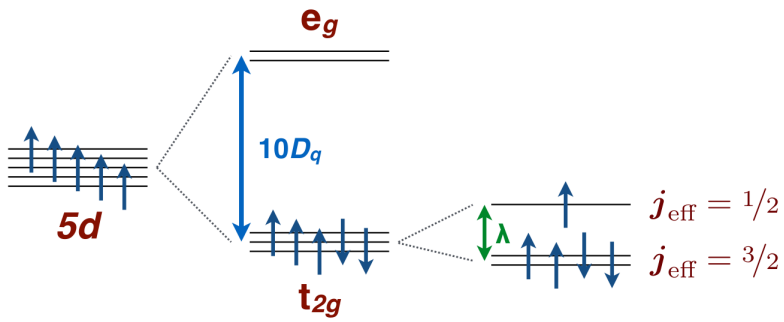

Figure 1.2.4: Orbital occupation of the Ir^{4+} ion, reproduced from [Lefrançois, 2016]

Let us now focus on what effect this magnetic order has on the rare-earth sublattice. Each rare-earth ion is surrounded by 6 nearest Iridium neighbors arranged in an hexagon, represented in Figure 1.2.5. They produce on the rare-earth a molecular field which mimics their magnetic structure, namely a local field $\mathbf{B}_{\text{loc}}$ along the rare-earth local axes in an all-in / all-out fashion. We can model this effect by a local Zeeman term in the spin Hamiltonian:

$$-g\mu_B \sum_i \mathbf{B}_{\text{loc}} \cdot \mathbf{S}_i \tag{1.2.18}$$

which can be translated in the dumbbell picture into a *staggered chemical potential* for the monopoles:

$$-\eta_r g\mu_B B_{\text{loc}} a \sum_r Q_r = -\eta_r \Delta \sum_r n_r \text{ with } \Delta = 2g\mu_B B_{\text{loc}} \mu \tag{1.2.19}$$

This term is antisymmetric under global spin inversion which reverses the A/B diamond sub-

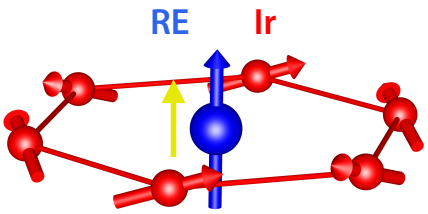

Figure 1.2.5: Rare-earth ion (in blue) and its hexagon of nearest Ir neighbors (in red). They create a molecular field pictured by the yellow arrow

lattice convention. Hence when positive, it promotes positive magnetic charges on diamond sublattice A and negative on sublattice B respectively. Thus, it changes the monopole (ν) and double monopole (ν_2) local chemical potentials as follows:

$$\nu \to \nu \pm \Delta, \;\; \nu_2 = 4\nu \to 4\nu \pm 2\Delta$$

depending on the diamond sublattice. For a non zero Δ like in $Ho_2Ir_2O_7$ and $Dy_2Ir_2O_7$ this allows for the single monopole crystal to be the minimum energy state. In the next section we will study in more details phase diagram and transitions between ground states.

	J (K)	D (K)	B_{loc} (T)
$Dy_2Ir_2O_7$	≈ -3.7	1.4	≈ 0.9
$Ho_2Ir_2O_7$	≈ -2.5	1.4	0.94

Table 1.2.3: Approximated values of the coupling constants and local fields obtained for $Dy_2Ti_2O_7$ and $Ho_2Ti_2O_7$, from [Lefrançois et al., 2017; Cathelin et al., 2020; Lhotel et al., 2020]

1.2.5 Phase diagram of fragmentation

In order to compare various pyrochlore materials with different spins and lattice constants, reduced dumbbell model parameters have been defined by dividing by $|u(a)|\alpha$ such that

$$\bar{\nu} = -\frac{\nu}{|u(a)|\alpha}, \bar{\Delta} = \frac{\Delta}{|u(a)|\alpha}, \bar{T} = \frac{k_B T}{|u(a)|\alpha} \tag{1.2.20}$$

The sign of $\bar{\nu}$ was changed to better represent the fact that it is the energy cost for creating monopoles. At zero temperature we can compare the energies of a perfect vacuum of charge, monopole crystal and double monopole crystal in theses reduced units to get the phase diagram. They are respectively

$$\bar{E}_0 = 0, \bar{E}_1 = -\frac{1}{2} + \bar{\nu} - |\Delta|, \bar{E}_2 = -\frac{1}{2} + 4\bar{\nu} - 2|\Delta| \tag{1.2.21}$$

Therefore the monopole crystal is stable for

$$\frac{1}{3} < \frac{\bar{\nu} - \frac{1}{2}}{\left|\bar{\Delta}\right|} < 1 \tag{1.2.22}$$

whereas the ground state is a double monopole crystal if this ratio is smaller than 1/3 and a spin ice if bigger than 1. This condition is pictured on the phase diagram in Figure 1.2.6 (left) where the ground states are separated by first-order transitions. The fact that $\bar{\nu}$ has a lower limit of 1/2 for a spin ice to exist is a remnant of the long-range dipolar interactions.

The parameters of the dumbbell model for $Dy_2Ti_2O_7$, $Dy_2Ir_2O_7$, $Ho_2Ti_2O_7$ and $Ho_2Ir_2O_7$ are shown below in Table 1.2.4. As represented in Figure 1.2.6 (left) they are consistent with both pyrochlore iridates being located deep into the fragmented monopole crystal phase. However some differences between Holmium and dysprosium pyrochlore are worth noting. Dysprosium pyrochlores generally have a lower $\bar{\nu}$ which corresponds to a more long-range interacting behavior. This places them closer to phase transitions in the phase diagram. In particular $Dy_2Ir_2O_7$ could be the most promising material in which to observe a fragmentation phase transition, but the precise determination of the parameters in the dumbbell model is difficult.

	ν (K)	Δ (K)	$\bar{\nu}$	$\bar{\Delta}$
$Dy_2Ti_2O_7$	-4.4	0	0.9	0
$Dy_2Ir_2O_7$	≈ -4.4	≈ 4.95	≈ 0.9	≈ 1.0
$Ho_2Ti_2O_7$	-5.7	0	1.2	0
$Ho_2Ir_2O_7$	≈ -5.4	6.3	≈ 1.1	1.3

Table 1.2.4: Approximated values of the dumbbell model obtained for $Dy_2Ti_2O_7$ and $Ho_2Ti_2O_7$, from [Lefrançois et al., 2017; Cathelin et al., 2020; Lhotel et al., 2020]

The general structure of the phase diagram was investigated numerically in [Raban, 2018; Raban et al., 2019] and is shown in Figure 1.2.6. It can be understood as a three-dimensional extension to the DSI model phase diagram, where the possible ground states are separated by nearly vertical "wings" of first-order transitions (in light green). Once again they are a signature of the long-range interactions in the system, as numerical studies of fragmentation in the nearest-neighbor model only found evidence of crossovers between the phases [Lefrançois et al., 2017]. As the temperature increases the first order transitions terminate on a line of critical end points where second-order transitions occur (in dark green). These lines then join in the multicritical region where $\Delta = 0$, $\bar{\nu} \approx 1/2$. Several scenarii are possible: the wings could all meet together in an exotic pentacritical point at $\Delta = 0$ where all five phases can coexist, or separately in a set of tricitical points where only three phases coexist at once. Careful considerations of the entropy of the different phases revealed that in the dumbbell model the wings join in two stages, once at $\Delta \neq 0$ then at $\Delta = 0$ with three tricitical points. Indeed this model at $\Delta = 0$ only has two variables $\bar{\nu}$ and $\bar{T}$ so any pentacritical point would be accidental. However such a point could be tuned into the model by introducing a new variable like the cost of double monopoles $\bar{\nu}_2$ which would be different from $4\bar{\nu}$.

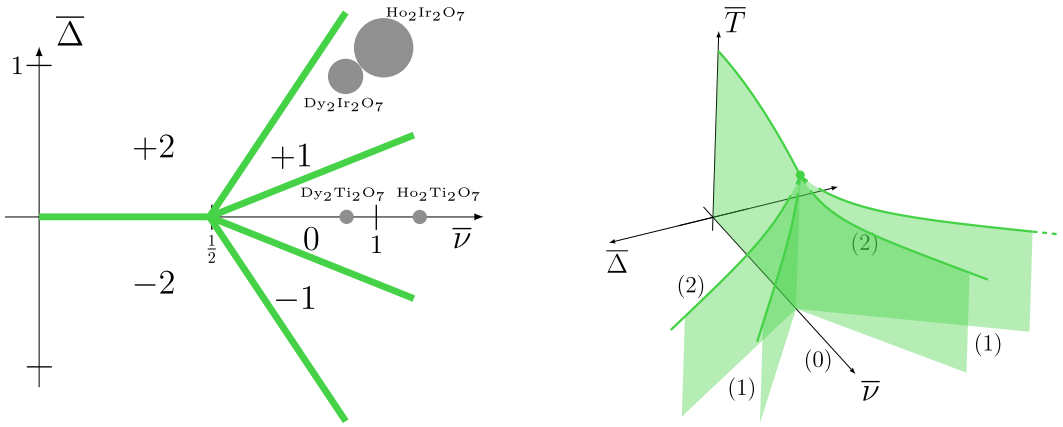

Figure 1.2.6: (left) Phase diagram of the dumbbell model at $T = 0$ K and (right) as a function of temperature. Figures adapted from [Raban et al., 2019]

1.2.6 Mean-field theory of fragmentation

In order to get a free energy for fragmentation a mean-fiel approach has been derived in [Raban, 2018; Raban et al., 2019]. It revolves around a mapping of the dumbbell model Hamiltonian to a simpler one, the Blume-Capel model, which is the simplest model which exhibits a tricritical point. It essentially truncates the long-range interaction to the nearest-neighbor level. For simplicity the authors limited themselves to the case of single monopoles. They define degrees of freedom $S_I = 0, \pm 1$ on the diamond lattice which represent the monopole occupation state of site I, and consider the following Blume-Capel Hamiltonian:

$$\mathscr{H}_{\text{Blume-Capel}} = \frac{1}{4}\frac{|u(a)|\alpha}{2}\sum_{\langle I,J\rangle} S_I S_J + \nu\sum_I S_I^2 - \Delta\sum_I \eta_I S_I \tag{1.2.23}$$

$$\bar{\mathscr{H}} = -\frac{1}{8N}\sum_{\langle I,J\rangle} S_I S_J + \frac{\bar{\nu}}{N}\sum_I S_I^2 - \frac{\bar{\Delta}}{N}\sum_I \eta_I S_I \tag{1.2.24}$$

where the $1/4$ factor accounts for the connectivity of the diamond lattice and N is the number of sites. The second line is rewritten as an energy per site with the reduced parameters discussed above. Two mean field variables are then introduced: ρ the average density of monopoles and ϕ their crystallization parameter, representing their propensity to be located on the A/B sublattice. They are defined from number of $\pm$ monopoles on sublattice through

$$\frac{N_{A,\pm}}{N} = \rho\left(\frac{1\pm\phi}{2}\right), \frac{N_{B,\pm}}{N} = \rho\left(\frac{1\mp\phi}{2}\right), \frac{N_0}{N} = 1-\rho \tag{1.2.25}$$

Within this approach, the product $\rho\phi$ is a good parameter to tell apart the two phases of interest: it is close to 0 in a spin ice phase and close to 1 in a monopole crystal. Placing ourselves in the grand canonical ensemble for monopoles and perform a mean-field procedure on the Blume-Capel Hamiltonian in order to get a grand potential. We will first take care of the enthalpy, then the entropy.

The sums are split into separate sums over A and B sublattices, then replaced by their mean-field value:

$$\begin{aligned}\sum_I S_I^2 &= \sum_{I\in A} S_I^2 + \sum_{I\in B} S_I^2 \approx N\rho \\ \sum_I S_I &\approx N\rho\phi \\ \sum_{\langle I,J\rangle} S_I S_J &= \sum_{I\in A} S_I \left(\sum_{\substack{J\in B \\ J \text{ nn } I}} S_J\right) \approx 4N(\rho\phi)^2\end{aligned} \tag{1.2.26}$$

so that we end up with the following mean-field enthalpy per site for the monopoles:

$$\bar{H} \approx -\frac{1}{2}\rho^2\phi^2 + \bar{v}\rho - \bar{\Delta}\rho\phi \tag{1.2.27}$$

To compute the entropy, we use the same combinatorics than in Equation (1.1.5), meaning we consider N independent tetrahedron. However, in addition to the 6 two in / two out tetrahedron corresponding to a vacuum of monopoles ($\{N_1,\dots,N_6\}$) we include this time $4+$ ($\{N_7,\dots,N_{10}\}$) and $4-$ ($\{N_{11},\dots,N_{14}\}$) single monopoles states . Each of the 14 states is considered equiprobable and have densities

$$N_1 = \cdots = N_6 = (1-\rho)\frac{N}{6},\ N_7 = \cdots = N_{10} = \rho\left(\frac{1+\phi}{2}\right)\frac{N}{4},\ N_{11} = \cdots = N_{14} = \rho\left(\frac{1-\phi}{2}\right)\frac{N}{4} \tag{1.2.28}$$

The number of states reads similarly

$$W = \left(\frac{1}{2}\right)^{2N} \frac{N!}{N_1!\dots N_{14}!} \tag{1.2.29}$$

So that using Stirling's formula we end up for the following expression of the entropy per tetrahedron:

$$\bar{S} = \frac{S}{N k_B} = -\rho\frac{1+\phi}{2}\ln\left(\rho\frac{1+\phi}{2}\right) - \rho\frac{1-\phi}{2}\ln\left(\rho\frac{1-\phi}{2}\right) + (1-\rho)\ln(1-\rho) + (1-\rho)\ln\left(\frac{3}{2}\right) \tag{1.2.30}$$

The last term is the one that makes this entropy different from that of a gas on a bipartite lattice: it yields the Pauling entropy when $\rho = 0$. It is interesting to note that the entropy is negative for some parameter values like $\rho = 1, \phi = 0$. This nonsensical result is the sign of a breakdown of Stirling's approximation when the corresponding number of microstates W becomes to small. In total we get the following grand potential for the monopoles:

$$\begin{aligned}\bar{\Omega} &= \bar{H} - \bar{T}\bar{S} \\ &= -\frac{1}{2}\rho^2\phi^2 + \bar{v}\rho - \bar{\Delta}\rho\phi + \bar{T}\left(\rho\frac{1+\phi}{2}\ln\left(\rho\frac{1+\phi}{2}\right) + \rho\frac{1-\phi}{2}\ln\left(\rho\frac{1-\phi}{2}\right) + (1-\rho)\ln(1-\rho) + (1-\rho)\ln\left(\frac{3}{2}\right)\right)\end{aligned} \tag{1.2.31}$$

This potential can be minimized numerically to draw a minimal phase diagram of fragmenta-

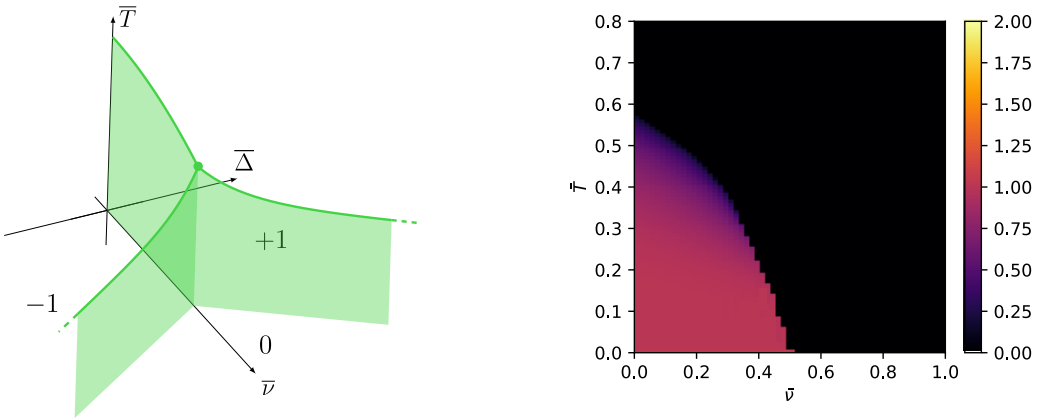

Figure 1.2.7: (left) Phase diagram of the mean field theory of fragmentation as a function of temperature and staggered chemical potential. (right) Plot of the order parameter at $\bar{\Delta} = 0$.

tion. Compared to the one studied previously in Figure 1.2.6, it neglects any double monopole excitation or phase. But the general structure of the phase diagram remains similar: we find the spin ice and monopole crystal phases are separated at low temperature by wings of first order transitions, terminated by lines of second-order transitions, which meet at a critical end point. The schematic phase diagram, as well as a cut for $\Delta = 0$ solved numerically, are shown in Figure 1.2.7. Despite its shortcomings, it highlights an important feature: the barriers of first order transition are not not completely independent on temperature. They are angled in a way that represent the difference in entropies between the low-temperature phases they separate. Indeed, the Clausius-Clapeyron relation reads:

$$\frac{\mathrm{d}\bar{\Delta}_{tr}}{\mathrm{d}\bar{T}} = -\frac{\delta\bar{S}}{\delta(\rho\phi)} \tag{1.2.32}$$

where $\delta(\rho\phi)$ is the difference in order parameter between the two sides of the transition, $\delta\bar{S}$ is the difference in entropy per tetrahedron and $\bar{\Delta}_{tr}$ is the staggered chemical potential at the transition. Therefore at fixed $\bar{\nu}$, $\bar{\Delta}_{tr}$ will increase slightly as a function of temperature because of the difference between the Pauling and monopole crystal residual entropies. Equivalently, at fixed $\bar{\Delta}$ $\bar{\nu}_{tr}$ will decrease slightly as shown in Figure 1.2.7 (right). The angle from the vertical is overestimated there because our mean-field model does not include the residual entropy of the monopole crystal. The tricritical where all phases join is located at a temperature of $\bar{T} = \frac{1}{3}$, which is also overestimated compared to the Dumbbell model. This is because the long-range coulombic interactions in the monopole fluid phase have not been taken into account.

1.3 Going beyond Ising pyrochlores: magnetic phases and quantum effects

1.3.1 Symmetry-allowed two-dipoles interactions

In this section we want to explore the physics of pyrochlore magnets going beyond Ising spins. This means that we first allow each spin to have three classical components S^x, S^y, S^z expressed in the local axes, which we assume transform like dipoles. We will then promote to quantum operators to study quantum effects. At the nearest-neighbor level, they interact through a Hamiltonian which is constrained by the symmetry of the pyrochlore lattice. More precisely, its matrix elements must be left invariant by all the operations of the space group of the lattice. This results in only 4 distinct allowed nearest neighbours couplings which can be expressed in various frames. The frame attached to the bond between two neighboring magnetic ions is where the four fundamental interactions are most naturally expressed:

- Ising with respect to the local bond;
- XY with respect to the local bond;
- Symmetric off-diagonal exchange;
- Dzyaloshinski-Moriya exchange.

In this work we will instead use the local pyrochlore frame, because it highlights the spin ice physics. We keep the same local z as out of an A-type tetrahedron and define x, y local axes at each pyrochlore site. The four parameters are expressed as $J_{zz}, J_{\pm}, J_{z\pm}, J_{\pm\pm}$ and the Hamiltonian reads:

$$\mathscr{H}_{\text{local}} = \sum_{\langle i,j \rangle} J_{zz} S_i^z S_j^z - J_{\pm} \left(S_i^+ S_j^- + S_i^- S_j^+ \right) + J_{\pm\pm} \left(\gamma_{ij} S_i^+ S_j^+ + \gamma_{ij}^* S_i^- S_j^- \right) + J_{z\pm} \left[S_i^z \left(\zeta_{ij} S_j^+ + \zeta_{ij}^* S_j^- \right) + i \leftrightarrow j \right] \tag{1.3.1}$$

where γ and ζ are matrices which encode the transition from one bond to another:

$$\zeta = \begin{pmatrix} 0 & -1 & e^{i\pi/3} & e^{-i\pi/3} \\ -1 & 0 & e^{-i\pi/3} & e^{i\pi/3} \\ e^{i\pi/3} & e^{-i\pi/3} & 0 & -1 \\ e^{-i\pi/3} & e^{i\pi/3} & -1 & 0 \end{pmatrix} = -\gamma^* \tag{1.3.2}$$

1.3.2 $\mathbf{Q} = 0$ pyrochlore magnetic orders from group representations theory

The theory of group representations is a powerful tool in the study of magnetic ordering. It makes it possible to predict the various $\mathbf{q} = 0$ structures allowed by symmetry on a certain lattice. It has been applied successfully in Ref [Yan et al., 2017] in the case of a pyrochlore lattice with classical dipolar spins, and we will briefly restate here the main conclusions. All the $\mathbf{q} = 0$ classical orders on the pyrochlore lattice can by definition be described by the set of the orientations of 4 spins on the vertices of a given tetrahedron, each having 3 components. The energy

of any configuration can therefore be computed by multiplying the vector of components by a 12×12 Hamiltonian matrix. As mentioned before, this matrix elements are constrained by the symmetries of the pyrochlore lattice. Since we consider only $\mathbf{q} = 0$ orders, the translation symmetry is already included and we replace the space group by the point group of the unit cell. The point group of the pyrochlore lattice is $O_h = T_d \times I$ where T_d is the symmetry group of a single tetrahedron and I is the inversion operation between up and down tetrahedra. The main interest of representation theory is that it can be now used to block-diagonalize the Hamiltonian into blocks, whose components transform under the four non trivial irreducible representations of T_d: $\{\Gamma_3, \Gamma_5, \Gamma_7, \Gamma_9\}$ of respective dimensions are 1, 2, 3, and 3 respectively. These representations are also called $\{A_2, E, T_2, T_1\}$.

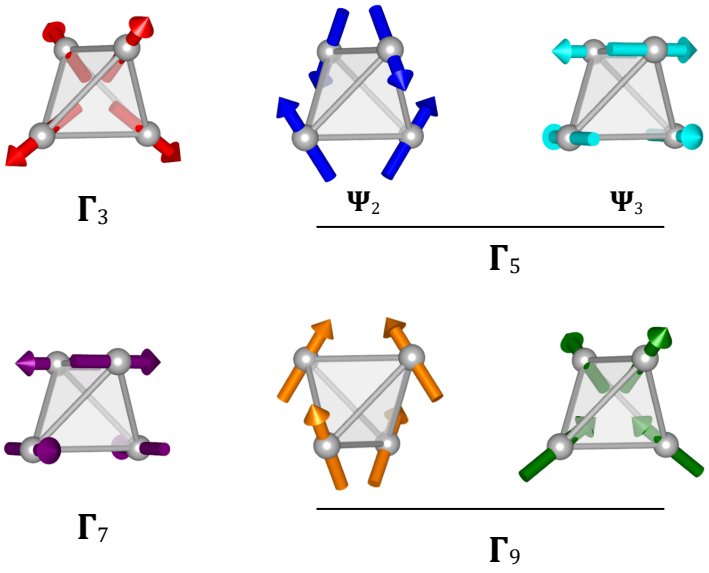

Figure 1.3.1: Possible magnetic orders on the pyrochlore lattice, grouped by representations.

The precise decomposition depends on the type of objects we populate the pyrochlore lattice with: pure dipoles, dipolar-octupolar doublets for Kramers ions, non Kramers doublets, pure quadrupoles, etc. For our case of classical dipoles the decomposition of the Hilbert space reads

$$\Gamma_3 \oplus \Gamma_5 \oplus \Gamma_7 \oplus 2\Gamma_9 \tag{1.3.3}$$

with two instances of the Γ_9 representation, which does result in a total of 12 dimensions. The eigenvectors $\mathbf{m}_{\Gamma_i}$ of each representations can be interpreted as the order parameters of a particular type of ordering, shown in Figure 1.3.1:

- $\mathbf{m}_{\Gamma_3}$ (of dimension 1) corresponds to the all-in / all-out moment, also called m in other texts;

- $\mathbf{m}_{\Gamma_5}$ (of dimension 2) to the "all x / all y" easy plane antiferromagnetic order. Its two basis states are called Ψ_2 and Ψ_3;
- $\mathbf{m}_{\Gamma_7}$ (of dimension 3) to the so-called Palmer-Chalker order;
- $\mathbf{m}_{\Gamma_9^A}$ and $\mathbf{m}_{\Gamma_9^B}$ (also of dimension 3) are both ferromagnetic structures, corresponding for the first one to the ordered spin ices states, and for the other to a conventional colinear ferromagnet.

The eigenvalues a_{Γ_i} given by the diagonalization procedure are the energy costs of theses orders, computed from J the parameters described above. In concept, this approach is similar to the diagonalisation of a tight-binding Hamiltonian in $\mathbf{k}$-space, leading to several bands. The result is that the exchange Hamiltonian can be rewritten in a simpler form:

$$\mathscr{H} = \frac{1}{2}\left(a_{\Gamma_3} m_{\Gamma_3}^2 + a_{\Gamma_5}\mathbf{m}_{\Gamma_5}^2 + a_{\Gamma_7}\mathbf{m}_{\Gamma_7}^2 + a_{\Gamma_9^A}\mathbf{m}_{\Gamma_9^A}^2 + a_{\Gamma_9^B}\mathbf{m}_{\Gamma_9^B}^2 + a_{\Gamma_9^{AB}}\mathbf{m}_{\Gamma_9^A}\cdot\mathbf{m}_{\Gamma_9^A}\right) \tag{1.3.4}$$

One important note is that this rewriting is mathematically equal to the original Hamiltonian, and not a Landau free energy obtained through an averaging procedure. It is composed of a sum of quadratic terms for each type of ordering, as well as one coupling allowed by symmetry between the two order parameters that transform under the same representation Γ_9. To find the magnetic structure, one must add a constraint of fixed length to each spin. We can highlight some simple examples:

- $a_{\Gamma_3} = 3J_{zz}$, an all-in / all-out order is stabilized if the effective Ising exchange < 0;
- $a_{\Gamma_5} = -6J_{\pm}$, so an easy-plane antiferromagnetic order of representation Γ_5 is stabilized if $J_{\pm} > 0$. Within this description it turns out that any superposition of the two basis vectors Ψ_2, Ψ_3 of Γ_5 have the same energy; it has been shown that a ground state is thermally selected by an order-by-disorder mechanism [Yan et al., 2017].

So far in this discussion we have ignored longer range interactions. It turns out that introducing further neighbors two-spins coupling in Equation (1.3.1) only results in renormalized values of the nearest-neighbor couplings. This is because in the $\mathbf{Q} = 0$ order picture long range interactions are projected on the 4-site unit cell, and so the results of the group representation analysis hold as well when considering material with significant dipolar interactions. However they become irrelevant when the ordered state has a propagation vector $\mathbf{Q} \neq 0$, such as in dipolar spin ice at low temperature.

1.3.3 Quantum effects and perturbation theory

There are several theoretical frameworks that can be used on quantum frustrated magnets: Schwinger bosons [Sachdev, 1995; Moessner et al., 2003b], partons with gauge-mean field theory [Savary et al., 2012; Savary et al., 2017b], bosonic many-body theory [Hao et al., 2014], perturbation theory [Bergman et al., 2007b; Bergman et al., 2006; Bergman et al., 2007a]. We will

mostly use the latter, with a simple mapping from spins to hardcore bosons in order to get similar quantum dimer models for various scenarios. In this thesis we will consider spin $\frac{1}{2}$ pseudospins $\left\{\hat{S^x}, \hat{S^y}, \hat{S^z}\right\}$. We limit ourselves to quantum fluctuations induced by a $J_\pm$ term, keeping $J_{zz} > 0$ as the frustrated exchange. This is known as the XXZ model, which we will apply to the pyrochlore and kagome lattices:

$$\mathscr{H} = \sum_{\langle i,j \rangle} J_{zz} \hat{S}_i^z \hat{S}_j^z - J_\pm (\hat{S}_i^+ \hat{S}_j^- + \hat{S}_i^- \hat{S}_j^+) \tag{1.3.5}$$

This mapping simply consists in replacing a spin by a boson if the spin is in a + state and a vacuum in the − state. For example,

$$\hat{S}_i^+ = a_i^\dagger,\ \hat{S}_i^- = a_i,\ \hat{S}_i^z = a_i^\dagger a_i - \frac{1}{2} \tag{1.3.6}$$

because $[\hat{S}^+, \hat{S}^-] = 2\hbar \hat{S}^z$. However these bosons don't quite have the same commutations relations as usual canonical bosons, although they commute on different sites:

$$[a_i, a_j^\dagger] = \delta_{ij}(1 - 2a_i^\dagger a_i) \tag{1.3.7}$$

It is nevertheless possible to realize the same matrix elements as the spin Hamiltonian by imposing a canonical commutation relation and a hardcore repulsion between bosons

$$U \sum_i \left(a_i^\dagger a_i - \frac{1}{2} \right)^2$$

with $U \to +\infty$: such a term limits the number of bosons per site at 0 or 1, thus giving back the two states of a spin $\frac{1}{2}$. This might seem like a standalone trick but it is representative of a common approach in quantum condensed matter: enlarge the Hilbert space (i.e. allow formally more than one boson per site) to lift a constraint (here the unusual commutation relation in Equation (1.3.7)), then project it back onto the physical states.

Injecting the hardcore boson definitions into the XXZ Hamiltonian, one finds that it can be rewritten as:

$$\mathscr{H} = -J_{zz} \sum_i a_i^\dagger a_i - J_\pm \sum_{\langle i,j \rangle} a_i^\dagger a_j + a_j^\dagger a_i + J_{zz} \sum_{\langle i,j \rangle} a_i^\dagger a_i a_j^\dagger a_j + U \sum_i a_i^\dagger a_i^\dagger a_i a_i + \text{cte} \tag{1.3.8}$$

These bosons can be seen as the quantum equivalent of the dimers associated to the emergent field. They live on the links of the diamond lattice for pyrochlore spin ice (or hexagonal lattice for kagome spin ice), and they hop in ways that preserve the local constraint at low energy. With this mapping, non-fragmented and fragmented pyrochlore spin ice are represented by different hard-core boson fillings:

- On the pyrochlore lattice:
  - An AIAO state corresponds to having all pyrochlore sites occupied by a boson or empty;

  - a spin ice state corresponds to having 2 surrounding each diamond site, hence the system is at (local) half-filling;
  - a fragmented ice state corresponds to having 1 or 3 bosons surrounding each diamond site, hence (local) quarter-filling.

- On the kagome lattice:
  - An AIAO state corresponds to having all kagome sites occupied by a boson or empty;
  - a spin ice / magnetic charge crystal corresponds to 1 or 2 bosons surrounding each hexagonal site, hence (local) third-filling

The monopoles excitation correspond to vacancies or supplementary bosons. It is interesting to note that the J_{zz} terms translates to a repulsion between neighboring bosons and a chemical potential. Therefore, the perturbative limit $J_{\pm} \ll J_{zz}$ can be seen as going to the grand canonical ensemble, with a globally fixed number of hard-core bosons, and a large repulsion between neighbors.

The hardcore boson Hamiltonian obtained above can then be projected onto the degenerate ground space manifold, by removing the defects excitations and fixing the number of bosons per site, using degenerate perturbation theory [Bergman et al., 2007b; Bergman et al., 2006; Bergman et al., 2007a]. The equation obtained by this procedure is called the effective Schrödinger equation. We write 1.3.5 in the form $\mathscr{H}_0 + \mathscr{H}_1$. Here $\mathscr{H}_0$ is a classical Hamiltonian. The details of the interactions in it can differ, so long as its ground state is a standard or fragmented spin ice manifold and whose excitations are the magnetic charges or monopoles, with typical energy scale J_{zz}. Most importantly, it is diagonal in the basis of spins operators along the local axis z, such that a ground state can be expressed as a set of $\langle \hat{S}_i^z \rangle$. We call $\mathscr{P}$ the projector on the subspace of all accessible ground states. On the other hand, $\mathscr{H}_1$ contains the small quantum fluctuations of energy scale $J_{\pm}$. The ground sate wavefunction satisfies the equation

$$\left[E_0 + \mathscr{P}\mathrm{H}_1 \sum_n^{+\infty} \left(\frac{1}{E - \mathrm{H}_0} (1 - \mathscr{P}) \mathrm{H}_1 \right)^n \mathscr{P} \right] \left| \Psi_0 \right\rangle = E \left| \Psi_0 \right\rangle = \mathscr{H}_{\text{eff}} \left| \Psi_0 \right\rangle \tag{1.3.9}$$

The operator $\mathscr{R} = \frac{1}{E - \mathrm{H}_0}$ is called the resolvent. Because it contains the exact energy E, this equation is actually a non-linear eigenvalue problem. However, to any given order of the perturbation theory, E may be expanded in a series in $J_{\pm}/J_{zz}$ to obtain an equation with a true Hamiltonian form within the degenerate manifold. Because we will only be interested in the lowest order terms, it is admissible to replace E by E_0 in $\mathscr{R}$, simplifying the problem considerably. We will present the result of this perturbative analysis in the next section, and in the third chapter from the point of view of fragmentation.

1.3.4 Quantum spin ice

The perturbative approach above has been applied to a the XXZ Hamiltonian of a quantum spin ice [Hermele et al., 2004; Benton et al., 2012; Gingras et al., 2014]. The lowest energy term is a

ring exchange process:

$$\mathscr{H}_{\text{eff}} = -\frac{12J_{\pm}^3}{J_{zz}^2} \sum_{\hexagon} \hat{S}_1^+ \hat{S}_2^- \hat{S}_3^+ \hat{S}_4^- \hat{S}_5^+ \hat{S}_6^- \tag{1.3.10}$$

It corresponds to the coherent flip of six spins along a hexagon in the pyrochlore lattice, pictured in Figure 1.3.2 (right). This term promotes spin ice to an analogue of quantum electrodynamics. Indeed, the emergent field **A** defined in Equation (1.1.9) acquires a dynamics driven by the ring exchange Hamiltonian, so that an effective electric field emerges as well: $\mathbf{E} = -\partial\mathbf{A}/\partial t$. In this context the coarse-grained magnetization is commonly named **B** instead of **M**. The emergent quantum theory is formally called a compact $U(1)$ gauge theory. In other words, the potential vector **A** has a local $U(1)$ gauge invariance but its values are bounded, because a hexagonal loop of spins $\frac{1}{2}$ has a maximum winding number. Consequently, it hosts a novel charge-like excitation, called vison, which has no equivalent in classical spin ice. The interaction between the particles of the theory are mediated by gapless bosons with a linear dispersion, which are therefore called effective photons. The energy scales of the various excitations of the theory are shown in Figure 1.3.2 (left). The quantum electrodynamics phase is entered not through a phase transition but a crossover. The most striking signature is that the pinch-points in (quasi)elastic scattering become blurred [Hermele et al., 2004; Benton et al., 2012].

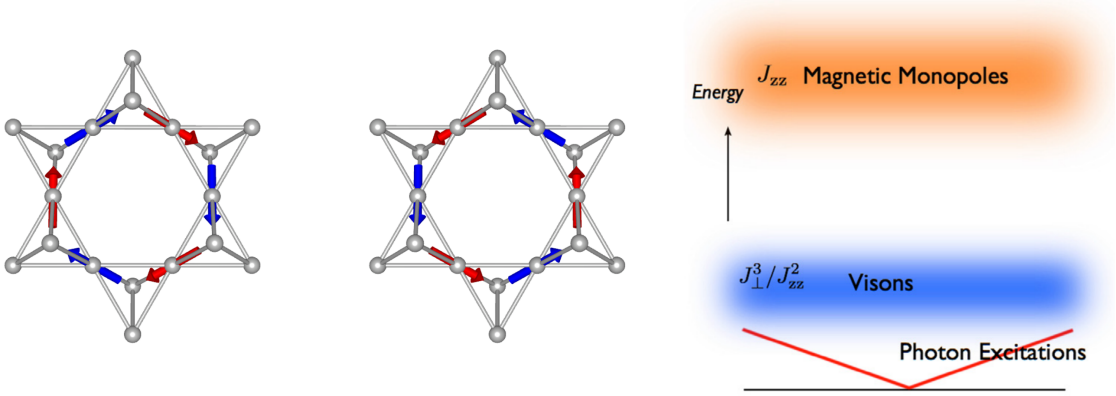

Figure 1.3.2: (left) Ring exchange tunnelling process and (right) Energy scales of the various novel excitations in quantum spin ice.

Chapter 2

Experimental techniques

Contents

2.1 Low temperature

2.1.1 ^{4}He cryogenics

In rare earth pyrochlores, the magnetic exchanges can range from a few tens of milliKelvins for the transverse interactions between some rare-earth, to a hundred Kelvins for the metal-insulator transitions observed with Iridium for example. The study of theses magnetic structures and associated phase transitions therefore requires a suite of cryogenic techniques to reach such low temperatures.

The cryogenic fluid of reference is ^{4}He, which is a liquid at 4.2 K at ambient pressure. Due to its cost and large gas volume generated when boiling, its handling required special care. Cryostats are equipped with screens to limit the thermal losses by the helium vapors, and such vapors are then collected and liquefied on site at the Néel Institute. Like all liquids, the boiling point of helium can be lowered by diminishing the pressure. In the case of ^{4}He this makes it possible to reach temperatures of the order of 1 K through a device called a 1 K pot. By instead using the cool vapors pumped from a bath of ^{4}He, commercial instruments like the MPMS and PPMS from Quantum Design can regulate the sample temperatures from about 2 K to 300 K and are therefore extremely useful for sample characterization.

2.1.2 ^{3}He refrigerator

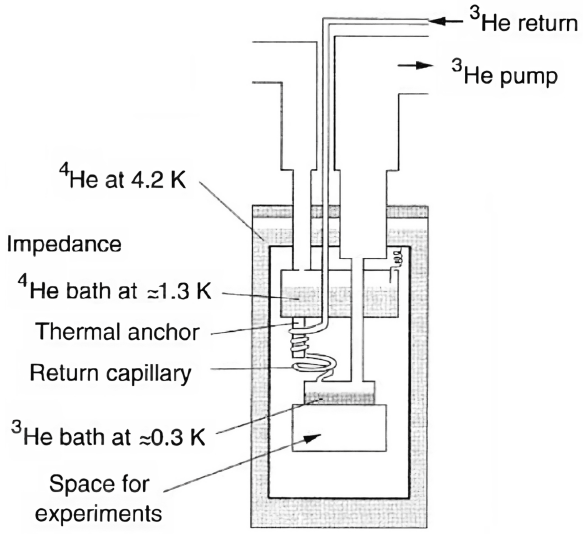

Figure 2.1.1: ^{3}He refrigerator. Figure from Sandia National Labs

To go to temperatures below 1 K, more advanced cryogenic techniques must be used. The simplest idea is to find another cryogenic fluid with an even lower boiling point than ^{4}He. ^{3}He is the only know example, with a boiling point at 3.2 K at atmospheric pressure. Subsequent umping on a liquid ^{3}He bath allows to go to temperatures of the order of 300 mK. However it adds some complexity because ^{3}He is particularly expensive and must be kept clean after

repeated passages through a pump by going through a liquid nitrogen trap. An example of such a ^{3}He refrigerator is shown in Figure 2.1.1. There exists another system, called a sorption pump, which gets rid of moving parts. It cools activated charcoals with liquid ^{4}He and uses its large adsorption capacity to cryopump ^{3}He. This results in much simpler and more reliable cooling system, but has the drawback of only offering a limited time at base temperature, usually of several hours.

2.1.3 Dilution refrigerator

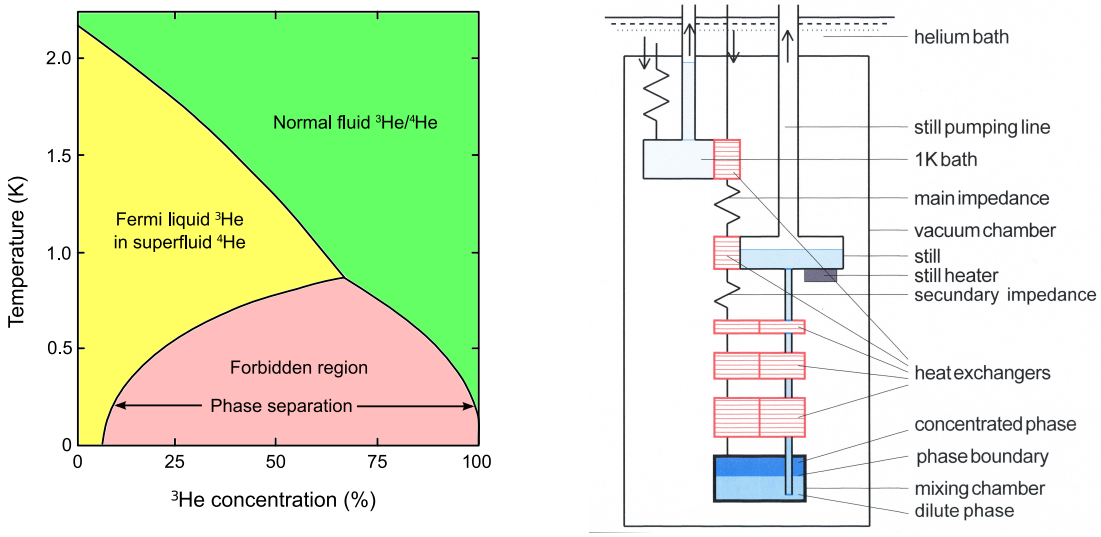

Figure 2.1.2: (Left) Phase diagram of the ^{3}He - ^{4}He mixture. (Righ) Schematics of a dilution refrigerator. Figures reproduced from Wikipedia under CC BY-SA 3.0.

To go to temperatures of the order of the millikelvin for macroscopic samples, the next option is a dilution refrigerator. This cooling technology is much more complex and we will only explain its principle of operation. It relies on the fact that below about 0.87 K a ^{3}He - ^{4}He mixture separates into a ^{3}He-rich phase, called the concentrated phase, and a ^{3}He-poor phase called the dilute phase. This is because the superfluid ^{4}He cannot coexist with a large fraction of ^{3}He below this temperature. The other important point is that ^{3}He has a higher vapor pressure than ^{4}He due to it being slightly lighter. Therefore heating the dilute phase with a small heater results in mostly ^{3}He being evaporated. The general scheme of a dilution refrigerator is shown in Figure 2.1.2. The ^{3}He is pumped at room temperature, then injected and cooled by a heat exchanger with a 1 K pot. At this point it condenses and is pushed through the main impedance which regulates the flow. Then it is cooled by a series of heat exchangers with the still and the ^{3}He being pumped in the dilute phase. It finally reaches the mixing chamber, at the bottom of the cryostat, where the phase boundary between the concentrated and dilute phase is located and to which the sample space is connected. The continuous pumping of ^{3}He pushes it to flow from the concentrated to the dilute phase; like a liquid turning into a gas, this process increases

the entropy of ^{3}He and is therefore endothermic. This is where the cooling power of a dilution refrigerator is generated. The ^{3}He then makes it way in the dilute phase to the still, where it is vaporized by the still heater and pumped to complete the cycle. It is actually the still heater which controls the flow of ^{3}He and not the pumps speed, and therefore regulates the cooling power of the refrigerator.

The dilution canes used on the magnetometer developed by Carley Paulsen and Elsa Lhotel actually slightly differ. The extraction mode of operation for the magnetometer needs the cane to oscillate up and down in the cryostat and so the use of a 1 K pot to cool the ^{3}He is not really possible. Furthermore the study of magnetic phenomena dilution requires to perform temperature ramps up to 4 K, which drives it in an unstable state where all of the mixture is vaporized. The design of these specific canes therefore gets rid of the 1 K pot and injects the mixture at a higher pressure through a higher impedance. However the cooling power is reduced and the sample can only reach a temperature of about 70 mK in the best case scenario. This also makes the cane more susceptible to clogging by a small impurity. There is also the possibility to add the thermal impedance made of brass between the mixing chamber and the sample space, which limits the minimum temperature to about 350 mK but makes the dilution much easier to operate in the $2-4$ K range.

2.2 Specific heat: relaxation time and AC techniques

2.2.1 Definitions and interest

The specific heat of a thermodynamic system (assumed of constant volume) is defined as the ratio between a heat transfer applied to the system δQ and the change in temperature δT per unit of mass:

$$C = \frac{\delta Q}{\delta T} \tag{2.2.1}$$

If there is only heat being exchanged then δQ is related to the entropy change through $\delta Q = T\delta S$. Therefore the knowledge of specific heat over a temperature range allows to compute the entropy difference:

$$\Delta S = \int_{T_1}^{T_2} \frac{C}{T} \mathrm{d}T \tag{2.2.2}$$

The specific heat is also related to the amplitude of fluctuations of the internal energy at a fix temperature. Standard manipulations of the partition function show that

$$C = \frac{\langle U^2 \rangle - \langle U \rangle^2}{k_B T^2} \tag{2.2.3}$$

This expression shows that the specific heat can be interpreted as a type of density of states at a fixed temperature, whereas the integration of $\frac{C}{T}$ counts the total number of available states, consistent with the Boltzmann definition of the entropy.

These theoretical considerations result in the specific heat being a very good probe for phase transitions, formally defined as a non-analyticity of a derivative of the free energy. They can be

classified in two broad classes:

- **Discontinuous** (also called first-order) transitions are characterized by a discontinuity in the entropy, a first-order derivative of the free energy. This results in a instability of the specific heat, and the jump in entropy is associated to a latent heat;
- **Continuous** transitions involve a jump in a further derivative of the free energy. The most common case is a algebraic divergence in the specific heat which is called a second-order transition. Through the lense of renormalization group theory, these transitions can be grouped in several universality classes characterized by a set of critical exponents. For example, the power law fitting the specific heat at the transition defines one such exponent α.

It is therefore paramount to accurately measure the specific heat of a sample. In this thesis we have used two distinct methods which we detail below.

2.2.2 Relaxation time method

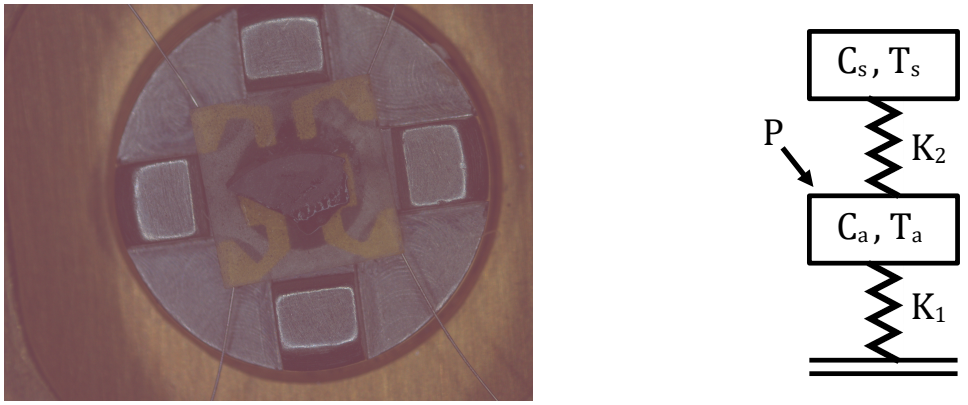

Figure 2.2.1: (left) Picture of a $Ho_2Ru_2O_7$ sample on a ^{3}He Quantum Design PPMS puck and (right) Thermal model of the PPMS system

This method involves heating the sample with a small heating pulse, and measuring the relaxation time when connected through a known thermal leak to a thermal bath at a fixed temperature. This principle of operation is used in the Physical Properties Measurement System (PPMS), built by Quantum Design, which we used to characterize the samples. The sample is fixed to a platform with some Apiezon N grease, which is then connected to the thermal bath with wires.

This platform and the added grease have their own specific heat which are gathered under the umbrella term *addenda*. In Figure 2.2.1 (Left) we show the thermal model of the PPMS, where the sample on top is connected to te platform through a finite thermal leak K_2. This platform has a specific heat C_a accounting for the addenda, and is connected to the thermal bath at temperature T_0 through a known thermal leak K_1. A heating power P is applied to the platform.

The evolution of the temperatures is controlled by the following equations:

$$\begin{aligned} P &= C_a \frac{\mathrm{d}T_a}{\mathrm{d}t} + K_2(T_a - T_s) + K_1(T_a - T_0) \\ 0 &= C_s \frac{\mathrm{d}T_s}{\mathrm{d}t} + K_2(T_s - T_a) \end{aligned} \tag{2.2.4}$$

From this two relaxation times can be defined: the main relaxation time $\tau_1 = (C_s + C_a)/K_1$ corresponding to the overall thermalization of the sample and the platform, and the sample thermalization time $\tau_2 = C_s/K_2$ accounting for a possible temperature difference between the sample and platform. The PPMS control system applies a heating pulse of finite duration to limit the relative amplitude of the temperature change to about 1%. It then fits the temperature measured at the platform using these two relaxation times. If $\tau_1 \gg \tau_2$ then the sample is well coupled. By measuring the addenda specific heat first before placing the sample, the sample specific heat can be readily computed. If however τ_1 and τ_2 are of the same order of magnitude, the sample is decoupled meaning its true temperature evolution cannot be accurately measured. This happens usually at low temperature, either because K_2 becomes too small compared to K_1 or because the sample specific heat increases too much. The PPMS assigns a coupling coefficient to each temperature measured which we use to discard spurious points. When mounting the sample, it is therefore important to use the right sample mass, the least possible amount of grease and to ensure a good thermal connection by lightly pressing the sample into the grease.

2.2.3 Alternative measurement of the heat capacity

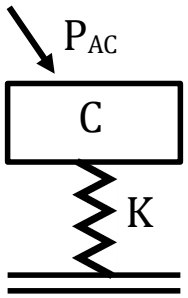

Figure 2.2.2: Simplified thermal model of the AC measurement of the specific heat

When one needs to measure very small samples, the relaxation time method may become unsuitable due to a low signal-to-noise ratio. To make use of the more effective signal processing techniques available for AC signals, an alternative method for measuring specific heat was developed. A sample of heat capacity C is subjected to an alternative heating power by Joule effect at a fixed frequency $P_{AC} = P(1 + \cos 2\omega t)$. It is also coupled to the environment through a thermal leak K. The corresponding simple thermal model is shown in Figure 2.2.2. In this

simple model, the sample temperature oscillations can be written

$$T_{ac} = \frac{P_{AC}}{K + 2j\omega C} \tag{2.2.5}$$

The experimental setup comprises of a synchronous detection which measures the phase difference between the temperature oscillations and the square of the applied voltage. Within this simple model they are

$$\phi = \tan \frac{2\omega C}{K} \tag{2.2.6}$$

Then the specific heat of the sample is

$$C = \frac{P}{2\omega |T_{ac}|} \sin \phi \tag{2.2.7}$$

This system can therefore independently measure the specific heat and the thermal leak to the environment. In particular it is very suited to the measurement of specific heat under pressure: the required pressure media comes with large losses to the environment, but their effect can be minimized with a high enough frequency. This however assumes that the sample stays in equilibirum at a high frequency. On the contrary, a low frequency ensures equilibrium but the phase difference might be so small that it becomes hard to measure. This is why most AC specific heat experiments try to maintain when possible a 45° phase difference working point. The other parameter that must be chosen is the voltage for the temperature oscillations. A higher voltage improves the S/N ratio but can lead to improper thermalization of the sample at the lowest temperatures.

2.3 Magnetometry

2.3.1 Magnetization and susceptibility

Consider a magnetic material, which has a volume magnetization **M** defined as a sum of the internal magnetic moments per unit volume. One the most important quantity to characterize its properties is its susceptibility. It is defined formally defined as a tensor, whose components are the partial derivative of the magnetization components over the applied field strength components:

$$\chi_{ij} = \frac{\partial M_i}{\partial H_j} \tag{2.3.1}$$

In the case of a powder samples, like the one which will be measured in this work this tensor can be simplified to a single scalar susceptibility $\chi = \frac{\partial M}{\partial H}$.

Several main magnetic behaviors are defined from the value of the susceptibility. In Figure 2.3.1 are shown schematic curves of magnetization as a function of field. A paramagnetic material is magnetized only in reaction to an applied field and in the same direction, so it has a slightly positive susceptibility. On the contrary, a diamagnetic material's susceptibility is negative; one striking example is a superconductor which exhibit perfect diamagnetism through

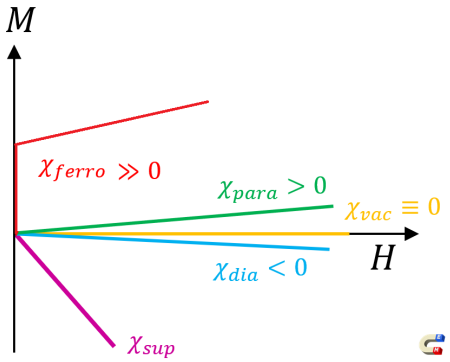

Figure 2.3.1: Illustration of magnetization as a function of field curves for different generic types of magnetism. Figure adapted from Encyclopedia Magnetica under CC-BY-4.0

the Meissner effect. A ferromagnet is defined by a spontaneous magnetization below a certain temperature and so its susceptibility is expected to be orders of magnitudes larger. In the rest of this work, we will use the mass susceptibility, which is the above volume susceptibility divided by the density. We will use CGS units where the magnetic field strength H is expressed in Oe and the mass susceptibility in emu/g.

2.3.2 Susceptibility as a function of temperature

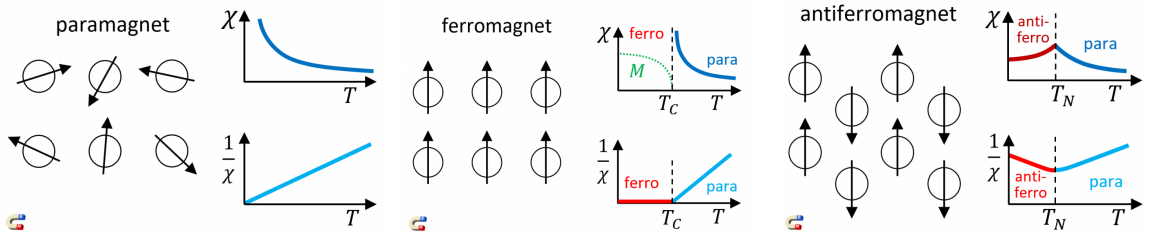

Figure 2.3.2: Schematic illustration of magnetic moments, susceptibility and inverse susceptibility plots for (left) a paramagnet, (center) a ferromagnet and (right) an antiferromagnet. For the ferromagnet the order parameter is plotted below the transition in green. Figure reproduced from Encyclopedia Magnetica under CC-BY-4.0

Upon increasing the magnetic field strength, a magnetic material will reach saturation: its magnetization attains a maximum which gives information on the value of the projected magnetic moment per magnetic atom. But in order to study magnetic transitions, it can be more useful to study the evolution of magnetic susceptibility as a function of temperature. In most cases it is enough to consider the linear susceptibility, i.e. the M/H ratio for small fields of the order of 100 Oe for example. At high enough temperature, most magnetic materials are paramagnetic and follow the so-called Curie-Weiss law:

$$\chi = \frac{C}{T - \Theta} \tag{2.3.2}$$

where C is the Curie constant of the material and Θ is the Curie-Weiss temperature. As an simple example, a two level (Ising) system with effective magnetic moment $\pm\mu_{eff}$ and molar mass M_m has a (mass) Curie constant:

$$C = \frac{\mu_{eff}^2}{k_B M_m} \tag{2.3.3}$$

Susceptibility measurements are often plotted as $1/\chi$ as a function of T, and the scaling law obtained can give important information on the nature of the magnetic moments. On the other hand, the Curie-Weiss temperature Θ is usually of the same scale as the interactions between moments. In non-frustrated magnets, it ends up being close to the transition temperature T_c. From this point of view, a frustration coefficient can defined as the ratio of the Curie-Weiss temperature over the transition temperature:

$$f = \frac{|\Theta|}{T_c} \tag{2.3.4}$$

which is much larger than 1 in frustrated magnets. In Figure 2.3.2 we present several examples of susceptibilities for generic magnetic behaviors. In a paramagnet the moments are disordered and the CW temperature is close to 0. In a ferromagnet, the moments align with each other below a transition temperature and the susceptibility will tend to diverge in an ideal case. In reality, it will saturate a relatively large value compared to the paramagnetic phase. Below the transition, the magnetization acts as an order parameter. However in an antiferromagnet, the spins order but in such a way that there is no overall magnetization. The determination of an order parameter is more complex because it involves dividing the lattice into several sublattices. The Curie-Weiss temperature is actually negative for an antiferromagnet, representative of the opposite sign of the interactions. This makes the susceptibility smaller overall, comparable to that of paramagnets. Below the transition temperature, called the Néel temperature T_N in this case, it tends to decrease towards 0.

We can gain more information on the interactions by looking at the deviations from the Curie-Weiss law just above the phase transition. A larger or smaller χ than what the scaling law indicates the onset of ferromagnetic or antiferromagnetic correlations respectively. Finally, the susceptibility obey a power law just above the transition which defines another critical exponent γ.

These properties represent an idealized sample with no defects or domain walls. In real materials there exists energy barriers which prevent the system to reach a true ground state.They can be estimated experimentally using a so-called ZFC-FC protocol, which takes place in two steps:

- **Zero Field Cooled** (ZFC) the sample is cooled with no magnetic field to the lowest temperature, then the field is applied. If there are significant energy barriers, the moments will be blocked in a given configuration. Only above a certain *freezing temperature* can they order along the field;
- **Field Cooled** (FC) the sample is cooled again with the field still applied. The moments

are polarized from above the freezing temperature and so the state obtained at low temperature will maximize the magnetization.

The comparison of the two measurements can help determine the freezing temperature as well an estimation of the energy barriers.

2.3.3 Susceptibility as a function of frequency

So far all the quantities we have presented are measured in a static fashion. However a lot of information lies in the dynamics of magnetic phases, and the characteristic flipping times for a spin as function of temperature. This is why it is very insightful to apply a small AC field $H(\omega)$ and measure the in-phase and out-of-phase susceptibilities at a fixed temperature, called χ' and χ'' respectively. In the presence of a single relaxation time the complex susceptibility follows a linear model:

$$\chi_{AC} = \chi' + i\chi'' = \chi_S + \frac{\chi_T - \chi_S}{1 + i\omega\tau} \tag{2.3.5}$$

represented in Figure 2.3.3 (top). χ_T is the isothermal susceptibility, equivalent to the DC quantities discussed before. A very high frequency, the spins do not have enough time to align with the field, and so χ tends to a much smaller value called the adiabatic susceptibility χ_S. In between, χ' decreases and χ'' goes through a maximum representing a maximum of dissipation in the sample. The frequency of that maximum represent a characteristic time τ for a spin flip. The evolution of τ as a function of temperature can follow an Arrhenius law, which defines a characteristic fundamental time τ_0 and energy barrier ΔE for a spin flip such that:

$$\tau(T) = \tau_0 e^{-\frac{\Delta E}{k_B T}} \tag{2.3.6}$$

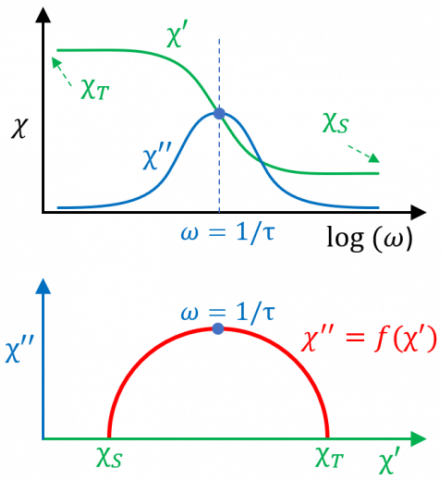

Figure 2.3.3: (top) χ' and χ'' as a function of frequency (bottom) Cole-Cole plot of χ'' as a function of χ'. Figure reproduced from Encyclopedia Magnetica under CC-BY-4.0

It is also possible to represent χ'' as a function of χ', called a Cole-Cole plot. Assuming the linear model holds, its should take the form of a semi-circle as picture in Figure 2.3.3 (bottom). If it departs from this shape, it is the sign that there is not a single relaxation time, but a distribution of a certain width.

One issue the AC measurements pose in our case with a copper sample holder is the creation of eddy currents in the instrument. These in turn create magnetic flux where the sample is located which perturbs the measurement. Such effect is akin to a screening of the sample and can be modelled by applying the following transformation:

$$\begin{aligned} \chi'_{\text{true}} &= \chi'_{\text{exp}} \cos(\theta) + \chi''_{\text{exp}} \sin(\theta) + \chi'_0 \\ \chi''_{\text{true}} &= -\chi'_{\text{exp}} \sin(\theta) + \chi''_{\text{exp}} \cos(\theta) + \chi''_0 \end{aligned} \tag{2.3.7}$$

The angle θ and offsets χ'_0, χ''_0 depend on the frequency and must be evaluated at high temperature where the sample response is known.

2.3.4 SQUID magnetometer

The instruments we have used to measure magnetization and susceptibility are SQUID magnetometers. A DC SQUID (Superconducting QUantum Interference Device) is a ring built from two Josephson junctions, composed of superconductors separated by a thin isolating barrier. The current in a Josephson junction is a function of the superconducting phase difference $\Delta\phi$ between the two superconductors:

$$i(t) = i_c \sin(\Delta\varphi) \tag{2.3.8}$$

where i_c the junction's critical current. When considering a DC SQUID in the presence of a magnetic flux Φ, the flux quantification inside the ring imposes $2\pi\Phi/\Phi_0 + \Delta\varphi_1 - \Delta\varphi_2 = 0$, where $\Phi_0 = h/2e$ is the flux quantum, and $\Delta\varphi_i$ is the phase difference at the junction i. This induces a modulation of the critical current i_c, which then writes: $i_c = i_0|cos(\pi\Phi/\Phi_0)|$.

A simplified SQUID magnetometer is shown in Figure 2.3.4. The SQUID is inductively coupled to pickup coils in which the sample is moved. It is controlled by a feedback electronic system which turns it into a high-gain amplifier of magnetic flux. The SQUID is biased by a current to choose a working point where the voltage change as a function of flux is maximal. Then, when a magnetic sample is passed through the SQUID pickup coils at a constant speed, the variation of flux is translated as a voltage change. This is called the extraction technique.

In this thesis we have used custom SQUID magnetometers built by Carley Paulsen. To eliminate magnetic perturbations, the SQUID pickup coils are arranged in a first-order gradiometer and isolated with magnetic shields. One magnetometer is equipped with a superconducting coil which can apply fields up to 8 T. Another can only apply field up to 0.4 T, and allows measurement of χ_{AC} from 1 mHz to 1 Khz. The sample is connected to the mixing chamber of a dilution cane by a copper sample holder to ensure thermalization. The entire dilution cane is moved during the extraction and allows to measure magnetization and susceptibility down to

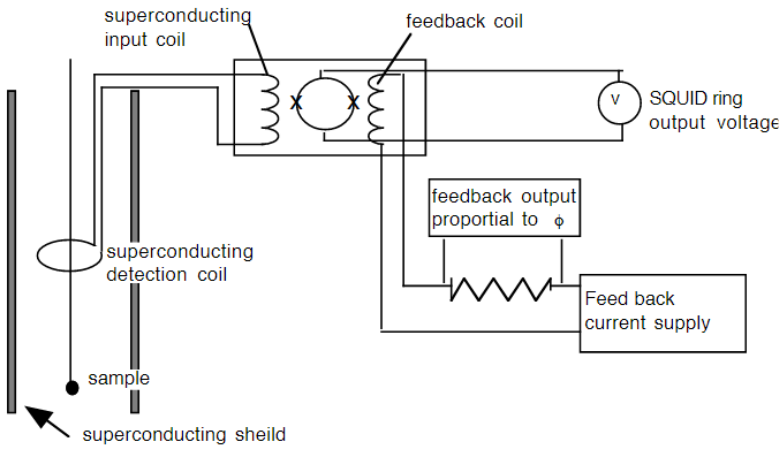

Figure 2.3.4: Simplified SQUID magnetometer.

70 mK. We have also used a commercial SQUID magnetometer built by Quantum Design called the MPMS3. It is instead a vibrating sample magnetometer (VSM), where the sample is vibrated at a known frequency and small amplitude inside the pickup coils. In this device the coils are arranged in a second order gradiometer. A SQUID working point is chosen in a similar way to get the maximal voltage change for a given amplitude of oscillation. The signal can be then be picked up by a lock-in amplifier. It can measure magnetization and susceptibility down to 1.8 K and an applied field of 7 T.

2.4 Neutron diffraction and scattering

2.4.1 Neutron properties and cross section

Together with protons, neutrons are particles which compose atomic nuclei. They are massive ($m_n \approx 1.67 \times 10^{-27}$ kg) and have a nuclear spin 1/2. With a gyromagnetic ratio of about -1.9 this results in them having a magnetic moment, but no electric charge as their name suggest. Therefore, they do not interact with nuclei through the Coulomb interaction but only through the strong interaction which has essentially a point-like potential. As a consequence the scattering can give very precise information on the structure of matter. On the contrary, their magnetic moment makes them interact with the magnetic field produced by unpaired electrons, as in the case of magnetic atoms. It is common to relate the energy of neutrons to quantities relevant in condensed matter physics. We can write the energy of a neutron as

$$E = \frac{h^2}{2m}\frac{1}{\lambda^2} = k_B T \tag{2.4.1}$$

Hence a so-called thermal neutron ($T \approx 300$ K) has a wavelength of about $1.8\,\text{Å}^{-1}$ and an energy of about 25 meV. These values are of the order of magnitude of the typical interatomic distances and magnetic excitations respectively. All these unique properties make neutrons a very suit-

able tool to probe condensed matter structures and their dynamics, especially in the case of magnetism.

The scattering amplitude of a neutron is proportional to the neutron flux and to the scattering cross-section. We consider an elastic scattering process with a scattering wave vector $\mathbf{Q}$ such that

$$\mathbf{Q} = \mathbf{k}_\mathrm{i} - \mathbf{k}_\mathrm{f},\ E_\mathrm{i} = E_\mathrm{f} \tag{2.4.2}$$

Let us consider a perfect lattice of atoms at positions $\{\mathbf{r}_j\}$ carrying dipolar moments $\{\mathbf{S}_j\}$. As we are interested in informations expressed in reciprocal space we define the following Fourier transforms:

$$N_\mathbf{Q} = \sum_j b_j e^{i\mathbf{Q}\cdot\mathbf{r}_j},\ \mathbf{M}_\mathbf{Q} = \sum_j f_{M,j}(\mathbf{Q})\mathbf{S}_j e^{i\mathbf{Q}\cdot\mathbf{r}_j} \tag{2.4.3}$$

The quantities b_j and $f_{M,j}$ account for the various interactions between neutrons and atomic nuclei or magnetic moments: they correspond to the scattering pattern produced by one single scattering object for the respective interaction, and are therefore the Fourier transform of the interaction potential. b_j is called the neutron scattering length of the nuclei at position j. It is a complex quantity, whose sign of the real part indicates if the neutron is attracted or repelled by the neutron, and whose imaginary part encodes the absorption. As mentioned above the nuclear scattering from the strong force is essentially point-like so b_j is a constant, which depends somewhat randomly on the nuclei. On the other hand, $f_{M,j}(\mathbf{Q})$ is called the magnetic form factor and has a strong $\mathbf{Q}$ dependance, due to the spatial extension of the electron cloud. The exact details of $f_{M,j}$ depend on the particular electron density of the unfilled orbital, but in a first approximation it has a somewhat bell shape with a half-width at half-maximum of $3-5\,\text{Å}^-1$. Plus, its intensity can be comparable to the nuclear scattering. This is the reason why neutron scattering is so useful for the study of magnetic structures: it produces magnetic Bragg peaks at low $\mathbf{Q}$ which appear distinctly from the nuclear peaks in diffraction experiments.

For scattering by unpolarized neutrons, the total cross-section is the sum of the nuclear and magnetic scattering, which can be shown to be well approximated by:

$$\frac{\mathrm{d}\sigma}{\mathrm{d}\Omega} \propto S_N(\mathbf{Q}) + S_M(\mathbf{Q}),\ \text{ with } S_N(\mathbf{Q}) = N^*_\mathbf{Q} N_\mathbf{Q} \text{ and } S_M(\mathbf{Q}) = \mathbf{M}^*_{\perp\mathbf{Q}}\mathbf{M}_{\perp\mathbf{Q}} \tag{2.4.4}$$

where $S_N(\mathbf{Q})$ and $S_M(\mathbf{Q})$ are called the nuclear and magnetic structure factor respectively. $\mathbf{M}_{\perp\mathbf{Q}}$ is the magnetic interaction vector, defined as

$$\mathbf{M}_{\perp\mathbf{Q}} = \hat{\mathbf{Q}} \times (\mathbf{M}_\mathbf{Q} \times \hat{\mathbf{Q}}) \tag{2.4.5}$$

where $\hat{\mathbf{Q}}$ is a unit vector parallel to $\mathbf{Q}$. It represents the fact that neutrons only see the component of the magnetization that is perpendicular to their scattering vector. This is a consequence of the dipole-dipole interaction between a neutron and the magnetization inside a sample, and can be understood visually by looking at the scattering by a dipolar field as shown in Figure 2.4.1.

Neutron scattering also allows for the study of excitations in condensed matter, where the

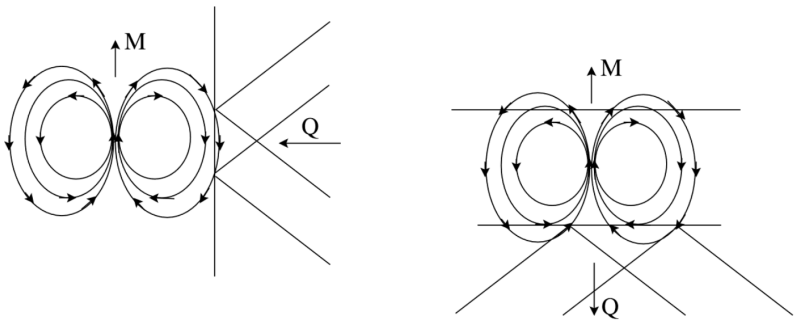

Figure 2.4.1: Neutron scattering off of a dipolar magnetic field. (right) $\mathbf{M} \perp \mathbf{Q}$ leads to constructive interference. (left) $\mathbf{M} \parallel \mathbf{Q}$ leads to destructive interference. Image reproduced from [Jülich, 2007]

quantities $\{\mathbf{r}_j, \mathbf{S}_j\}$ change in time in a coherent manner. This requires measuring the energy of scattered neutrons, whose difference with the incoming energy relates to the energy of excitations: $\hbar\omega = E_\mathrm{i} - E_\mathrm{f}$. The differential cross section now depends on the energy transfer and reads:

$$\frac{\mathrm{d}^2\sigma}{\mathrm{d}\Omega \mathrm{d}E} \propto f_N S_N(\mathbf{Q},\omega) + f_M(\mathbf{Q}) \sum_{\mu,\nu} S_M^{\mu,\nu}(\mathbf{Q},\omega) \tag{2.4.6}$$

where S_N and $S_M^{\mu,\nu}$ are the nuclear and magnetic dynamical correlations functions respectively:

$$\begin{aligned} S_N(\mathbf{Q},\omega) &= \frac{1}{2\pi\hbar}\int_{-\infty}^{+\infty} e^{-i\omega t}\langle N_\mathbf{Q}(0)^* N_\mathbf{Q}(t)\rangle \mathrm{d}t \\ S_M(\mathbf{Q},\omega) &= \frac{1}{2\pi\hbar}\int_{-\infty}^{+\infty} e^{-i\omega t}\langle M^\mu_{\perp\mathbf{Q}}(0)^* M^\nu_{\perp\mathbf{Q}}(t)\rangle \mathrm{d}t \end{aligned} \tag{2.4.7}$$

Nuclear excitations include phonons, which can appear as sharp branches going up in energy from nuclear Bragg peaks. Magnetic excitations can either be delocalized or localized on one site, which lead to very different signatures in the $(\mathbf{Q},\omega)$ space. For example, spin waves propagate through the lattice at different wavevectors and their inelastic scattering signal matches their dispersion relation. On the other hand, crystal field excitations are localized to one single site, and therefore only have the spatial dependance of the dipolar form factor in reciprocal space.

For this thesis we have used neutron instruments at two facilities: ILL and ISIS, both for elastic neutron diffraction and inelastic neutron scattering. We will briefly present the operating principles of each type of instrument below. Experimental data from diffractometer was analyzed with the FullProf software [Rodríguez-Carvajal, 1993]. It performs least-square optimization between the data and an input model, taking into account the specifics of each instrument. The model contains nuclear and magnetic phases with adjustable parameters, which must be constrained (in particular for the magnetic phases) knowing the allowed magnetic structures in each compound. Experimental data from inelastic scattering was analyzed with the Mantid software suite [Arnold et al., 2014].

2.4.2 Diffractometers: D1B and D20

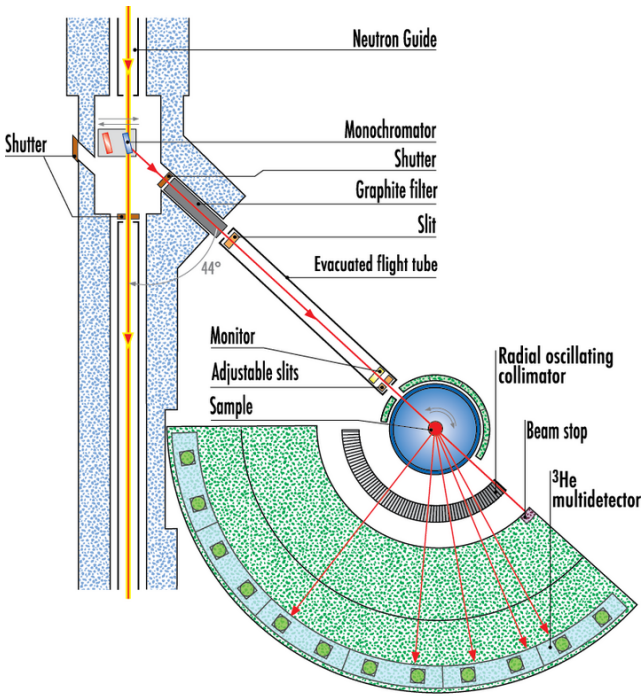

Figure 2.4.2: Schematic of the D20 diffractometer at ILL. Image reproduced from the ILL website

The Institut Laue-Langevin (ILL) in Grenoble is a high flux nuclear reactor dedicated to the study of the properties of matter with neutrons. At the time of writing, it is the brightest neutron source in the world with a continuous flux of 1.5×10^{15} neutrons $\cdot$ s^{-1} $\cdot$ cm^{-2}. Neutrons are produced through the controlled fission of ^{235}U which produces neutrons with an average energy of about 2 MeV. Such high energy neutrons are moderated (meaning slowed down), both to maintain the fission reaction and to provide a neutron beam to the scientific instruments. At ILL we have used the D1B and D20 diffractometers to determine magnetic structures at low temperature, with either a standard ^{4}He cryostat or dilution refrigerator. In particular D20 can accommodate a pressure setup, which we have used to measure the magnetic structure of $Ho_2Ir_2O_7$ under pressure.

Diffractometers operate with a fixed neutron wavelength, (2.52 Å for D1B). It is selected with a monochromator, which is usually a monocrystal (like graphite, Cu, Ge), orientated such as to diffract a single Bragg peak of known wavelength towards the sample. The neutron beam is then collimated on its way to the sample. The monitor, placed before the sample, then counts the total number of neutrons sent to the sample in order to properly normalize the data. The diffracted neutrons are detected by ^{3}He gas detectors, where the neutron is absorbed by the helium nucleus to create tritium and a proton. Being charged, the proton is then counted with a classical detector. The schematic of the D20 diffractometer is shown in Figure 2.4.2.

2.4.3 Time of flight spectrometers: WISH and LET

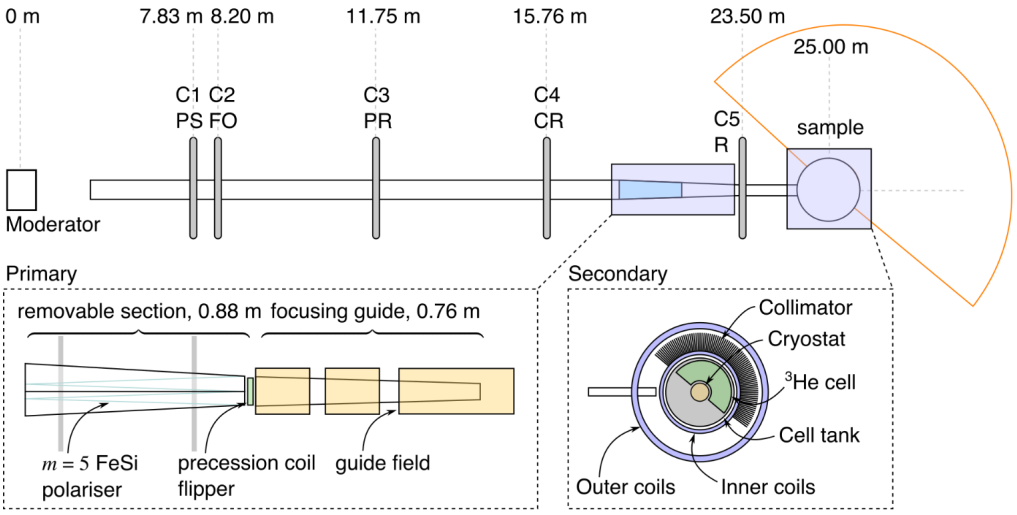

Figure 2.4.3: Schematic of the LET instrument viewed vertically. Five sets of disc choppers (C1-C5) select one or more neutron wavelength (Pulse Removal - PR, Contaminant Removal - CR), shape the pulse (Pulse Shaping - PS, Resolution - R), and eliminate frame overlap (Frame Overlap - FO). The magnified regions show the positions of the polariser and flipper and the analyser, respectively. Once polarised, the neutron beam can be flipped by a precession coil flipper. It is then transported to the sample by guide fields and a set of coils , before being analyzed by a wide-angle ^{3}He spin filter analyzer. Figure and caption adapted from [Nilsen et al., 2017]

Another technique to produce neutrons is the spallation process. It relies on a particle accelerator sending pulses of high energy protons (about 1 GeV) onto a heavy metal target (Pb, W, Hg...). As a result of the collision, neutron are produced, among other particles. This technique has the advantage of producing less radioactive waste but is inherently pulsed, sending packs of neutrons of various energies. The instruments at these facilities therefore operate in a different manner. The pulse of neutrons is first prepared by passing through a series of rotating disks with slices called choppers, whose speed determine the minimum and maximum energies. We have first used the WISH diffractometer at ISIS. It measures the time of flight, i.e. the energy, of neutrons arriving over a bank of detectors covering a certain angular range. Assuming the large majority of the neutrons detected were diffracted elastically, the time of flight is related to the wavelength via $t = (m_n l/h)\lambda$ where l is the length the neutron has traveled, which can then be converted back into reciprocal lattice units. Finally, we have performed an experiment on LET, which is a time of flight spectrometer used for the study of excitations in condensed matter. Compared to a diffractometer, its detectors are resolved in angle which allows for the simultaneous detection of a neutron's scattering wave vector and energy. A schematic of a time of flight spectrometer similar to LET is shown in Figure 2.4.3.

2.4.4 Neutron scattering from fragmented states

To finish this section, we want to apply the fragmentation decomposition to the formula for elastic neutron scattering. It is particularly useful as the longitudinal and transverse fragment, when transformed into reciprocal space, are orthogonal. Following the spin fragmentation, we can write $\mathbf{M}(\mathbf{Q}) = \mathbf{M_m}(\mathbf{Q}) + \mathbf{M_d}(\mathbf{Q})$, which obey the orthogonality condition $\mathbf{M_m}.\mathbf{M_d} = 0$ for all $\mathbf{Q}$. As a consequence, the magnetic structure factor also decomposes into two distinct parts

$$S_M(\mathbf{Q}) = S_{\mathbf{m}}(\mathbf{Q}) + S_{\mathbf{d}}(\mathbf{Q}) \tag{2.4.8}$$

so that the scattering intensity divides into components from the divergence-full and divergence-free the magnetic moments with no interference terms. Being associated with scattering from the ensemble of charges with total charge neutrality, the longitudinal fragment will contribute at antiferromagnetic peaks. Consequently, the scattering is purely from the transverse fragment inside the first Brillouin zone, except at the $\mathbf{Q} = 0$ point. The separation of these fragments has already been observed in magnetic charge crystal phases [Brooks-Bartlett et al., 2014; Lefrançois et al., 2017; Cathelin et al., 2020; Canals et al., 2016; Paddison et al., 2016].

Up to now we have not investigated the case of scattering by polarized neutrons. We will present a simplified version of the Blume-Maleyev equations for the present case of pyrochlore magnets. Using polarized neutrons, $S(\mathbf{Q})$ can be further resolved into "spin flip" (SF) and "non-spin flip" (NSF) components corresponding to scattering events in which the neutron spin direction is flipped or not [Fennell et al., 2009]. The SF scattering cross section lies in the plane perpendicular to the polarisation axis and projects out the component of $\mathbf{M}_\perp(\mathbf{Q})$ lying in this plane. The NSF component projects $\mathbf{M}_\perp(\mathbf{Q})$ onto the polarisation axis. This refinement leads to separate contributions to the structure factor, $S(\mathbf{Q})^{SF}$ and $S(\mathbf{Q})^{NSF}$ for scattering perpendicular and parallel to the polarisation axis, each of which can be decomposed into the two fragmentation components. Polarised neutron refinement is of particular interest for scattering from spin ice materials on the kagomé plateau. More specifically, choosing the neutron polarisation along the [111] field direction allows for the resolution of spin components parallel and perpendicular to the kagomé plane [Turrini et al., 2022].

In the following chapter we will demonstrate this property by computing the elastic scattering intensity of each fragment as well as of the total spin structure for different fragmented magnetic states. This property opens up the possibility of defining fragmentation order parameters by integrating the scattered intensity in specific regions of reciprocal space.

Chapter 3

Quantum fluctuations and phase transitions in fragmented spin ices

Contents

3.1 Motivations

The search for quantum materials is an important driving force in the field of solid state physics. However the concept of a quantum properties can have many practical or theoretical realizations to the point where its meaning becomes unclear. In the field of frustrated magnets, this can refer for example to the tunnelling of a single spins from one state to another. It can be enabled by crystal field excited states with an applied magnetic field [Tomasello et al., 2019] or because of small level separation [Gaulin et al., 2011]. On the opposite side of the quantum scale, it can relate to ground states where an extensive number of spins all intricated, like in quantum spin ice [Savary et al., 2017a] or in generalized quantum spin liquids [Wen, 2017]. We chose a median approach, where quantum effects are considered as collective fluctuations inside an otherwise classical ground-state manifold. In this section, we will investigate the effects of quantum fluctuations on examples of fragmented ground states and identify the relevant order parameter, with the goal of extending the fragmentation phase diagram from Chapter 1 towards low temperatures. We will first consider several cases on the kagomé lattice, then on the pyrochlore lattice, and conclude by detailing how the framework of fragmentation can help identify relevant order parameters.

3.2 Fragmented neutron scattering of quantum kagomé ice

3.2.1 Mapping to a dimer model and phase diagram

In this first section we investigate the example kagomé ice dressed with quantum fluctuations. We place ourselves in the KII kagomé ice phased discussed in Chapter 1 (Figure 1.1.9), which we recall is fragmented. The longitudinal fragment contains all the magnetic charge in the form of a partial all-in / all-out order. The transverse fragment is divergence free, with elements of field of different length. It maps onto a ($\mathbb{Z}_2$ sector of a) classical dimer model. Quantum fluctuations are added in the form of a $J_\pm$ transverse exchange, which yields an XXZ Hamiltonian on the kagomé lattice:

$$\mathcal{H} = \sum_{\langle i,j \rangle} J_{zz} \hat{S}_i^z \hat{S}_j^z - J_\pm (\hat{S}_i^+ \hat{S}_j^- + \hat{S}_i^- \hat{S}_j^+) = \mathcal{H}_0 + \mathcal{H}_1 \tag{3.2.1}$$

We follow the discussion of quantum perturbative methods in Chapter 1 and choose to describe its low energy behavior with the effective Schrödinger equation in Equation (1.3.9) [Moessner et al., 2001; Bergman et al., 2007b]. Here we can make use of the fragmentation formalism. We know that the effective Hamiltonian is projected onto the ground state manifold, where there are no charge excitations of typical energy J_{zz}. This means that the longitudinal field is effectively integrated out, and only the emergent transverse field contributes to the quantum dynamics of typical energy $J_\pm$. Since it maps to a dimer model, the effective Hamiltonian takes the form of a quantum dimer model on the hexagonal lattice. We are interested in the lowest non-zero order of the perturbation theory, meaning terms which involve the smallest number of dimer moves. Following Refs [Moessner et al., 2001; Bergman et al., 2007b], we use the

following quantum dimer Hamiltonian:

$$\mathcal{H}_{\text{eff}} = \mu \sum_{\hexagon} \left(|\hexagon\rangle\langle\hexagon| + |\hexagon\rangle\langle\hexagon| \right) - g \sum_{\hexagon} \left(|\hexagon\rangle\langle\hexagon| + |\hexagon\rangle\langle\hexagon| \right) \tag{3.2.2}$$

which is expressed as sum over all hexagons of the hexagonal lattice, also called hexagonal plaquettes. It is separated into two types of terms:

- **Diagonal terms** correspond to the classical energy of a particular dimer configuration. In our example, we give the potential energy μ to any plaquette with three regularly spaced dimers;
- **Non-diagonal terms** are the probability amplitudes of tunneling from one dimer configuration to another. Here we assign a "kinetic" energy cost g to the dimer move between the two possible types of plaquettes.

The phase diagram of such a quantum dimer model is a function of the μ/g ratio. It presents general characteristics which can be observed on a large number of lattices [Moessner et al., 2008]. For $g \ll \mu$ and $\mu > 0$, flippable plaquettes have a very high energy cost and therefore one gets a crystal of dimers with no flippable plaquettes. It is often called the columnar or staggered phase and maps onto a ferromagnetically ordered phase [Moessner et al., 2006]. Inversely for $\mu < 0$, flippable plaquettes are energetically favored. Thus the ground state is in the subspace of dimer coverings of the lattice which have the largest amount of such plaquettes [Moessner et al., 2001; Schlittler et al., 2017]. Finally, $\mu/g = 1$ is the Rokhsar-Kivelson point and is exactly solvable. Here the ground state is the superposition of all possible dimer coverings with equal weight and therefore the system does not display local order. This corresponds to a $U(1)$ quantum dimer liquid which can have a given extent in the phase diagram depending on the lattice.

The phase diagram of the quantum dimer model on the hexagonal lattice is shown in Figure 3.2.1. On this figure we show both the dimer grounds states at the top, and the equivalent states in the spin picture at the bottom, by mapping back from the dimers to a transverse fragment. But up to this point we don't know where the XXZ Hamiltonian we started with can be placed in this phase diagram. The exact computation of the effective parameters from degenerate perturbation theory is quite involved, but their scaling can be understood simply. Flipping a three-dimers plaquette requires applying the $J_\pm$ term three times, so the lowest-order non-diagonal term scales like $J_\pm^3/J_{zz}^2$. The diagonal term however requires coming back to the original configuration, applying the $J_\pm$ term another three times. It therefore scales like $J_\pm^6/J_{zz}^5$. In consequence, $\mu/g \sim (J_\pm/J_{zz})^3$ in the perturbative limit. This makes it possible to locate the so-called "spin-ice point" that corresponds to the position on the dimer model phase diagram of a particular classically frustrated system with small quantum fluctuations: $J_\pm \ll J_{zz}$ so $\mu/g \approx 0$.

The practical utility of quantum dimer models is that they are much easier to simulate numerically than a full spin system, and so their phenomenology and phase diagrams are better known. However, it is important to note that this remains an approximation that doesn't take into account the other interactions that might be relevant in spin ice materials. For example, a

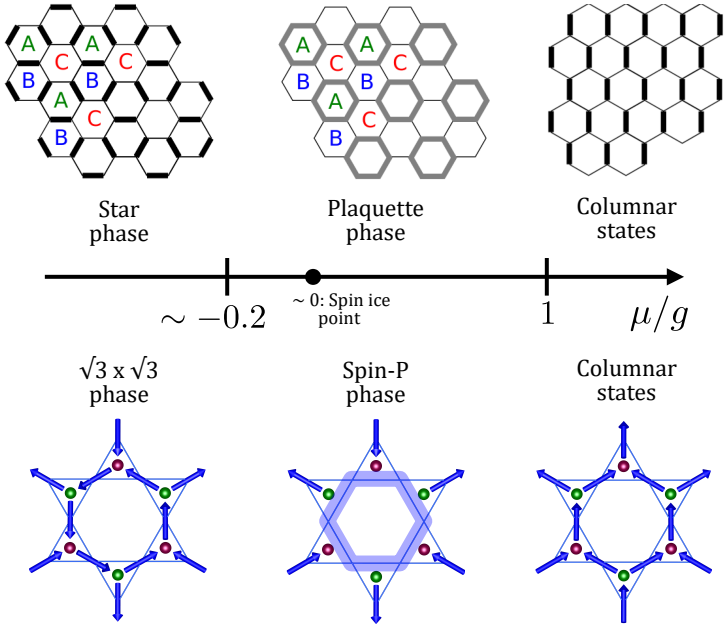

Figure 3.2.1: Phase diagram of the quantum dimer model in Equation (3.2.2) on the hexagonal lattice, with the ground states in the dimer picture (top) and spin picture (bottom), where the plaquettes in a quantum superposition state are shown with shaded links. The dimer pictures are adapted from [Schlittler et al., 2017].

possible evolution of the KII kagomé ice phase as the temperature is lowered [Möller et al., 2009; Chern et al., 2011], for example thanks to the long-range interactions, is the $\sqrt{3} \times \sqrt{3}$ phase. The effect of dipolar interactions can be understood simply when restricted to the ground state manifold: such interactions favors closing the magnetic flux lines, which results in an effective negative μ. However as we have explained, the $\mu/g \approx 0$ spin ice point is located deep in a different, quantum phase called the plaquette phase. Therefore, we will investigate the different diffraction signal produced by these two phases, in order to draft an experimental procedure to tell them apart.

3.2.2 The $\sqrt{3} \times \sqrt{3}$ and star phases

We start by considering the case of large negative μ/g. The ground state is called the $\sqrt{3} \times \sqrt{3}$ phase in the spin language, because it has magnetic unit cell 3 times the size of the lattice unit cell. Its emergent transverse fragment maps onto the star phase in the dimer language. Its structure is illustrated in Figure 3.2.2 top.

On the top row of the figure we show the fragmentation decomposition applied to the spin structure. The longitudinal part gives the charge order of alternate positive and negative charges, with a reduced unit cell of three sites. The transverse part maintains the 9-site unit cell, whose

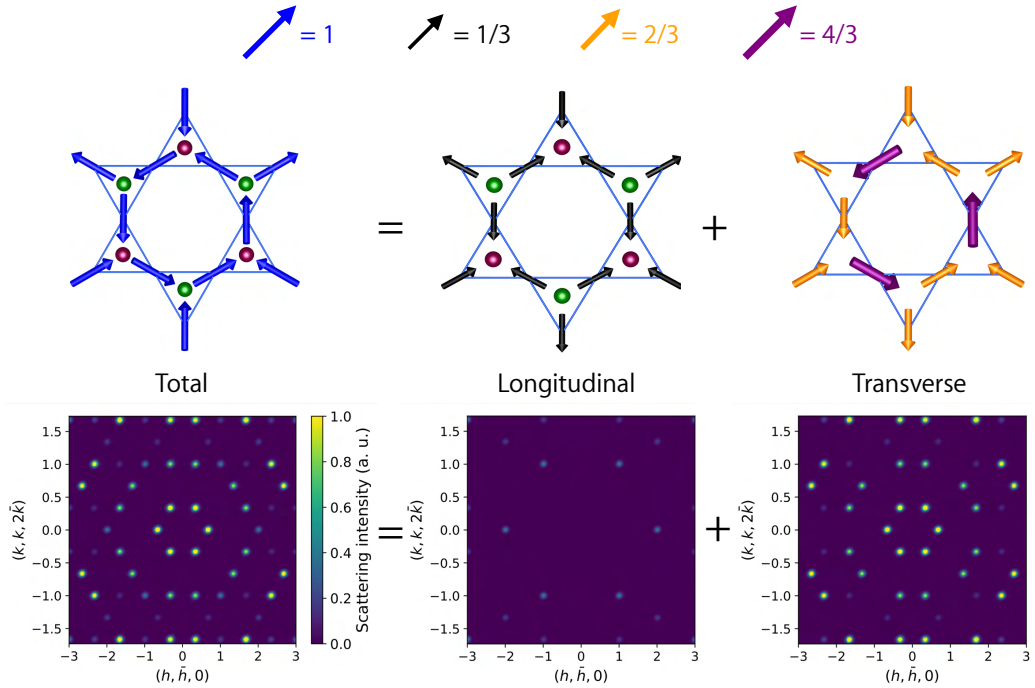

Figure 3.2.2: Top: Fragmentation of the $\sqrt{3}\times\sqrt{3}$ phase magnetic structure on a kagomé plane. Note that the unit cell extends over 9 sites. Colours illustrate the amplitude of each component, and green and purple spheres show the placement of positive and negative magnetic charges within the dumbbell model. Left panel, full spin configuration. Middle panel, longitudinal fragment $\mathbf{M_m}$ showing all-in / all-out ordering. Right panel, transverse fragment $\mathbf{M_d}$ showing emergent ordering of the star phase. Bottom: spin-flip neutron scattering intensities computed from the corresponding fragment above. The total scattering picture can also be computed by adding the separate intensities of the two fragments.

configuration maps onto the star phase emergent dimer solid which is build from three different hexagon configurations A, B and C shown in Figure 3.2.1. One out of the three form a six-fold symmetric star of dimers from which the phase takes its name [Moessner et al., 2001; Schlittler et al., 2017].

We now apply the same fragmentation decomposition to the structure factor; that is, we compute the magnetic part of Equation (2.4.4) separately for the longitudinal, transverse and total structures, and check that Equation (2.4.8) holds. I wrote a simple Python code to carry out the computation over a set of 16×16 magnetic unit cells in the scattering planes we are interested in, and smoothed numerically. The results are shown in the bottom row of Figure 3.2.2, in the scattering plane of the kagomé lattice in units appropriate for spin ice and the kagomé plateau: the in-plane axes $[k,k,2\bar{k}]$, $[h,\bar{h},0]$ lie perpendicular to the [111] field axis and are in units of $2\pi/a_c$. The six fold symmetry of the spins lying in the plane is represented in the figure by scaling the $[k,k,2\bar{k}]$ axis by a factor of $\frac{1}{\sqrt{3}}$.

The total scattering intensity for the $\sqrt{3}\times\sqrt{3}$ phase is indeed that of a fragmented double-q

structure. It is exactly the sum of the longitudinal and transverse parts, which have no communal Bragg peaks, as predicted in Equation (2.4.8). The total scattering is therefore made up of resolvable contributions from the charge ordering and the emergent field from the star phase. The charge ordering from the longitudinal component corresponds to antiferromagnetic, all-in / all-out order. This is a $\mathbf{Q} = 0$ order, with Bragg peaks at the centres of the kagomé lattice Brillouin zone starting at $h = 2, k = 0$ and symmetry related points, the scattering intensity being zero at the zone centres with smaller wave vector transfer. The star phase from the transverse component shows Bragg peaks at $h = \frac{2}{3}$, $k = 0$ and symmetry related points. These correspond to the basis vectors of the reciprocal space for the $\sqrt{3} \times \sqrt{3}$ unit cell with magnitude $q = \frac{2\pi}{a_c}\left(\frac{2\sqrt{3}}{3}\right)$. Peaks at larger q repeat in a distinctive, 6-fold symmetric pinwheel pattern which we can take to be characteristic of the star phase.

3.2.3 The spin-P and Plaquette phases

Let us now move to the case where quantum fluctuations are more prevalent. As discussed before, they promote a quantum superposition of closed loops of dimers. Therefore upon bringing μ/g gets closer to zero, the order parameter associated to the star phase is progressively reduced from saturation [Schlittler et al., 2017] up to a discontinuous transition. This intermediate phase, called the plaquette phase, has strong fluctuations but also long-range order. It is not a liquid phase, as dimer translational symmetry remains broken. But only one type of hexagon has a larger probability of finding a dimer around its perimeter contrary to the star phase, with the dimers are delocalized around the plaquette. This highlights the broken symmetry between the star and plaquette phases. Its equivalent in spin language is the resonating $\sqrt{3} \times \sqrt{3}$ phase, which we refer to as the spin-P phase. Two of the three types of hexagonal spin arrangement provide a framework for resonating loops of six spins around the third type of hexagon. This quantum resonance corresponds to a linear superposition of the two states per unit cell with spin rotations around the enclosed hexagon in opposite directions, leaving an effective magnetic state with reduced total moment, as shown in Figure 3.2.4 (top left).

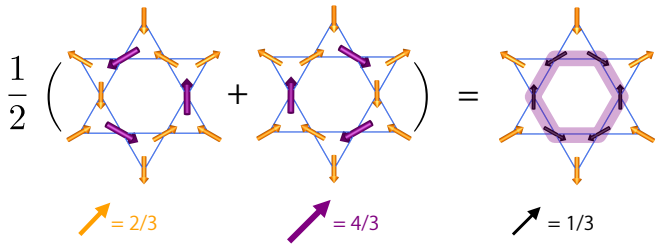

Figure 3.2.3: Approximation of the emergent transverse field in the spin-P phase, as an equal amplitude superposition of the two possible plaquette configurations.

In order to compute the scattering from the spin-P phase, one must first apply the fragmentation procedure to the effective reduced moments once the quantum spin resonances have been taken into account. From Figure 3.2.4 (top), one can see that the residual spin on each

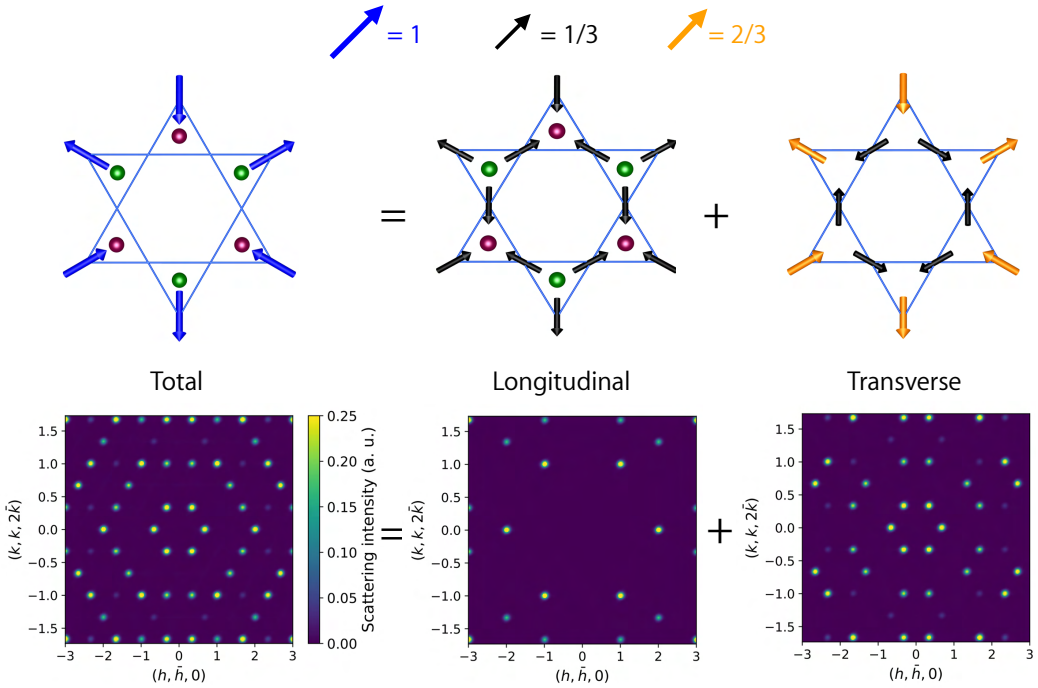

Figure 3.2.4: Top: Fragmentation of the spin-P phase magnetic structure on a kagomé plane. Note that the unit cell extends over 9 sites. Colours illustrate the amplitude of each component, and green and purple spheres show the placement of positive and negative magnetic charges within the dumbbell model. Left panel, full spin configuration. The quantum resonance on the hexagonal loop results in the effective absence of spins around the loop. Middle panel, longitudinal fragment $\mathbf{M_m}$ showing all-in / all-out ordering. Right panel, residual transverse fragment $\mathbf{M_d}$ corresponding to the residual emergent field of the dimer plaquette phase (see Figure 3.2.3). Bottom: spin-flip neutron scattering intensities computed from the corresponding fragment above. The total scattering picture can be computed by adding the separate intensities of the two fragments. Note that the absolute intensity scale is one quarter of that in Figure 3.2.2.

triangle can be written, using the previous notation; $\pm[-1,0,0]$, arranged such that the charge order is preserved. A vertex carrying a positive charge can thus be fragmented into a longitudinal and a transverse part

$$[-1,0,0] = [-\frac{1}{3},-\frac{1}{3},-\frac{1}{3}]_{\mathbf{m}} + [-\frac{2}{3},\frac{1}{3},\frac{1}{3}]_{\mathbf{d}} \tag{3.2.3}$$

This is equivalent to considering that the transverse fragment of the spin-P phase is the superposition of the two possible configuration of the transverse fragment of the $\sqrt{3}\times\sqrt{3}$ phase, as pictured in Figure 3.2.3.

This decomposition confirms that, on driving the $\sqrt{3}\times\sqrt{3}$ phase into the spin-P phase with quantum fluctuations, the charge ordering and hence the longitudinal fields are unchanged, while the amplitude of the transverse part is reduced by a factor of two. The quantum resonance is therefore limited to the transverse fragment as announced. Despite the resonance,

the emergent field retains a static residue which is precisely that of transverse spin fragment shown in Equation (3.2.3). The spin-P phase is therefore a superposition of the charge ordered phase, and the dimer plaquette phase represented by a single $\mathbb{Z}_2$ sector of its emergent field. In Figure 3.2.4 we show the neutron scattering data from the spin-P phase computed using the same PYTHON code, which we interpret using the fragmentation picture. We again expect the data to separate into independent longitudinal and transverse components and predict that the transverse scattering intensity will be reduced by a factor of four compared with scattering from the classical $\sqrt{3}\times\sqrt{3}$ phase. The intensity scale is reduced by a factor of four compared with Figure 3.2.2, highlighting the relative change in the two intensities.

3.2.4 The harmonic term of fragmentation

In this section, we will explain how the framework of fragmentation can be used to design experimental and numerical tests than can tell the difference between several fragmented phases. We start by highlighting an important and new extension to the standard formalism of fragmentation presented in Chapter 1 in Equation (1.1.12). It relies on the fact that for the Helmholtz decomposition in three dimensions to be unique, a third term is needed so that $\mathbf{M}$ writes:

$$\mathbf{M} = \mathbf{M_m} + \mathbf{M_d} + \mathbf{M_h} = \nabla\Psi + \nabla\times\mathbf{A} + \mathbf{h} \tag{3.2.4}$$

$\mathbf{h}$ is called the harmonic fragment due to the fact that it is both divergence and curl-free, and is mathematically determined by the boundary conditions imposed on the problem. In a more physical setting, it can be thought of as the overall magnetization of the system.

Consider again the case of spin ice under a magnetic field of modest strength along the [111] direction, as shown in Figure 3.2.5. We recall that the system enters the kagomé plateau region [Isakov et al., 2004]. In each tetrahedron the ice rules of two spins in and two out are satisfied but the apical spin is fixed to be out for an A tetrahedron and in for B. The three remaining spins, in the in-plane triangles forming kagome lattices perpendicular to the [111] direction, satisfy the kagomé ice rule with two spins in / one out on an A triangle and two out /one in on a B triangle [Moessner et al., 2003a]. In this phase, the monopole concentration (and therefore the longitudinal fragment) is zero. So the fragmentation decomposition concerns only the transverse and harmonic fragments. Using the previous notation and identifying the fourth element with the apical spin we find for a tetrahedron of type A:

$$\mathbf{M} = [-1,-1,1,1] = [0]_{\mathbf{m}} + [-\frac{2}{3},-\frac{2}{3},\frac{4}{3},0]_{\mathbf{d}} + [-\frac{1}{3},-\frac{1}{3},-\frac{1}{3},1]_{\mathbf{h}} \tag{3.2.5}$$

Here, the longitudinal fragment is zero, the transverse fragment is restricted to the three spins in the plane with two elements of amplitude $2/3$ and one of $4/3$ which together satisfy the zero divergence constraint. The harmonic term spreads out evenly over the three in-plane spins allowing the apical spin to be purely harmonic, with the sum over harmonic contributions en-

suring zero divergence. By projecting this decomposition on the kagomé planes, we find

$$\begin{aligned}\mathbf{M}^{2D} &= [-1,-1,1] \\ &= [-\frac{1}{3},-\frac{1}{3},-\frac{1}{3}]_{\mathbf{m}} + [-\frac{2}{3},-\frac{2}{3},\frac{4}{3}]_{\mathbf{d}}\end{aligned} \tag{3.2.6}$$

The in-plane projection of the harmonic term leaves a magnetic charge accumulation at the hexagonal lattice sites, corresponding to the longitudinal fragment of KII kagomé ice. The three-dimensional harmonic term therefore corresponds to a two dimensional longitudinal term. Similarly, the three-dimensional transverse fragment identifies readily to the two-dimensional one. Using the complete mathematical expression of fragmentation, we now understand why spin ice fragmentation on the kagomé plateau is intimately related to the fragmentation of two-dimensional spins in kagomé ice.

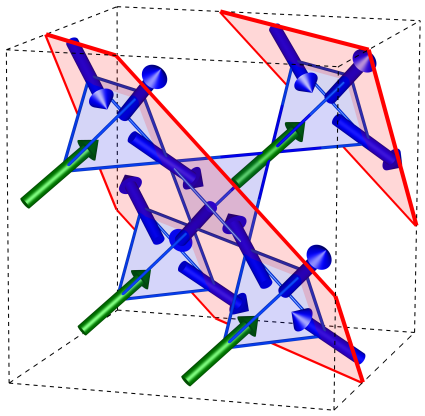

Figure 3.2.5: Pyrochlore spin ice in a [111] field, showing the distinction between planes of pinned apical spins on a triangular lattice (green) and kagomé planes satisfying the kagomé ice rules (red).

The only subtlety left is the spins on the kagomé planes of pyrochlore spin ice under field actually have a small canting out-of-plane, which our projection has conveniently made disappear. The experimental trick to reconcile the two and three-dimensional case is to use polarized neutrons, as explained in the end of Chapter 2. We can recover the purely in-plane scattering intensity of pyrochlore spin ice under a [111] field by looking at the spin-flip structure factor $S(\mathbf{Q})^{SF}$ with the neutron source polarised along the [111] direction[Turrini et al., 2022].

3.2.5 Comparison with quantum spin ice under a [111] field

We are now ready to review data from existing work in the context of our analysis using the fragmentation picture. In Figure 3.2.6 we show unpolarised neutron scattering data in the kagomé plane from Quantum Monte Carlo simulations. The data, for nearest neighbour quantum spin ice in a [111] field is reproduced from Ref. [Bojesen et al., 2017]. It is taken in the intermediate field region corresponding to the kagomé magnetization plateau. The right hand panel

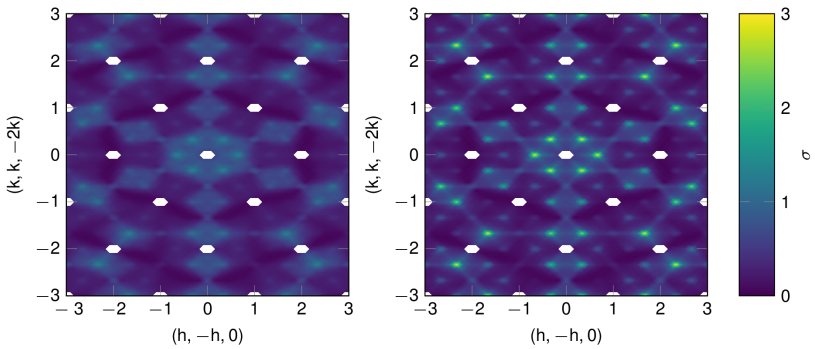

Figure 3.2.6: Unpolarized neutron scattering data in the kagomé plane from Quantum Monte Carlo simulations of quantum nearest neighbour spin ice in a [111] field. Left panel $\frac{T}{J} = \frac{1}{20}$, right panel $\frac{T}{J} = \frac{1}{320}$. Data reproduced with permission from [Bojesen et al., 2017].

shows data taken at $\frac{T}{J} = \frac{1}{20}$ where T is the temperature and J the coupling constant. It is consistent with Coulomb phase spin liquid behaviour, showing correlated diffuse scattering with pinch point features [Moessner et al., 2003a; Turrini et al., 2022]. Bragg peaks at the Brillouin zone centres corresponding to the ferromagnetic order generated by the harmonic fragment are masked and in an experiment would coincide with the structural Bragg peaks. On the right is shown data at much lower temperature, $\frac{T}{J} = \frac{1}{320}$ where the development of order is clearly observed. A different choice of scale along the vertical axis distorts the 6-fold symmetry of the scattering pattern but despite this one can observe features similar to those shown in Figures 3.2.2 and 3.2.4. In particular, sharpening peaks at the $h = \frac{2}{3}$, $k = 0$ and symmetry related points are clearly visible at the lowest temperature. A diffuse scattering background remains visible, presumably to remnant incoherent or thermal spin fluctuations about the ordered phase, which could be either the $\sqrt{3} \times \sqrt{3}$ or the spin-P phase.

We compare this figure to the diffraction patterns for the $\sqrt{3} \times \sqrt{3}$ and spin-P phases, shown in Figures 3.2.2 and 3.2.4. The peak structure is identical for the classical and quantum phases but the intensity difference can be used as a diagnostic to distinguish between them. For example, in the classical limit for the $\sqrt{3} \times \sqrt{3}$ phase, the intensity of inner ring of star phase peaks at $h = \frac{2}{3}$, $k = 0$ and symmetry related points, I_d^s is four times that of charge ordering peaks at $h = 2$, $k = 0$ and related points, I_m, while in the spin-P phase, the two sets of peaks, I_d^p and I_m have the same intensity. The difference could therefore be used as an order parameter separating the two phases.

$$Q = \sqrt{\frac{4I_m - I_d}{3I_m}} \tag{3.2.7}$$

Note that even within the $\sqrt{3} \times \sqrt{3}$ phase, quantum fluctuations in the form of flips of spins around either one of the two kinds of hexagon loops will also reduce the intensity of the transverse fragment peaks. This is already seen in direct simulations of the quantum dimer problem [Schlittler et al., 2017] and from these results we can anticipate that the peak intensities for the $\sqrt{3} \times \sqrt{3}$ phase will remain above those estimated for the spin-P phase.

In Figure 3.2.6 additional peaks can be seen compared with Figures 3.2.2 and 3.2.4. These are due to scattering from the out of plane spin components which as explained above appear as a consequence of simulating an unpolarised neutron source. Distinguishing between the two phases requires either an estimation of the absolute scattering intensity of the $h = \frac{2}{3}$, $k = 0$ Bragg peaks, or the inclusion of the $\mathbf{Q} = 0$ peaks, allowing a comparison of relative intensities. As these intensities differ by a factor of four, this should give a strong indicator as to which of the two possible ordered phases is emerging. Extended analysis of the $\mathbf{Q} = 0$ peaks, separating contributions from the apical spins and the triangular spins would give access to the charge ordering peaks of Figures 3.2.2 and 3.2.4 and to a comparison of the relative intensities of the longitudinal and transverse components of scattering from the spins in the kagomé plane.

3.3 Neutron scattering from the monopole crystal phase of spin ice

A similar application of the fragmentation framework can be made to the case of fragmented monopole crystal phase of spin ice in zero magnetic field [Brooks-Bartlett et al., 2014; Jaubert, 2015], which is the subject of this section. Our goal is again to understand the effect of quantum fluctuations on this fragmented phase. Here the transverse fragment maps onto a dimer model on the diamond lattice, so following the same approach as before we first focus on the associated quantum dimer phase diagram.

The quantum dimer Hamiltonian in Equation (3.2.2) on the diamond lattice has been studied both analytically [Moessner et al., 2001; Bergman et al., 2006] and numerically [Sikora et al., 2011]. The phase diagram is shown in Figure 3.3.1. For large and negative μ, the dimers crystallise into the so-called R-phase which maximises the number of hexagonal loops or plaquettes of dimers. The four-tetrahedra unit cell is shown at the top. Switching on the off-diagonal term through finite g, the classical R-order is again perturbed by quantum fluctuations until there is a phase transition to a quantum phase. In this case the ground state would incorporate quantum fluctuations around the classical R-order without inducing further changes to the translational symmetry (as was the case for the spin-P and plaquette phases). Moving the ratio μ/g away from zero, the dimer system is also predicted to enter a quantum phase but in a much smaller window, estimated numerically to be $0.75 < \mu/g < 1$ [Sikora et al., 2011]. Additionally this phase is a quantum dimer liquid rather than a resonating dimer solid. For $\mu/g > 1$, hexagonal plaquettes become unfavourable and the system passes discontinuously into a columnar phase[1] with dimers aligned along one of the [111] axes.

As discussed before, the emergent off-diagonal dimer moves are generated by a transverse spin coupling small compared with the nearest neighbour exchange. Therefore the spin ice point is again close to $\mu/g = 0$. As the inclusion of dipolar corrections to the classical monopole model sees the system order into the spin-R phase [Jaubert, 2015] this takes a putative quantum system, inclusive of dipolar interactions, even further from an emergent dimer liquid phase. We will therefore focus on the diffraction signal of the fully ordered phase illustrated in Figure 3.3.2

[1] referred to as isolated states in [Sikora et al., 2011]

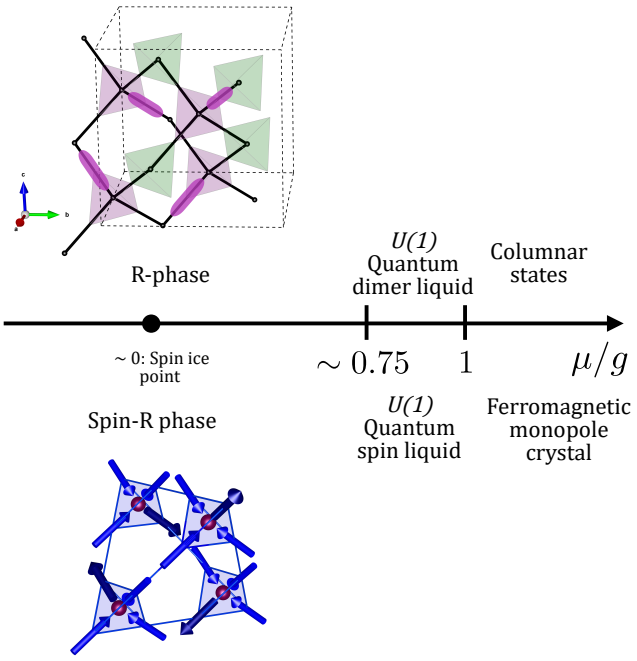

Figure 3.3.1: Top: R-phase dimer structure on the diamond lattice. The corresponding tetrahedra are pictured with a shade for comparison with the spin-R structure. This dimer representation is equivalent to the emergent field representation shown in the top right panel of Figure 3.3.2. Bottom: phase diagram [Sikora et al., 2011] for dimers on a diamond lattice as a function of the ratio μ/g from Equation (3.2.2). Also shown is the "spin ice" point corresponding to the location of the monopole crystal plus small transverse quantum spin fluctuations [Bergman et al., 2006], deep within the spin-R phase.

(top), which we refer to as the spin-R phase. The upper central and right panels show the longitudinal and transverse fragments respectively.

We recall that the transverse fragment of the monopole crystal maps onto one of the $\mathbb{Z}_2$ sectors of the emergent field for hard core dimers on a diamond lattice [Huse et al., 2003]. In this case, the element carrying transverse field $\pm\frac{3}{2}$, which is the minority spin of either the three in / one out or the three-out / one corresponds to the dimer position. The total spin structure can be represented as a classical superposition of the all-in / all-out order from the charges and the emergent field from the phase of ordered dimers, the R-phase. We apply the same computation procedure to compute the diffraction patterns relative to each fragment. The calculated unpolarised neutron scattering intensity from the spin-R phase is shown in the lower panels of Figure 3.3.2 for the $[hh0]$, $[00l]$ plane. They confirm that the scattering decomposes into a fragmented double-$\mathbf{Q}$ structure with different ordering wave vectors for the longitudinal and transverse parts. The longitudinal fragment shows the characteristic $\mathbf{Q} = 0$ ordering of the ionic crystal, while the transverse part orders with $\mathbf{Q} = (hhl)$ in units of the reciprocal cubic cell, $\frac{2\pi}{a}$ and with $h + l$ an odd number. The total intensity is again equal to the sum of the independent

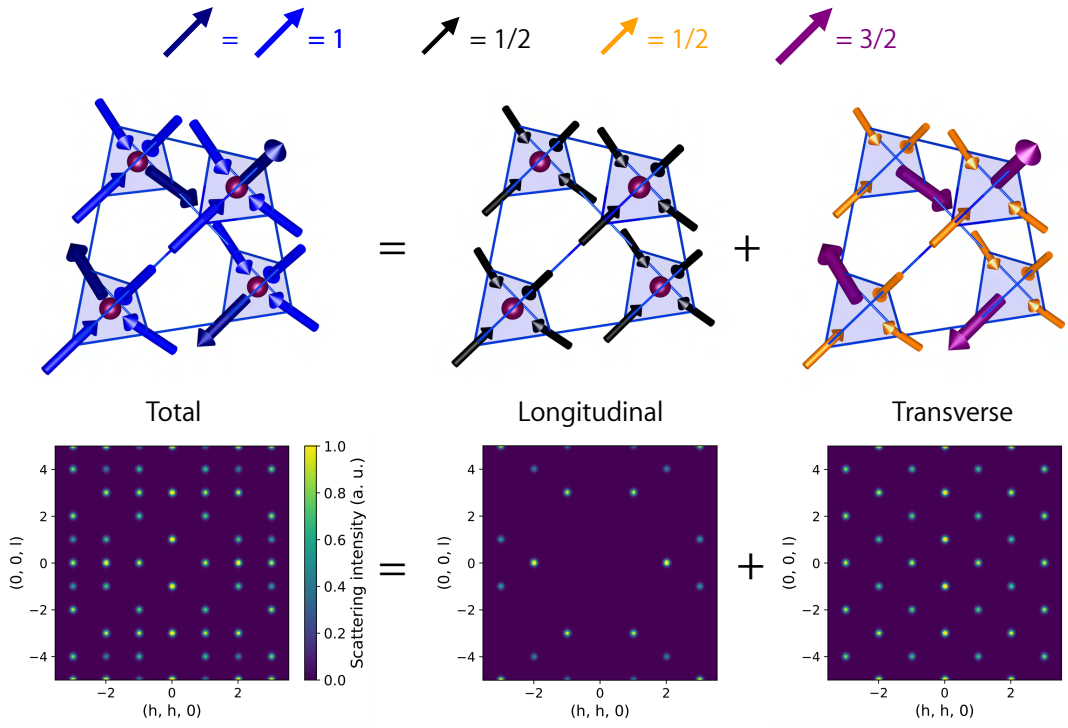

Figure 3.3.2: Top: fragmentation of the spin-R phase magnetic structure - a monopole crystal with ordered transverse fragment. Only half of the tetrahedra are pictured for clarity. Left panel, spin configuration. The minority spins are indicated by a darker shade of blue. Middle, longitudinal fragment $\vec{M}_{\mathbf{m}}$ showing all-in / all-out ordering. Right panel, transverse fragment $\vec{M}_{\mathbf{d}}$ corresponding to the emergent field for the ordered dimer phase (the R-phase, see Figure 3.3.1 (top)). The colours illustrate the amplitude of each spin component. Bottom: unpolarized neutron scattering intensities in the $[hh0]$, $[00l]$ plane computed from the corresponding fragment above. The total scattering picture can also be computed by adding the separate intensities of the two fragments.

fragments with no interference terms.

The previous discussion applies to a fully classical spin-R structure; let us now investigate the effect of larger quantum fluctuations, such that μ/g becomes significantly positive. As long as the system stays in the R-order region of the phase diagram, it would lead to reduction in the intensity of the [001] peaks coming from the transverse fragment while maintaining the classical intensity of the [220] peaks. With appropriate analysis, this intensity reduction could be developed as a diagnostic tool for the level of quantum fluctuations. If however one could move into the emergent quantum dimer liquid, the neutron scattering signature of this phase would strongly resemble that of quantum spin ice [Benton et al., 2012]. The emergent field for the quantum dimers maps to lattice quantum electrodynamics (LQED) [Sikora et al., 2011]. It has essentially the same structure and the same emergent photons which should show up in the inelastic neutron scattering spectrum, albeit at very low energy. Integrating over the photon bands to give static spin correlations, the pinch point structure of the classical system [Brooks-

Bartlett et al., 2014] would evolve. The dipolar correlations of the classical system would map to correlations in four dimensional space time with projection onto three dimensions leading to a suppression of the pinch point intensities at the Brillouin zone centres. These predictions could be tested using configurations from the quantum Monte Carlo simulations of Ref. [Sikora et al., 2011] and working backwards to construct the emergent transverse fragment of a monopole crystal. In this partial quantum liquid phase these modified spin correlations from the transverse fragment would coexist with the [220] peaks from the longitudinal fragment or charge order. The intensity of these Bragg peaks should remain unchanged within the regime of emergent quantum dimer fluctuations.

3.4 Perspectives on fragmentation

We conclude this chapter on a few perspectives to foster the use of the formalism of fragmentation, from both an experimental and theoretical point of view.

3.4.1 Fragmentation order parameters

First, we would like to extend the procedure used in the differentiation of the $\sqrt{3} \times \sqrt{3}$ and spin-P phases to obtain the order parameter in Equation (3.2.7). Our goal is to define three order parameters for each of the three fragments, which will be computed by integrating the scattered intensity on certain specific regions of the reciprocal space. A similar procedure was applied in Ref [Gray et al., 2021] for a two dimensional Coulomb fluid.

- **Longitudinal part**: When ordered, it can be represented by a scalar order parameter corresponding to the density of monopoles ρ. As described previously, it can be computed by integrating neutron diffraction data around antiferromagnetic Bragg peaks. When disordered, it will scatter mostly in the Brillouin zones around antiferromagnetic Bragg peaks;
- **Transverse and harmonic parts**: Separating these two contributions is trickier as their structure factor may have have interference terms. Nevertheless we can expect the harmonic fragment to be ordered as we have identified it to the overall magnetization. So a harmonic order parameter can be defined by integrating around $\mathbf{Q} = 0$ peaks at the center of Brillouin zones. The transverse order parameter can be defined on what remains of the reciprocal space. The case where both the harmonic and transverse fragment have a $\mathbf{Q} = 0$ order requires more careful thinking and is outside the scope of this work.

3.4.2 Fragmenting further: the poloidal-toroidal decomposition

Building upon the mathematical properties of the Helmholtz decomposition, the more mathematically inclined reader will notice that it can be expanded further with regard to the transverse

term. Any divergence-free vector field can be decomposed into toroidal and poloidal fields:

$$\begin{aligned} \nabla \times \mathbf{A} &= \mathbf{T} + \mathbf{P} \\ &= \nabla\phi \times \hat{r} + \nabla \times (\nabla\chi \times \hat{r}) \end{aligned} \tag{3.4.1}$$

where $\hat{r}$ is a radial unit vector, ϕ is the toroidal and χ the poloidal scalar potentials. Together with the longitudinal potential Ψ they make up the Debye potentials and allow the mapping of any vector field onto a set of three scaler fields, up to a harmonic contribution [Dubovik et al., 1990; Spaldin et al., 2008]. The fields from a single point dipole are purely poloidal while toroidal fields are characteristic of circular solenoids or toroids. The complete decomposition of the transverse magnetic fragment into poloidal and toroidal elements is beyond the scope of this discussion but pragmatically one can assume that the extensive loop network leading to pinch point scattering patterns is due largely to the poloidal component, while short loops contain a toroidal contribution. In modified spin ice models with induced attractive interactions between monopoles of like charge, low energy excitations include like charge clusters characterized by loops of spin flips, identified as toroidal loops [Udagawa et al., 2016; Mizoguchi et al., 2018]. Using the fragmentation picture it is straightforward to show that such clusters lead to isolated loops in the transverse fragment, which indeed correspond to a pure toroidal contributions. In a spin liquid phase dominated by such loops, the diffuse neutron scattering exhibits half-moons of high intensity straddling the Brillouin zone centre, rather than the pinch points of the Coulomb phase. This strongly suggests that magnetic moment fragmentation could be an essential tool for a complete description of such systems.

3.4.3 Beyond the perturbative limit: gauge Mean Field Theory

So far in this chapter we have used exclusively a perturbative approach to study the effect of quantum fluctuations. This has two mains drawbacks: it restricts the amplitude of the quantum fluctuations that we can consider, as well as the locations in the fragmentation phase diagram which can be used as a starting point for the degenerate perturbation theory. For example, the low temperature behavior of the spin-ice / monopole crystal boundary plane is not known in the case where spin ice and monopole crystal have the same ground state energy. In Ref [Lv et al., 2015], the authors studied numerically the closely related problem of the hardcore bosons on the pyrochlore lattice, with variable fillings. They found that the quantum fluctuations open an intermediate elusive "superfluid" phase between the two phases that would map to the spin ice and the monopole crystal in our case. To try to get a more analytical picture beyond perturbation theory, we resort to trying a new formalism: gauge Mean Field Theory (gMFT) developed by Savary *et. al.* in Refs. [Savary et al., 2012; Savary et al., 2013] and applied in Ref. [Bègue, 2012]. It has been used to sketch a phase diagram of a quantum Hamiltonian with parameters J_{zz}, $J_{\pm}$ and $J_{z\pm}$ shown in Figure 3.4.1.

The main advantage of gMFT is that it is a non perturbative approach, so it should in principle be correct for a wider range of parameters. In particular it would be of great interest to us to understand what happens at the phase boundary in the fragmentation phase diagram of Raban

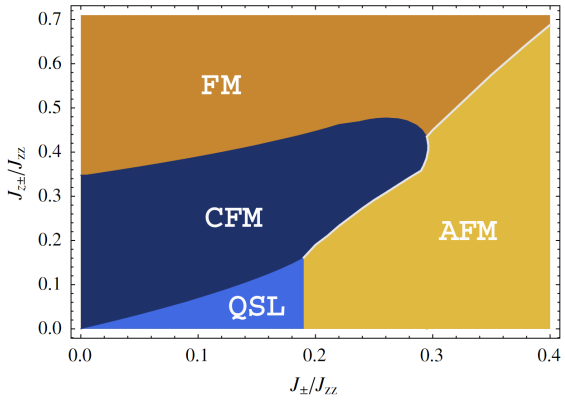

Figure 3.4.1: Phase diagram of quantum spin ice using gMFT, reproduced from [Savary et al., 2012]. AFM is an classical antiferromagnetic phase, FM a classical ferromagnet, QSL is the $U(1)$ quantum spin liquid of standard quantum spin ice and CFM is coulombic ferromagnet with quantum fluctuations but nonzero magnetization in the author's representation.

et. al. [Raban et al., 2019] (pictured in Figure 1.2.6). at low temperatures where quantum fluctuations might become prevalent. In this regime the degenerate perturbation theory cannot be applied as there are two distinct manifold of classical states very close in energy. In this section we will sketch a possible extension of the existing gMFT, and try to include the staggered chemical potential in the method.

The formalism builds upon the hardcore boson Hamiltonian in Equation (1.3.8). We define a new operator $\hat{Q}_{\mathbf{r}}$ which lives on the centers of the tetrahedra / sites of the diamond lattice :

$$Q_{\mathbf{r}} = \eta_{\mathbf{r}} \sum_{i \in \text{tet}\,\mathbf{r}} \hat{S}_i^z = \eta_{\mathbf{r}} \sum_{i \in \text{tet}\,\mathbf{r}} \left(\hat{a}_i^\dagger \hat{a}_i - \frac{1}{2} \right) \tag{3.4.2}$$

where $\eta_{\mathbf{r}} = \pm 1$ indexes the to diamond sublattices A, B. In the following we will drop the hat sign on quantum operators for clarity. In this language flipping a spin (or creating/annihilating a boson) corresponds to increasing the charge on one diamond site and decreasing on the adjacent site. However we recall here that the standard hardcore boson mapping is only unique up to a phase, which is usually discarded by setting it at 0 everywhere. gMFT makes use of this site-dependant phase $\theta_{\mathbf{r},i}$ to more accurately account for the quantum fluctuations and intrication between degrees of freedom. We introduce $\phi_{\mathbf{r}}$ the canonically conjugated variable to $Q_{\mathbf{r}}$: $[\phi_{\mathbf{r}}, Q_{\mathbf{r}}] = i$. Therefore one can show that $\Phi_{\mathbf{r}}^\dagger = e^{i\phi_{\mathbf{r}}}$ acts as a raising operator for $Q_{\mathbf{r}}$. Note that $\Phi_{\mathbf{r}}, \Phi_{\mathbf{r}}^\dagger$ are not creation and annihilation operators but rather discrete ladder translation operators, with $Q_{\mathbf{r}}$ akin to a distance from the origin; indeed Φ is unitary ($\Phi_{\mathbf{r}}^\dagger \Phi_{\mathbf{r}} = 1$). This is similar to the mapping made from a spin to a quantum rotor [Sachdev, 2011]. The excitations indexed by $Q_{\mathbf{r}}$ are called spinons and are of bosonic nature because there can be more than 1 per site, but $Q_{\mathbf{r}}$ is not a number operator because it can take a negative value. The constraint in the definition of Q keeps it between -2 and 2.

Keeping in mind that $Q_{\mathbf{r}}$ is like a position along a ladder, we have

$$\Phi_{\mathbf{r}} Q_{\mathbf{r}} \Phi_{\mathbf{r}}^{\dagger} = e^{-i\phi_{\mathbf{r}}} Q_{\mathbf{r}} e^{+i\phi_{\mathbf{r}}} = Q_{\mathbf{r}} - i[\phi_{\mathbf{r}}, Q_{\mathbf{r}}] \tag{3.4.3}$$

$$= Q_{\mathbf{r}} + 1 \tag{3.4.4}$$

Similarly $\Phi_{\mathbf{r}}^{\dagger} Q_{\mathbf{r}} \Phi_{\mathbf{r}} = Q_{\mathbf{r}} - 1$. We can now write the representation of a spin operator in terms of these new variables:

- For $\mathbf{r} \in A$:

$$\begin{aligned} S^{+}_{\mathbf{r},i} &= \Phi^{\dagger}_{\mathbf{r}} s^{+}_{\mathbf{r},\mathbf{r}+\mathbf{d}_i} \Phi_{\mathbf{r}+\mathbf{d}_i} \\ S^{-}_{\mathbf{r},i} &= \Phi_{\mathbf{r}} s^{-}_{\mathbf{r},\mathbf{r}+\mathbf{d}_i} \Phi^{\dagger}_{\mathbf{r}+\mathbf{d}_i} \end{aligned} \tag{3.4.5}$$

- Equivalently, for $\mathbf{r}' \in B$:

$$\begin{aligned} S^{+}_{\mathbf{r}',i} &= \Phi_{\mathbf{r}'} s^{+}_{\mathbf{r},\mathbf{r}-\mathbf{d}_i} \Phi^{\dagger}_{\mathbf{r}-\mathbf{d}_i} \\ S^{-}_{\mathbf{r}',i} &= \Phi^{\dagger}_{\mathbf{r}'} s^{-}_{\mathbf{r},\mathbf{r}-\mathbf{d}_i} \Phi_{\mathbf{r}'-\mathbf{d}_i} \end{aligned} \tag{3.4.6}$$

where $s^{+}_{\mathbf{r},\mathbf{r}+\eta_{\mathbf{r}}\mathbf{d}_i}$ is a local gauge field, $\mathbf{d}_i$ are the local pyrochlore axes. These relations means that flipping a spin creates a pair of spinons of opposite charge on neighboring tetrahedra, and changes the sign of the gauge field in between. We emphasize that $s^{+}_{\mathbf{r},\mathbf{r}+\mathbf{d}_i}$ is not the physical spin as it does not remain within the Hilbert space of a spin $\frac{1}{2}$. $\Phi_{\mathbf{r}}$ is similar to a matter field.

With this mapping the XXZ Hamiltonian becomes:

$$\mathscr{H}_{\text{gMFT}} = \frac{J_{zz}}{2} \sum_{\mathbf{r}} Q^2_{\mathbf{r}} - J_{\pm} \sum_{\mathbf{r}\in A} \sum_{i\neq j} s^{+}_{\mathbf{r},\mathbf{r}+\mathbf{d}_i} s^{-}_{\mathbf{r},\mathbf{r}+\mathbf{d}_j} \Phi^{\dagger}_{\mathbf{r}+\mathbf{d}_i} \Phi_{\mathbf{r}+\mathbf{d}_j} - J_{\pm} \sum_{\mathbf{r}\in B} \sum_{i\neq j} s^{+}_{\mathbf{r},\mathbf{r}-\mathbf{d}_i} s^{-}_{\mathbf{r},\mathbf{r}-\mathbf{d}_i} \Phi^{\dagger}_{\mathbf{r}-\mathbf{d}_i} \Phi_{\mathbf{r}-\mathbf{d}_j} + \text{cte} \tag{3.4.7}$$

which is the Hamiltonian of a $U(1)$ gauge theory. Indeed, upon local rotation of the spins by a angle $\theta_{\mathbf{r},i}$ around their z local, axes, the variables we have defined become

$$\begin{aligned} \Phi_{\mathbf{r}} &\to \Phi_{\mathbf{r}} e^{i\eta_{\mathbf{r}} \sum_{i\in \text{tet}\,\mathbf{r}} \theta_{\mathbf{r},i}} \\ s^{\pm}_{\mathbf{r},\mathbf{r}+\eta_{\mathbf{r}}\mathbf{d}_i} &\to s^{\pm}_{\mathbf{r},\mathbf{r}+\eta_{\mathbf{r}}\mathbf{d}_i} e^{\pm i\theta_{\mathbf{r},i}} \end{aligned} \tag{3.4.8}$$

so that $\mathscr{H}_{\text{gMFT}}$ remains invariant.

In this language the staggered chemical potential expression in straightforward:

$$\mathscr{H}_{\text{stagg}} = -2\Delta \sum_i S^z_i = -\Delta \sum_{\mathbf{r}} \eta_{\mathbf{r}} Q_{\mathbf{r}} \tag{3.4.9}$$

It favors charges +1 on sublattice A and -1 on sublattice B. The J_{zz} and $J_{\pm}$ terms do not commute, otherwise the problem would be trivial. However, the staggered chemical potential Hamilto-

nian commutes with both the J_{zz} and $J_{\pm}$ terms:

$$\left[\sum_i S_i^z, \sum_{<i,j>} S_i^z S_j^z\right] = 0 \tag{3.4.10}$$

$$\begin{aligned}\left[\sum_i S_i^z, \sum_{<i,j>} S_i^+ S_j^- + S_i^- S_j^+\right] &= \frac{1}{2}\sum_i \left[S_i^z, \sum_{j\neq i} S_i^+ S_j^- + S_i^- S_j^+\right] \\ &= \frac{1}{2}\sum_i \sum_{j\neq i} [S_i^z, S_i^+] S_j^- + [S_i^z, S_i^-] S_j^+ \\ &= \frac{1}{2}\sum_i \sum_{\mathrm{NN}\, j\neq i} S_i^+ S_j^- - S_i^- S_j^+ \\ &= 0 \text{ because it is antisymmetric under } i \leftrightarrow j \end{aligned} \tag{3.4.11}$$

This means that the eigenvectors of the staggered potential are all orthogonal to the eigenvectors of the J_{zz} and $J_{\pm}$ terms. The next step is to apply the mean field decoupling between the matter field Φ and the gauge field s to obtain two Hamiltonians $\mathscr{H}_\Phi$ and $\mathscr{H}_s$, coupled together by a small number of order parameters.

At this point we are faced with the task of applying the decoupling to the staggered chemical potential term. A first option is to use a clever variable change, which integrates the staggered chemical potential into a new monopole charge Q^*. Indeed we can merge the J_{zz} and staggered chemical potential term by "completing the square":

$$\frac{J_{zz}}{2}\sum_{\mathbf{r}} Q_{\mathbf{r}}^2 - \Delta \sum_{\mathbf{r}} \eta_{\mathbf{r}} Q_{\mathbf{r}} = \frac{J_{zz}}{2}\sum_{\mathbf{r}} \left(Q_{\mathbf{r}} - \frac{2\Delta}{J_{zz}}\eta_{\mathbf{r}}\right)^2 = \frac{J_{zz}}{2}\sum_{\mathbf{r}} Q_{\mathbf{r}}^{*2} \text{ since } \eta_{\mathbf{r}}^2 = 1 \tag{3.4.12}$$

This corresponds changing the origin of the ladder operators Φ depending on the tetrahedron, up on tetrahedron A and down on tetrahedron B for example.

Another option is to integrate the chemical potential into the decoupling on the $\mathscr{H}_\theta$ side. This could done by applying the commutation relation $2S_i^z = [S_i^+, S_i^-]$ in natural units and use the mapping in Equations (3.4.5) and (3.4.6):

$$\mathscr{H}_{\text{stagg}} = -2\Delta \sum_i S_i^z = -2\Delta \sum_{\mathbf{r}} \sum_{i\in \text{tet}\,\mathbf{r}} s^z_{\mathbf{r},\mathbf{r}+\mathbf{d}_i} \tag{3.4.13}$$

after the Φ terms simplify. Therefore the staggered chemical potential translates into a term which polarizes the gauge field away from 0 in average, without needing other interactions.

I have struggled to progress further in any of these approaches due to the technical difficulty of the formalism. However I am convinced that these ideas should enable the motivated reader to reuse a large part of the results in the original articles of Savary *et al.* [Savary et al., 2012; Savary et al., 2013] with minimal new computations, which would provide a better understanding of the fragmentation phase diagram with quantum fluctuations.

3.5 Conclusions

We have shown here that it is extremely useful to carry the fragmentation decomposition through to the analysis of neutron scattering results, as each component gives a separate contribution to the neutron scattering intensity. Previous texts have concentrated on situations in which an ordered monopole fragment coexists with the transverse fragment in the form of a correlated spin liquid on the kagome and pyrochlore lattices [Brooks-Bartlett et al., 2014; Lefrançois et al., 2017; Canals et al., 2016; Cathelin et al., 2020; Paddison et al., 2016]. Here we show that such systems with magnetic charge ordering, when driven into a fully ordered phase, either through quantum fluctuations or by long range interactions, form fragmented double-**Q** structures in which each fragment orders with a distinct ordering wave vector. Due to the separation in energy scales, quantum fluctuations are largely restricted to the transverse fragment. In consequence we argue that the intensity reduction of the transverse fragment compared to a known classical limit can be used as a diagnostic tool for the level of quantum fluctuations.

The analysis we propose relies on the existence of a gapped energy spectrum above the ground state. In this case, the proposed quantum resonances of spins, or effective dimes moves around hexagonal closed loops will lead to a quantifiable reduction in the observed neutron scattering intensity. For this to hold, both the temperature scale and the neutron energy resolution must be smaller than this gap. Bojesen and Onoda [Bojesen et al., 2017] have argued that their quantum Monte Carlo data for spin ice in a modest [111] field are consistent with the development of an emergent quantum dimer solid at low temperature. Our work provides a protocol for a detailed analysis allowing for the distinction between the quantum phase and its classical analogue. The energy scale associated with this quantum phase is extremely low; between 1/20 and 1/320 of the nearest neighbour coupling strength, so that quantitative measurement appears to be at the limit of numerical resolution. However, a clearer quantum limit is reached in dedicated quantum dimer simulations on a hexagonal lattice [Schlittler et al., 2017]. Our protocol could be tested in detail from such simulations by reconstructing a single $\mathbb{Z}_2$ sector of the emergent field from the dimers and constructing the corresponding neutron scattering plots.

Chapter 4

A new fragmented state in $Ho_2Ru_2O_7$

Contents

4.1 State of the art and motivations

In this chapter we focus on the ruthenate pyrochlore $Ho_2Ru_2O_7$. As Ru^{4+} ions are magnetic, this compound could provide a new way to explore the fragmentation phase diagram proposed in Ref [Raban et al., 2019]. It offers a opportunity to perturb the spin ice phase favored by Ho^{3+} ions in isolation, with the goal of finding exotic magnetic ground states. $Ho_2Ru_2O_7$ was first investigated in the early 2000s under the possibility that it could be a spin ice compound [Gardner et al., 2005; Wiebe et al., 2004]. The main goal of the authors was therefore to find if the material experienced a magnetic transition at low temperature, and the associated magnetic structure. They found that the Ru sublattice orders at 95 K in a ferromagnetic, ordered spin ice (Γ_9) structure. Upon further cooling, they detected a transition on the Ho sublattice at 1.5 K, therefore ruling out a standard spin ice phase in this material. Their specific heat measurements are shown in Figure 4.1.1 (right). Using neutron diffraction down to 100 mK, they were able to confirm that the associated Ho magnetic structure is also an ordered spin ice. Their neutron data refinement is shown in Figure 4.1.1 (left). However their work presented several shortcomings:

- the refinement of the Ru magnetic structure relied on the presence of a small peak around $Q = 1.25$ Å^{-1}, which could not clearly be seen in their data. We depicted it in orange on the picture;
- they found a Ho ordered moment of about 6 μ_B at base temperature but could not explain the missing intensity to account for the ≈ 10 μ_B expected for a Ho^{3+} doublet;

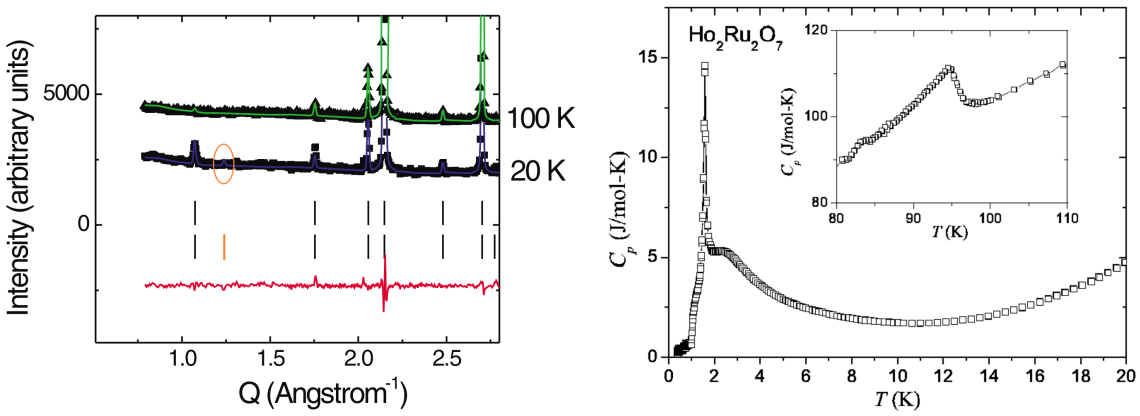

Figure 4.1.1: (Left) Neutron diffraction signal of $Ho_2Ru_2O_7$, reproduced from [Wiebe et al., 2004] (Right) Specific heat at high and low temperature, reproduced from [Gardner et al., 2005]

Our study of $Ho_2Ru_2O_7$ will try to address these issues, in order to correctly identify the magnetic ground state on both Ho and Ru sublattices, and identify the main ingredients which drive the ordering transition.

Let us first explain why the Ru^{4+} ions are magnetic, following the argument in Ref [Li et al., 2018]. They have a $4d^4$ electronic configuration. The crystal field they experience splits the $4d$ states into e_g and t_{2g} orbitals, pictured in Figure 4.1.2. However, due to the lowest principal

quantum number in Ru compared to Ir, the spin-orbit coupling could be of the same order of magnitude than the Hund coupling, i.e. the Coulomb repulsion between electrons in the same orbital. This leads to the two possible scenarii pictured on the right of Figure 4.1.2. If the Hund coupling is dominant, we get scenario (a), whereas if the spin-orbit interaction is dominant we get a quenched orbital degree of freedom as in scenario (b). This means that a perturbative picture with well separated energy scales may not be applicable to the Ru^{4+} ion in general; however in both cases we do get a $S_{Ru} = 1$ spin moment. Similarly to the Iridium $5d$ orbitals, we expect the Ruthenium $4d$ orbitals to have a significant spatial extension and effective hopping between neighboring sites, so that the Ru sublattice should have some conductive properties. Finally, the Ho^{3+} ion should exhibit the same properties as in other Ho-based pyrochlores, namely an almost entirely dipolar ground state doublet with the first crystal field excited states to be separated by an energy of about 200 K.

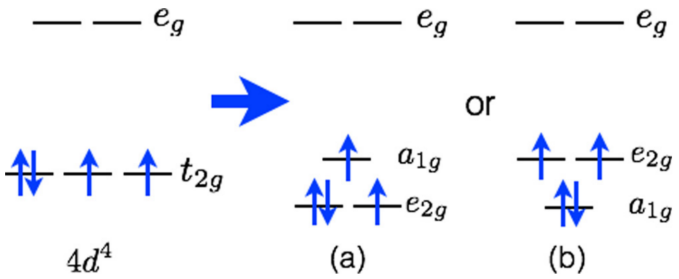

Figure 4.1.2: Orbital occupation of the Ru^{4+} ion, reproduced from [Li et al., 2018]

A powder sample of $Ho_2Ru_2O_7$ was synthesized by Elise Pachoud and Abdellali Hadj-Azzem at Institut Néel. They used a solid-state synthesis starting from a stœchiometric mix of the Holmium and Ruthenium powders, finely grounded in a mortar. Due to the tendency of Ruthenium to evaporate, they sealed the mixture in a glass ampoule filled with an inert gas. The sample was then compressed into several pellets. An impurity of 1.7% of Ho_2O_3 was measured by X-ray diffraction. Holmium does not absorb neutrons as much as Dysprosium and so is much more suited to neutron scattering experiments. However it has a large $I = 7/2$ nuclear spin which leads to a hyperfine contribution in the specific heat. We performed specific heat, neutron diffraction and magnetic measurements on this powder sample.

4.2 Sample characterization

4.2.1 High temperature: Ruthenium transition

First, we performed measurements above 2 K of the magnetization on the MPMS3 instrument, and of the specific heat on the PPMS instrument. We used the same sample of 24.3 mg.

On the top left of Figure 4.2.1 we show measurements of the specific heat. It has an anomaly at about 95 K which corresponds to the Ruthenium transition. On the top right we show H/M (which can be considered as the inverse susceptibility) as a function of temperature, in a zero

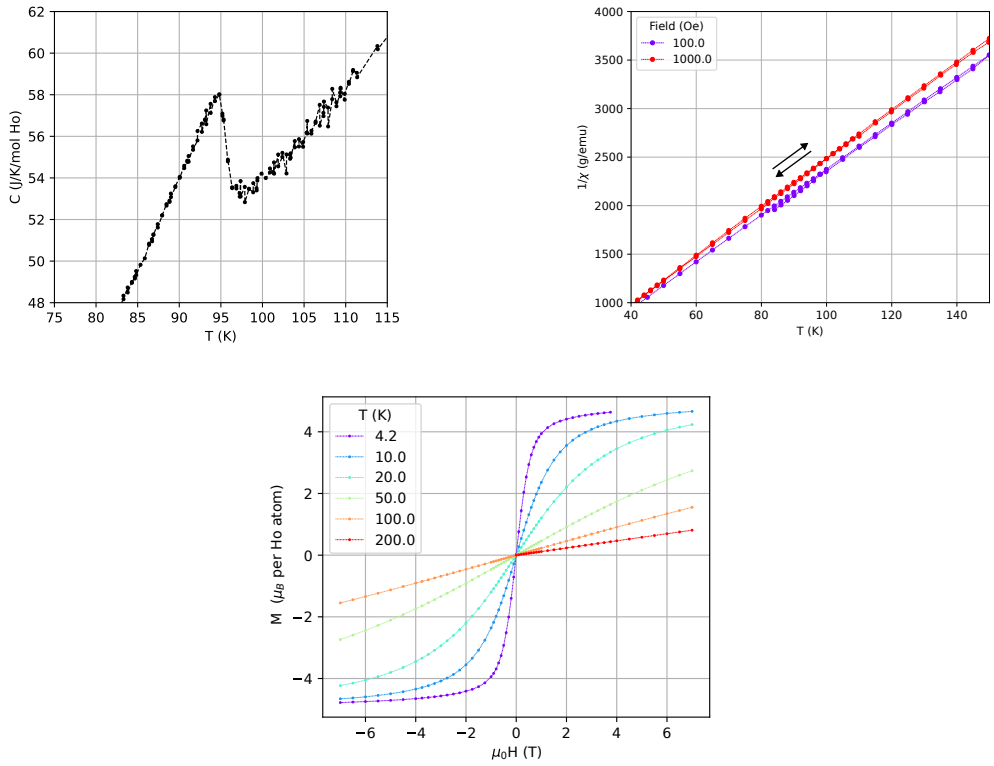

Figure 4.2.1: (top left) Specific heat anomaly at 95 K (top right) H/M measured for two fields with a ZFC-FC protocol (bottom) Magnetization as a function of field

field cooled and field cooled protocol for two applied fields of 100 and 1000 Oe. The data show no sign of any ZFC-FC effect around the ruthenium transition at 95 K, contrary to what was seen in Ref [Bansal et al., 2002]. The transition is not visible either in a dM/dT analysis. We can expect the Ru transition to be hard to see in magnetization measurements because of its small moment compared to Ho; however a ZFC-FC effect was seen in $Ho_2Ir_2O_7$ below the Ir transition. The fact that it could not be detected here could be the sign of a sample of good purity.

On the bottom row of Figure 4.2.1 we show measurements of the magnetization as a function of an applied field up to 7 T. At 4.2 K, we measure the saturation value to be about 4.75 μ_B per Ho atom. For a powder sample of a pyrochlore magnet with strong Ising anisotropy along the local $\langle 111 \rangle$ axes, the saturation magnetization per spin is one half of the projected magnetic moment $\mu_{/\!/}$ [Bramwell et al., 2000]. So our measurement is consistent with a Ho^{3+} ion with a strong Ising anisotropy and a magnetic moment $\mu_{/\!/} \approx 2 \times 4.75 = 9.5\ \mu_B$.

In order to confirm that the transition observed in specific heat is of magnetic nature, we performed neutron diffraction measurements on the D1B diffractometer at ILL. The data were collected by Claire Colin in an Easy Access experiment, on a ≈ 3 g powder sample with a wavelength of 2.52 Å. The sample was contained in a Vanadium sample holder and cooled with a ^{4}He cryostat. Claire Colin and Virginie Simonet provided the FullProf template files from which we refined the structure.

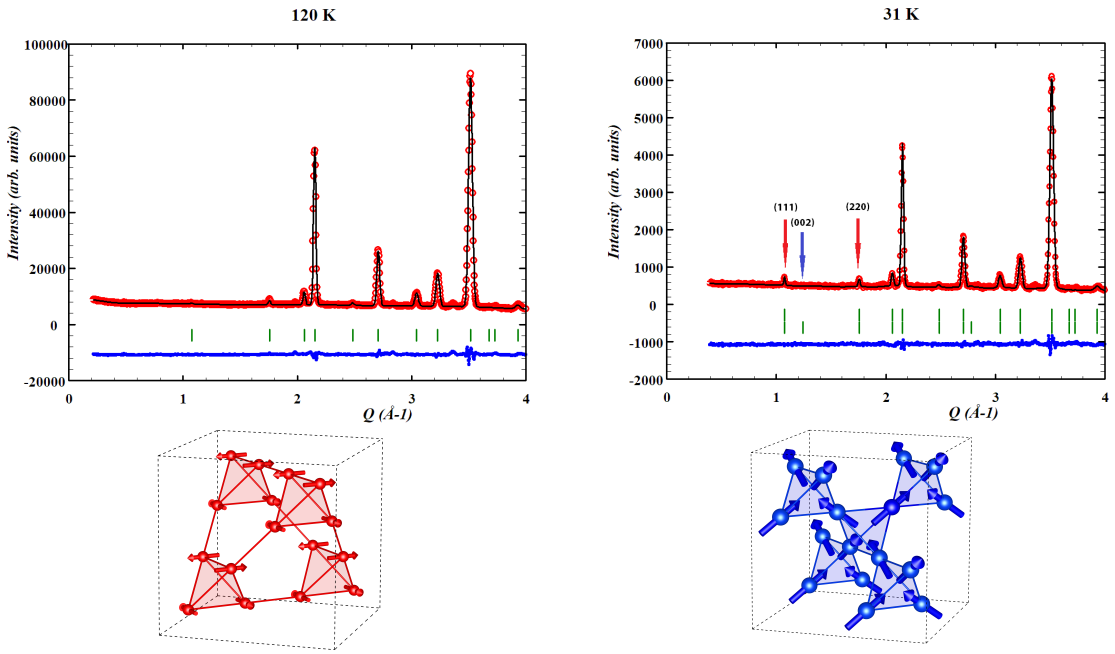

Figure 4.2.2: (top) Neutron data collected on D1B. (left) Refinement of the nuclear structure at 120 K (right) Refinement of the Ru magnetic structure at 31 K (bottom) Γ_5 antiferromagnetic structure in red and Γ_9 ferromagnetic structure in blue.

In Figure 4.2.2 (left) we show the neutron diffraction signal at 120 K (in red), which we refined successfully with a pyrochlore structure. At 10 K, the parameter for the position of the oxygen is $x = 0.335$ and the lattice constant $a = 10.11$ Å. At 95 K, small magnetic Bragg peaks appear at locations where there were no nuclear reflections: (111) and (220), which we show with red arrows on the picture. This is consistent with the transition seen in specific heat at this temperature and is therefore associated to the Ru magnetic ordering. However the magnetic structure we identify is in direct contradiction with the ferromagnetic ordered spin ice structure (Γ_9) proposed in [Wiebe et al., 2004]. This structure, where all tetrahedra are in the same two-in, two-out configuration, is associated to an additional magnetic Bragg peak at the (002) location (indicated by the blue arrow) which is not seen in our data. Instead, we find that the easy-plane, Γ_5 antiferromagnetic structure provides a better fit, as shown in Figure 4.2.2 (right). Below about 75 K, the amplitude of the Ru magnetic Bragg peaks does not increase. The ordered moment is of about 1.2 μ_B at 10 K. Going to the lowest temperature of about 1.6 K, we could see larger magnetic Bragg peaks develop which seemed to match the structure found in Ref. [Wiebe et al., 2004], but we could not study them in detail due to temperature regulation issues.

4.2.2 Low temperature: Holmium transition

To study in more details the transition that occurs at low temperature, we performed low temperature magnetization and susceptibility measurements from 100 mK to 4.2 K on the dilution

magnetometer on the same 24.3 mg sample. We also measured the specific heat of a 4.3 mg sample between 0.3 and 10 K on the PPMS instrument, using a ^{3}He insert. We note here that the 24.3 mg sample used for several measurements is a fragment of a pellet of about $2 \times 1.5 \times 1$ mm, shown in Figure 2.2.1 (left). We did not undertake an estimation of the demagnetization factor of this sample but due to its shape we believe its effect will be relatively small. In fact, the experiments on this sample were performed without maintaining a fixed orientation but their results remained consistent.

In Figure 4.2.3 (left) we show the specific heat data for several applied fields. It shows a sharp peak at a temperature $T_c \approx 1.55$ K, indicating a phase transition. Given the scale of the effective ferromagnetic exchange in Ho pyrochlore ($J_{\text{eff}} \approx 2$ K), it is natural to associate this transition to a magnetic ordering on the Ho sublattice. Confirming this hypothesis, an irreversibility is observed at low temperature between the ZFC and FC curves (see Figure 4.2.3 right), with a field-cooled behavior pointing towards a ferromagnetic transition. The amplitude of the ZFC-FC effect is large, indicating the presence of significant energy barriers below the transition.

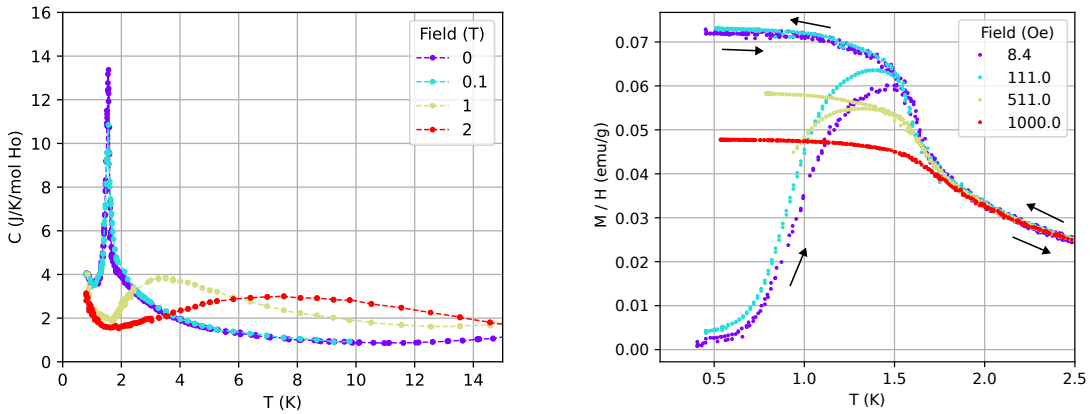

Figure 4.2.3: (left) Specific heat and (right) ZFC-FC effects at low temperature. The fields were corrected for the remanent field trapped in the superconducting coil. The 1000 Oe measurement was done field-cooled only, and a temperature regulation issue prevented the 511 Oe ZFC curve to be correctly measured.

We measured the AC susceptibility on the high field magnetometer. In Figure 4.2.4 we show χ' (left) and χ'' (right), corrected as best as possible from significant phase difference corrections above 10 Hz. The M/H curve matches well the low frequency χ' above the transition. Around the transition temperature, χ' exhibits a maximum, which moves slightly towards higher temperature when increasing the frequency. The width of the peak indicates that there is not a single time scale at the transition. Moreover, the space left between the 0.57 Hz curve and the ZFC curve points towards very slow dynamics below the transition. A frequency dependence is observed with a large signal in the out of phase χ'' susceptibility, but it is hard to exploit further due to the large phase corrections.

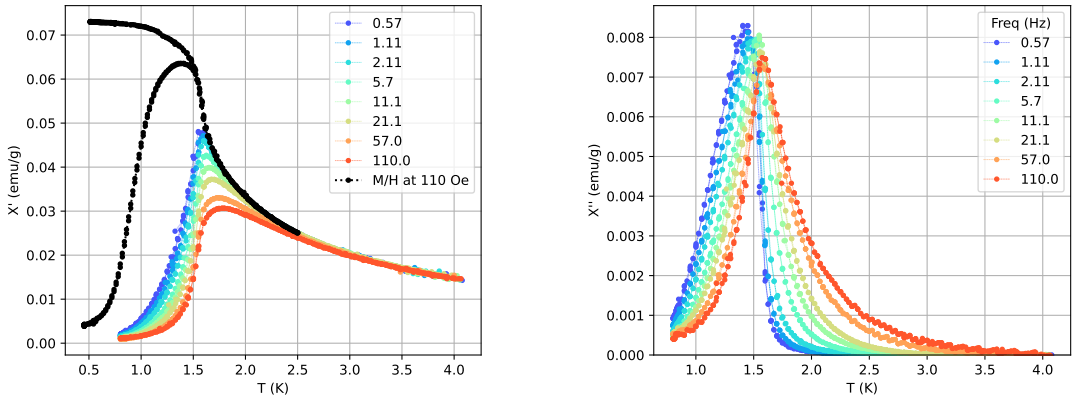

Figure 4.2.4: AC susceptibility vs temperature measured at several frequencies between 0.57 and 110 Hz. (Left) χ' (color crosses) together with M/H measured with $H = 111$ Oe (black crosses). (Right) χ''

The transition temperature, defined in magnetization measurements as the maximum of the slope of M/H, does not change significantly increasing the magnetic field. This is confirmed in the specific heat data, where the transition remains upon application of a 0.1 T external field. In Figure 4.2.5 (left) we show the magnetization as a function of field, measured on the high-field magnetometer. Below the Ho transition temperature, a hysteresis cycle opens, with a coercive field of about 0.13 T at 125 mK. At a higher field, the magnetization curves for a decreasing field at temperatures below the transition seem to exhibit an inflexion point. The shape is reminiscent of the case of spin ice in a [111] field, shown in Figure 1.1.8 and measured in Ref. [Petrenko et al., 2003]. It could be the sign of a field induced transition, but it is hard to conclude with our powder sample. Further measurements would be needed to better determine the field - temperature phase diagram.

In order to investigate the magnetic structure of $Ho_2Ru_2O_7$, we performed a new neutron diffraction experiment going down to a lower temperature. The data were collected on WISH, a time-of-flight (TOF) diffractometer at ISIS, by Pascal Manuel. We used the same sample as in the measurement on D1B, with a Copper sample holder and a Heliox ^{3}He sorption pump. The analysis of the data was performed with the FullProf software, starting from template command files provided by Virginie Simonet and Pascal Manuel.

At 95 K, we see small magnetic Bragg peaks that appear only at locations (111) and (220). This is consistent with the D1B measurement and confirms an antiferromagnetic Γ_5 structure for the Ruthenium. Going to temperatures below 5 K, a diffuse background at low-Q appears. In Figure 4.2.6 (left) we plot the signal collected from the lowest angle detector banks, allowing to see the signal down to $Q \approx 0.15$ Å^{-1}. The spikes at smaller Q are the signature of the limitations of the instrument at very long time of flights. The kink at $Q \approx 0.45$ Å^{-1} is due to the signal from the sample environment and cryostat and is independent of temperature. Nevertheless, we see a diffuse signal which arises from the 10 K reference in blue in the background. In particular it

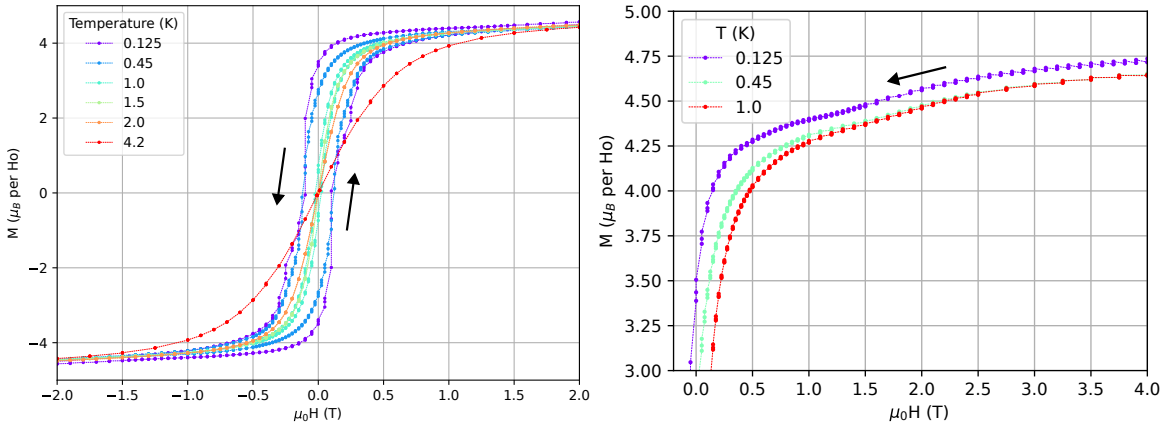

Figure 4.2.5: (Left) Symmetrized hysteresis cycles between 0.12 and 4.2 K and (Right) Zoom in M as a function of H obtained after saturation as the field is decreased, for temperatures below the transition

exhibits a bump between 0.5 and 1 Å^{-1}. This bump reaches a maximum in absolute value at 2 K (in red), and then gets suppressed progressively below the transition at 1.55 K as the spectral weight is transferred to the Holmium Bragg peaks. At the same time a rise in the diffuse signal below 0.3 Å^{-1} occurs and remains down to the base temperature. Because the Ru moments are fully ordered, the diffuse signal must originate from correlations developing between the Holmium spins. It could be a signature of dipolar correlations, as observed in other spin-ice type compounds [Fennell et al., 2009; Lefrançois et al., 2017]. In Figure 4.2.6 (right) we show

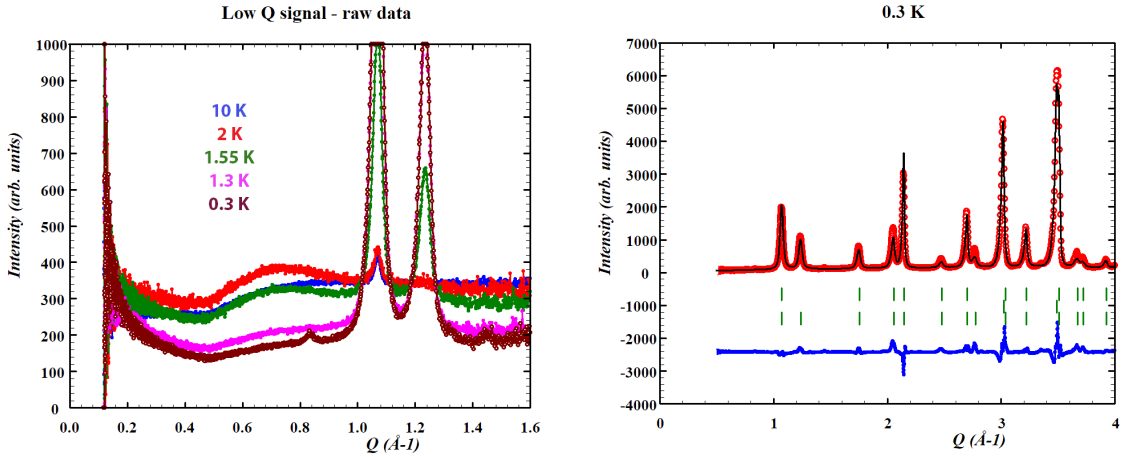

Figure 4.2.6: (Left) WISH diffraction data for several temperatures, showing the rise of Bragg peaks and of a diffuse signal. (right) Refinement of the data at 300 mK

the large magnetic Bragg peaks originating from the Ho magnetic structure at the base temperature (300 mK). They can indeed be refined by an ordered spin-ice (Γ_9) structure, as proposed in [Gardner et al., 2005; Wiebe et al., 2004]. We have used a joint refinement of the Ho and Ru structure in order to account for potential interference effect. Leaving the Ru moment as a vari-

able did not improve significantly the quality of the fit, so we left it fixed at its 10 K value. We find an incomplete ordered moment for Ho at low temperature, of about 6.5 μ_B at 300 mK, as observed by Wiebe *et. al.*. Finally, small peaks appear below 1.2 K at 0.85 and 1.45 Å^{-1}. They are most likely the sign of the magnetic transition of an impurity.

4.3 Towards a fragmented ground state

In this section we propose a new ground state for $Ho_2Ru_2O_7$, which is more consistent with all the experimental data.

4.3.1 Magnetic specific heat and entropy

In the study of Ising systems (or in general systems which are formed of copies of a N-level fundamental object), the measure of the entropy is a powerful tool to gain information on the nature of the ground state. At temperature high compared to the relevant energy scales, the entropy per site is $k_B \ln N$ because all levels are equally occupied. Then, a measure of the specific heat can give access to the entropy difference released over the temperature range:

$$\Delta S = S_{\text{High T}} - S_{\text{Low T}} = \int \frac{C}{T} \mathrm{d}T \tag{4.3.1}$$

The low temperature entropy, if not 0, is called the residual entropy and characterizes the ground state degeneracy. However, the application of this procedure is more complex in a real world example, because all materials have other degrees of freedom in addition to the one of interest.

In the case of $Ho_2Ru_2O_7$ we focus our attention on the entropy associated to the magnetic degrees of freedom. In the temperature range < 25 K, one must subtract the contributions from the nucleus (which accounts for the increase in C below 1 K) and the lattice (which arises above 10 K). In Ref. [Gardner et al., 2005] the authors do not give the details of this procedure but reported a deficit of entropy at low temperature, comparable to that of the kagome plateau of spin ice under a moderate [111] field: $S_{\text{residual}} \approx R \ln 1.17$ J/K/mol.

We first focus on the hyperfine contribution coming from the Ho nucleus. Indeed, the only stable isotope ^{165}Ho has an $I = 7/2$ nuclear spin and therefore its levels can be split by the interaction with the electronic spin. Fortunately, due to the interaction being very small, the energy scale is of the order of few hundred mK and does not interfere with the electronic spin frustrated physics. It does however contribute to a large increase in specific heat below 2 K and must be accounted for to isolate the magnetic contribution. We model the nucleus as a $2I + 1 = 8$ level system obeying the following Hamiltonian:

$$\mathscr{H}_N = A_{/\!/} I_z + P\left(I_z^2 - \frac{1}{3} I(I+1)\right) \tag{4.3.2}$$

$A_{/\!/}$ is the strength of the hyperfine interaction, which splits the nuclear levels evenly, and P is the quadrupole interaction, driven by the average quadrupole electronic moment, which modifies the splitting between high and low I_z. The computation of the associated specific heat for one

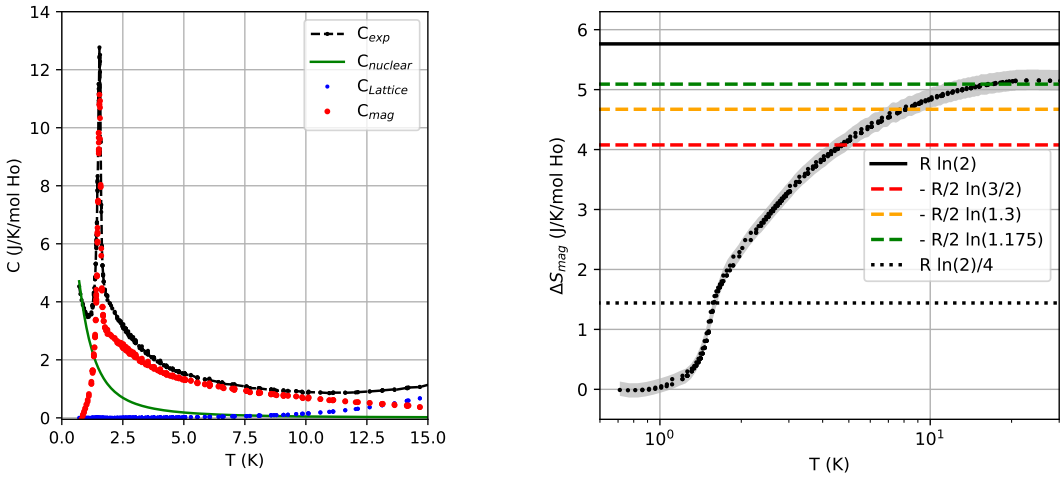

Figure 4.3.1: (left) Measured specific heat in black, nuclear contribution in green, lattice contribution in blue, and subtraction in red (Right) Estimation of the magnetic entropy, with the expected values for different spin ice phases: standard spin ice in red, monopole crystal in orange, kagome plateau of spin ice in green.

nucleus is straightforward:

$$C_N = \frac{\partial \langle E \rangle}{\partial T} = \frac{\partial}{\partial T}\left(k_B T^2 \frac{\partial \ln Z}{\partial T}\right) = \frac{\sum_{i=-I}^{I}\sum_{j=-I}^{I}(E_i^2 - E_i E_j)\exp\left(\frac{-E_i-E_j}{k_B T}\right)}{(k_B T)^2 \sum_{i=-I}^{I}\sum_{j=-I}^{I}\exp\left(\frac{-E_i-E_j}{k_B T}\right)} \tag{4.3.3}$$

When applied to only 2 levels, it yields the well-known Schottky anomaly. This expression could in theory be fitted to the data, but we could not accurately collect enough data points at low temperature to perform this. Below approximately 700 mK, the increase in specific heat and the decrease in grease conductivity cause the sample to become decoupled from the sample holder. This effect is amplified by the fact that we have a powder sample. We instead chose to manually adjust the rise in specific heat measured below 1 K, comparing our estimates of $A_{/\!/}$ and P with published values measured in other Ho^{3+} systems [Lounasmaa, 1962; Bramwell et al., 2001; Mennenga et al., 1984]: $A_{/\!/} \in [0.3, 0.4]$, $P \in [0.002, 0.009]$. We find values of $A_{/\!/}/k_B = 0.33\ K$, $P/k_B = 0.009\ K$ work best for our data. This best adjustment is represented in green in Figure 4.3.1.

Secondly, we turn our attention to the lattice degrees of freedom, responsible for the increase in specific heat above 10 K. Fitting the data to a Debye model would be made difficult by the presence of the ruthenium magnetic transition at $T_N = 95$ K. So as a better approximation we chose to measure the specific heat of the non magnetic analogue $Lu_2Ru_2O_7$: it has the same pyrochlore lattice and therefore a similar phononic structure. However the $Lu_2Ru_2O_7$ measurement needs to be rescaled to account for the different molar mass. The lattice specific heat is a function of the ratio T/Θ_D, where Θ_D is the Debye temperature which varies like the inverse

square root of the molar mass. Thus

$$C_{L,\mathrm{HRO}} = C_{L,\mathrm{LRO}}\left(T \times \frac{\Theta_{D,\mathrm{LRO}}}{\Theta_{D,\mathrm{HRO}}}\right) = C_{L,\mathrm{LRO}}\left(T \times \sqrt{\frac{M_{\mathrm{HRO}}}{M_{\mathrm{LRO}}}}\right) \tag{4.3.4}$$

With this conversion we estimate the lattice contribution as the blue points in Figure 4.3.1 (left).

The subtraction of both contributions leaves our estimation of the magnetic specific heat in red. In Figure 4.3.1 (right) we show the resulting estimation of the entropy difference associated to the Holmium magnetic transition. The shaded area corresponds to the uncertainty related to the process of finding a suitable hyperfine contribution and is estimated by using the two extreme values of $A_{/\!/}$ and P that seem to adjust equally well to the low-temperature data. The main result is that the entropy difference does not reach $k_B \ln 2$ at high temperature. The residual entropy does not match with the Pauling estimate for standard spin ice (in red) nor the fragmented monopole crystal (in orange), but it does match with the one for spin ice under a moderate [111] field, computed from the 2D kagome ice entropy. Additionally, below the transition temperature a quarter of the $R \ln 2$ entropy is released, suggesting that below this temperature one spin per tetrahedron orders in a long-range fashion. This gives a first indication that the ground state structure is not the conventional [100] ordered spin ice previously proposed.

4.3.2 Neutron diffraction of spin ice under a [111] field

The residual entropy discussed above, together with the incomplete moment in an Ising system assuming a Γ_9 structure are strong arguments in favor of a fragmented ground state where an ordered and a disordered fragment coexist. But what type of fragmented structure would give the same Bragg peaks as the ordered spin ice structure we see in $Ho_2Ru_2O_7$? From the diffraction patterns in the ordered phase, we know that there is no all-in / all-out ordered moment corresponding to a longitudinal fragmentation term. Therefore the fragmentation would occur between the transverse (fluctuating) and harmonic (ordered) terms. We have defined this case in Chapter 3, as the fragmentation decomposition of a classical spin ice under a moderate [111] field. One spin per tetrahedron (called apical spin) is pinned towards the field and the 3 others obey the kagome ice rule. We restate the decomposition into a harmonic and transverse fragments below, with the first spin the apical spin:

$$[1,1,-1,-1] = \left[0,\frac{4}{3},-\frac{2}{3},-\frac{2}{3}\right]_{\mathbf{d}} + \left[1,-\frac{1}{3},-\frac{1}{3},-\frac{1}{3}\right]_{\mathbf{h}} \tag{4.3.5}$$

The crucial point is that the harmonic fragment also belongs to the same Γ_9 representation. In fact, it can be constructed by considering the superposition of 3 ordered spin ice configurations in 3 cubic directions, which yields in average on one tetrahedron:

$$\frac{1}{3}\big([1,1,-1,-1]+[1,-1,-1,1]+[1,-1,1,-1]\big) = \left[1,-\frac{1}{3},-\frac{1}{3},-\frac{1}{3}\right] \tag{4.3.6}$$

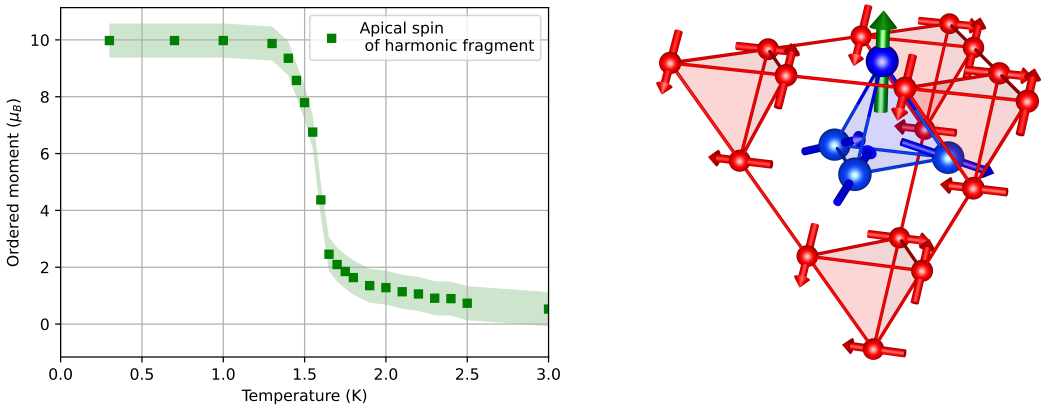

Figure 4.3.2: (left) Magnetic moment of the Ho apical spin as a function of temperature. (right) Fragmented structure in $Ho_2Ru_2O_7$, with the Ru ions in red and the Ho ions in blue. The Ho apical spin is plotted in green and is fixed. The three other Ho spins satisfy the kagome ice rules.

In consequence, the magnetic Bragg peaks associated to such a fragmented state are identical to the one for a fully ordered spin ice, as it is a type of powder average, with two notable exceptions:

- the intensity of the peaks will be reduced due to the partial ordered moment on certain sites;
- the transverse fragment will also diffract neutrons, and should give a diffuse signal representative of the correlations imposed by the transverse nature.

Therefore, the refinement we performed on the WISH data using the harmonic fragment as the Holmium structure is exactly the same, shown in Figure 4.2.6 (right). We plot the value of the ordered moment on the apical site in Figure 4.3.2. Within errors bars we indeed recover the full moment of the Ho^{3+} on this site, of approximately 10 μ_B. However, the refinement in Figure 4.2.6 (right) is visibly not perfect for the two peaks at 2.05 - 2.15 $Å^{-1}$ in particular. We believe the issue is caused by the width of the Holmium magnetic Bragg peaks. They are wider than the experimental resolution and despite trying several combinations of Lorentzian and Gaussian widening, we have not managed to refine them properly. We are still confident that the ordered moment we find is correct because of the consistency with other experiments [Wiebe et al., 2004], and because the first two magnetic peaks are purely magnetic, almost entirely from the Ho ordering, and are better refined. In Figure 4.2.6 (left) we can see that the Holmium Bragg peaks are wider than the experimental resolution: the width at half maximum of the first Ru magnetic peak at 10 K is visibly less than that of the Ho magnetic peak at 1.55 K. The inverse of the half-width at half-maximum of a peak can be interpreted as a correlation length for the associated magnetic phase (provided that it is much larger than the experimental resolution). This yields a correlation length of about 30 Å at 300 mK, corresponding to 3 unit cells or about 12 Holmium neighbors. Therefore, the ordered fragment seems to have relatively small domains.

4.3.3 Diffuse signal

The last main experimental sign of a fragmented ground state is the presence of a diffuse scattering signal in addition to the Bragg peaks. In Figure 4.2.3 (left) we showed the raw diffuse signal seen in the WISH data. The standard procedure in studying the low-Q diffuse signal is to subtract the paramagnetic form factor at each temperature. However it is made difficult in the WISH data because of the background originating from the sample environment. Therefore we instead subtracted the signal at 100 K, where the experimental contribution is the same and the paramagnetic form factor should be quite flat in the Q range below 1.5 Å^{-1}. In Figure 4.3.3

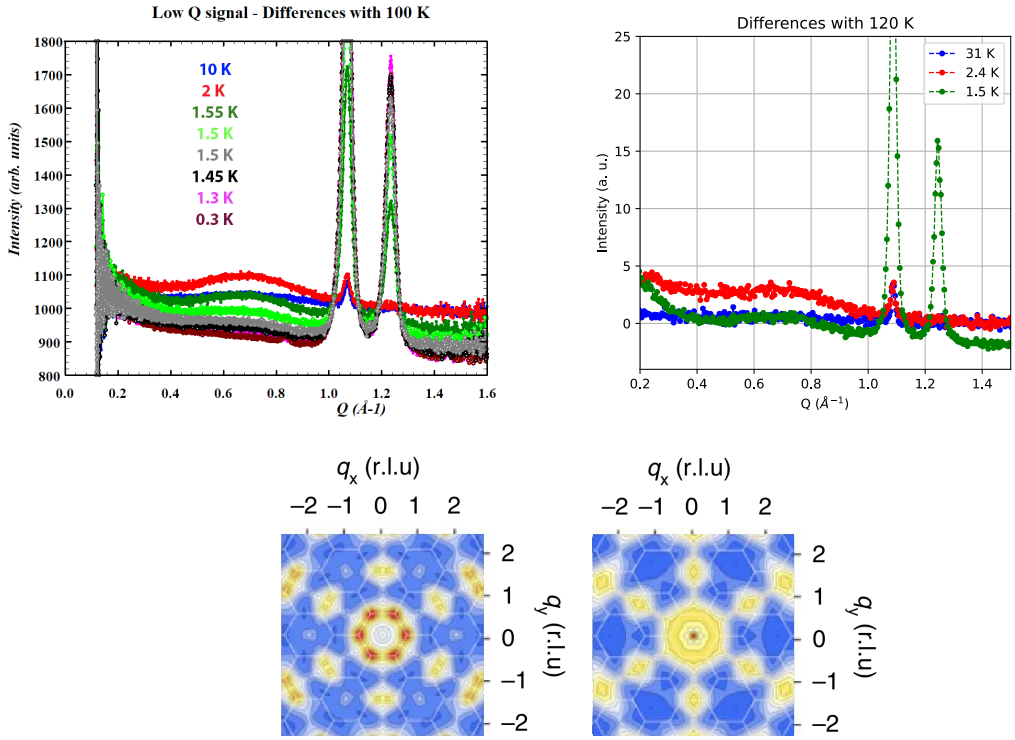

Figure 4.3.3: (top left) Differences of the WISH data with a 100 K reference. (top right) Differences of the D1B data with a 120 K reference. (Bottom) Plots of the simulated diffuse scattering signal from two phases of kagome ice, in the kagome reciprocal axes, reproduced from [Canals et al., 2016].

(top left) we show the result of the subtraction for temperatures close to the transition. It shows that the bump in the diffuse signal is suppressed quickly below the transition, becoming invisible below 1.4 K. At the same time, the spectral weight moves towards $\mathbf{Q} = 0$, forming a very large bump. On the top right, we show the differences we could compute with the data collected on D1B, with essentially the same features. To understand how the diffuse signal can change so drastically below the transition, we would like to compare this data with simulations of the diffuse scattering for different types of kagome spin ice. The powder calculation we have undertaken together with Geoffroy Haeseler was not successful, so we compared our measure-

ments to the single-crystal computations performed in Ref. [Canals et al., 2016]. On the left we show the diffuse scattering for the standard KII kagome ice. It exhibits correlation features in red, which are located roughly where we see a bump experimentally when converting back to pyrochlore reciprocal units. On the right we plot the signal for KI kagome ice, which is a phase where every triangle is in a two-in / one-out or two-out / one-in configuration but do not follow a staggered pattern: there is no magnetic charge order. In this phase the correlation features at low $\mathbf{Q}$ get suppressed. We hypothesize that the apparent disparition of the diffuse signal around $0.65\,\text{Å}^{-1}$ could be due to the presence of such defects. However this is not definitive evidence, and we have planned an experiment on the D1B instrument to study the diffuse scattering at low temperature in more details.

4.4 Modelling and simulations

In order to explain why an antiferromagnetic Γ_5 structure for the ruthenium can induce a ferromagnetic Γ_9 or fragmented phase on the Ho^{3+} ions, it is necessary to investigate the possible interactions between those two ions. A proposed mechanism, investigated in simulations by Julien Robert, is that the ferromagnetic holmium correlations tilt the ruthenium spins out-of-plane, which in turn reinforces those correlations until they favor a [111] order.

4.4.1 Fragmentation in representation theory

First of all we would like to understand how the representation theory presented in Chapter 1 can be used to model fragmentation. In the group representation picture, fragmented ground states are characterized by the coexistence of multiple representations in a single phase: name Γ_3 (all-in / all out) for the ordered longitudinal fragment and Γ_9 for the transverse one. Because the spins are subject to a constraint of fixed length, the solutions of the diagonalized Hamiltonian Equation (1.3.4) are always characterized by one and only one of the moments described in Section 1.3.2, except when the system is located at a phase boundary. However it is important to keep in mind that these solutions apply to a single tetrahedron. Hence if there are several single-tetrahedron solutions that share some spins orientation on some sites, the ground state of the entire lattice can be constructed by joining the various single-tetrahedron solutions at the site in common and tiling the lattice. This approach therefore allows to place a lower boundary on the degeneracy of the macroscopic ground state, and is useful to identify which regions of the phase diagram can host degenerate ground states. To give a simple example, the ground states for the simple ferromagnetic Ising Hamiltonian are all the two-in / two-out tetrahedron which transform under the Γ_9 representation. The tiling rules allow for an extensive amount of possible ground states and give the Pauling estimate of the spin ice entropy.

This discussion should make it clear that in this approach it is not possible to obtain a ground state that is a superposition of different representations on one tetrahedron. However this begs a question: how is the fragmented monopole crystal observed in pyrochlore iridates possible, as every tetrahedron is in a superposition of an Γ_3 and a Γ_9 representation? The answer lies in the fact that the minimal Hamiltonian for a monopole crystal is not a just bilinear exchange,

but also includes a local molecular field of Γ_3 symmetry produced by the Ir^{4+} ions. In general a molecular or external field of the desired symmetry readily gives rise to a new ground state, which can be a superposition of representations or on the contrary reduce the degeneracy of a certain configuration. Another simple example is the case of spin ice under a [111] field. On the scale of a single tetrahedron, the lowest energy configurations are all the two-in / two-out states which have the apical spin fixed along the field. From theses states, the tiling rules can be used to create planes of kagome spin ice separated by triangular planes of apical spins.

4.4.2 Extended molecular field picture

However, in the case of $Ho_2Ru_2O_7$, the molecular field produced by the Ru^{4+} ions on the Ho site is very different to the iridate case, as shown in Figure 4.4.1. We recall that the first Ir neighbours in an Γ_3 configuration (all-in / all-out structure along the local z axis) produce a field along the local z axis on the rare-earth site. However the Ru^{4+} ions in a Γ_5 structure (easy-plane antiferromagnetic structure, with spins pointing along the same local $x-y$ plane) create a field in the $x-y$ plane on the Ho site.

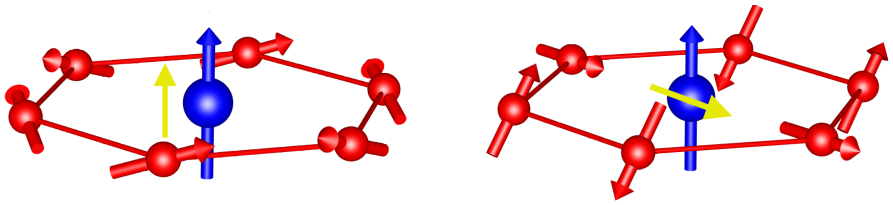

Figure 4.4.1: Molecular field (yellow arrow) produced by the first neighbours metallic ions (in red) on the rare-earth site (in blue), in the case of AIAO ordering in pyrochlore iridates (left) and in the case of $Ho_2Ru_2O_7$ (right)

To understand the possible effect of such a field and extend the simple molecular field picture, the first step is to establish what nearest-neighbor couplings between Ho and Ru ions are allowed by symmetry. Namely, the coupling tensor $\mathscr{J}_{\text{Ho-Ru}_i}$ for a given Ho-Ru link needs to be invariant upon the rotation around the rare-earth site which transforms a Ho-Ru link into the next one. This coupling tensor is then multiplied on both sides by the anisotropy tensor g of each ion. Ho^{3+} is a non Kramers ion so expressed in the local axes, the $g_\perp$ components are zero. We do not have any specific information on the Ru^{4+} ion anisotropy so it will be assumed to be a Heisenberg spin. The general coupling Hamiltonian between nearest neighbor Ho and Ru writes:

$$\mathscr{H}_{\text{Ho-Ru}} = (g_{\text{Ho}}\mathbf{S}_{\text{Ho}})^\top \mathscr{J}_{\text{Ho-Ru}}(g_{\text{Ru}}\mathbf{S}_{\text{Ru}}) \tag{4.4.1}$$

Julien Robert performed the details of the symmetry computations to simplify this Hamiltonian. It turns out that it can be rewritten in the local axes for each ion using only two parameters J_{zz} and $J_{z_\pm}$, where the first index relates to the Ho local axes and the second to the Ru ones:

$$\mathscr{H}_{\text{Ho-Ru}} = J_{zz}S^z_{\text{Ho}}S^z_{\text{Ru}} + J_{z\pm}S^z_{\text{Ho}}\left(\zeta_{\text{Ho-Ru}}S^+_{\text{Ru}} + \zeta^*_{\text{Ho-Ru}}S^-_{\text{Ru}}\right) \tag{4.4.2}$$

where the $\zeta_{\text{Ho-Ru}}$ matrix elements encode the transformation from one Ho-Ru link to another similarly to Equation (1.3.1). The effective Ho only term can be found by summing the above Hamiltonian for the six Ru neighbors around a rare-earth site. But in the case of Ru in a Γ_5 structure, the computation shows the total interaction is zero:

$$\sum_{i=1}^{6} \mathscr{H}_{\text{Ho-Ru}_i} = 0 \tag{4.4.3}$$

Therefore, we cannot explain our observations in a molecular field picture with a pure Ising Ho spin.

4.4.3 Tilting the Ruthenium

In place of the molecular field formalism, where the Ru structure is fixed, we then tried to simulate the coupled dynamics of Ho and Ru with Monte-Carlo simulations. We consider the following Hamiltonian which stabilizes a spin ice for the Ho sublattice, a Γ_5 structure for the Ru sublattice and a simple $J_{z_{\text{Ho}} z_{\text{Ru}}}$ coupling in between the two:

$$\mathscr{H}_{\text{MC}} = \sum_{\langle i,j \rangle} J_{zz} S^z_{i,\text{Ho}} S^z_{j,\text{Ho}} - \sum_{\langle i,j \rangle} J_{\pm} S^+_{i,\text{Ru}} S^-_{j,\text{Ru}} + S^-_{i,\text{Ru}} S^+_{j,\text{Ru}} + \sum_{\substack{\langle i,j \rangle \\ \text{Ho } i \text{ nn Ru } j}} J_{z_{\text{Ho}} z_{\text{Ru}}} S^z_{\text{Ho}} S^z_{\text{Ru}} \tag{4.4.4}$$

with $J_{zz} > 0, J_{\pm} > 0, J_{z_{\text{Ho}} z_{\text{Ru}}} \ll J_{zz}, J_{\pm}$, on which Julien Robert performed Monte Carlo simulations on a system of $4 \times 4 \times 4$ unit cells, *i. e.* 2048 spins total.

The mechanism we want to test is the following. We consider that the two-in / two-out Ho correlations which develop below 2 K can tilt the Ru out of its Γ_5 structure, through the $J_{z_{\text{Ho}} z_{\text{Ru}}}$ coupling. It allows for a Ru tilt along the local z axes that has the same two-in / two-out structure. In return, the tilting creates a non zero molecular field with a two-in / two-out structure on the Ho sublattice, analogous to an external field along a cubic direction [100]. To sum up, Ho ions only interact with the out of plane tilt of Ru ions, that they create themselves to begin with when they start to correlate. In the Monte-Carlo simulations performed with Julien Robert, we have observed that such an interaction indeed drives a transition on the Ho sublattice, but towards a fully ordered spin ice [100] state instead of a fragmented [111] one. This can be understood simply in that the magnetization of a two-in / two-out tetrahedron will always be along a cubic direction [100].

In fact, only a three-in / one-out tilt configuration has a magnetization towards a [111] direction. When interacting with Ru spins with this configuration, one Ho site is surrounded by 6 out-tilted Ru spins while the three others are surrounded by 4 out-tilted and two in-tilted, and therefore has the same energetics as spin ice in a [111] field. A three-in / one-out tilt (or in general any tilt configuration with a magnetization along [111]) is therefore the most straightforward way to generate a the fragmented structure which we claim is the ground state of $Ho_2Ru_2O_7$. To induce this tilt configuration in the simulations, we tried to add terms to the Ru-only Hamiltonian. We introduced an antiferromagnetic Ising term, which favors an all-in / all-out tilt, to compete with the two-in / two-out in a way similar to the monopole crystal. Unfortunately this

approach proved inconclusive. The Ru spin has no particular anisotropy in our simulations, so it can escape any attempt at imposing competing interactions on the tilt by minimizing its out-of-plane component. As a result we were only able to achieve two-in / two-out or all-in / all-out Ru tilts, wether in Monte-Carlo simulations or in numerical minimisations of the energy on the scale of a unit cell. Therefore, we believe that the fragmented [111] ferromagnetic phase cannot occur in a system with only bilinear interactions and that other physical ingredients are needed.

Julien Robert was able to give a general framework to make sense of this observation. He followed the same procedure than in Ref [Yan et al., 2017] to apply representation theory to a bigger unit cell including the metallic site, formed of two tetrahedra, with a general symmetry-allowed bilinear Hamiltonian. In the absence of couplings, the Hamiltonian for both sublattices is a simple sum of two Hamiltonians Equation (1.3.4). But the introduction of the generalized couplings Equation (4.4.2) only allows for interactions between identical representations: a Γ_5 structure for Ru can only couple to the same Γ_5 structure on the Ho site, which has a very large energy because of the Ising anisotropy of Ho. In particular it is not possible to find a ground state which is a superposition of different basis vectors of the Γ_9 representation, like the one of spin ice under a [111] field.

4.4.4 A minimal model for [111] ordering in ferromagnets

Faced with these setbacks, we turned our focus towards establishing a phenomenological model which can host ferromagnetism along the body-centered [111] direction in a cubic system. In the case of pyrochlore magnets, we are specifically looking fo a perturbation to the Ising spin ice Hamiltonian that can lift the degeneracy of the spin ice manifold to keep only the ones where an apical spin is selected and pinned. We believe that such a perturbation requires two ingredients:

- a first interaction which promotes all spin-ice states with a nonzero magnetization from the spin-ice manifold, whatever its direction may be;
- a type of self-consistent repulsive cubic field, which would push the overall magnetization as far away from [100] directions as it can, therefore ending along [111].

These two ingredients can be realized in the following effective perturbation Hamiltonian for the Ho sublattice:

$$\mathcal{H}_{\text{Ho, pert}} = J_3 \sum_{\langle i,j \rangle_3} \mathbf{S}_i \cdot \mathbf{S}_j + U \left(\sum_i \mathbf{S}_i \cdot \mathbf{M} \right)^2 \tag{4.4.5}$$

The first term is a third-neighbor coupling which couples the same pyrochlore sites on neighboring tetrahedra, thus favoring identical tetrahedra configuration if J_3 is negative [Henelius et al., 2016]. The second term is a self-consistent quartic interaction between each spin and the overall magnetization of the system. It could come from an expansion of the long-range interactions, in which we disregard the quadratic terms that can be absorbed into an effective $J_3^{'}$ and in which each term must keep the cubic symmetry of the lattice. If U is positive then it

acts as a repulsive cubic potential. Then, there exists a region of the phase diagram where the fragmented [111] ferromagnet is the ground state. The first term J_3 can already exist in other Ising pyrochlores as a truncation of the long-range dipolar interaction [Henelius et al., 2016]. There now remains to find a plausible origin to the second ingredient and integrating it into the simulations.

4.4.5 Interactions between the magnetic and electronic degrees of freedom

The most promising answer we have found lies into the interaction between the magnetic and electronic degrees of freedom on the Ru sublattice. This was originally investigated in the case of iridates compounds [Goswami et al., 2017; Ladovrechis et al., 2021] as the unfilled $5d$ orbitals of the Ir^{4+} ion are extended in space and therefore their magnetism is not entirely localized. The authors start from the normal metallic state of pyrochlore iridates: a so-called parabolic semimetal (PSM), which at low energy has a quadratic band touching around the Fermi level. They then use group representation theory in a similar way as explained in Chapter 1 to list all the possible local order parameters that an interacting PSM can host. These are interpreted as magnetic structures created by interacting with the itinerant electrons; the authors focus especially on the all-in / all-out and ordered spin ice order parameters. Because of their symmetry, their couplings with the PSM state are constrained. Finally they apply renormalization group theory to write an effective Landau energy for the magnetic orders dressed by such itinerant fermions. We believe that this analysis will apply to Ruthenium ions as well. This is justified by the fact that the Ru $4d$ electrons are also slightly delocalized, so the core concept of magnetic orders interacting with electronic bands should remain valid. The main result of interest for us is the new couplings generated as a perturbation to the Hamiltonian in Equation (1.3.4):

$$\mathscr{H}_{\text{Ru, pert}} = 3u_1^{'}\sum_{i=1}^{3} m_i^4 + 3u_1^{''}\sum_{i<j}^{3} m_i^2 m_j^2 + u_2 m_{\Gamma_3}^4 + 2u_{12}\mathbf{m}_{\Gamma_9}^2 m_{\Gamma_3}^2 \tag{4.4.6}$$

where m_{Γ_3} is the all-in / all-out order parameter the m_i's are the components of the $\mathbf{m}_{\Gamma_9}$ ordered spin ice order parameter. Such new couplings make the following scenario for the Ru tilt possible:

- Ru acquires a two-in / two-out tilt through interactions with the correlated Ho sublattice, and therefore a non zero $\mathbf{m}_{\Gamma_9}$ order parameter;
- the quartic terms with $u_1^{'} < 0$ and $u_1^{''} > 0$ would tend to push this magnetization towards [111], by trying to minimize the projection on a particular cubic axes;
- the u_{12} term mixes the all-in / all-out representation with Γ_9 to obtain a three-in / one-out tilt.

At the time of writing, Julien Robert is working in implementing such quartic terms in the simulations.

4.5 Dynamics and excitations in the fragmented phase

4.5.1 Relaxation times measured in AC susceptibility

We performed AC susceptibility measurements down to frequencies of 1 mHz to study the dynamics above and below the transition. We first measured the AC susceptibility at fixed frequency as a function of temperature, which we report in Figure 4.5.1. We could not measure the curve at 1 mHz over the entire temperature range due to external perturbations which hampered the very long acquisition. On the right we see that the out of phase susceptibility χ'' at 2.1 mHz exhibits two bumps: one close to the transition, which does not significantly move in the frequency range we have explored; and one at a at low temperature (about 1 K) whose temperature increases when frequency in increased. This point towards the existence of two distinct relaxation times in the system. However we also observed that curves measured while heating or cooling do not match together for frequencies above 11 mHz, especially close to the maximum of χ''. We do not understand exactly why this happened, and this made the extraction of the temperature of the maximum as a function of frequency less trustworthy.

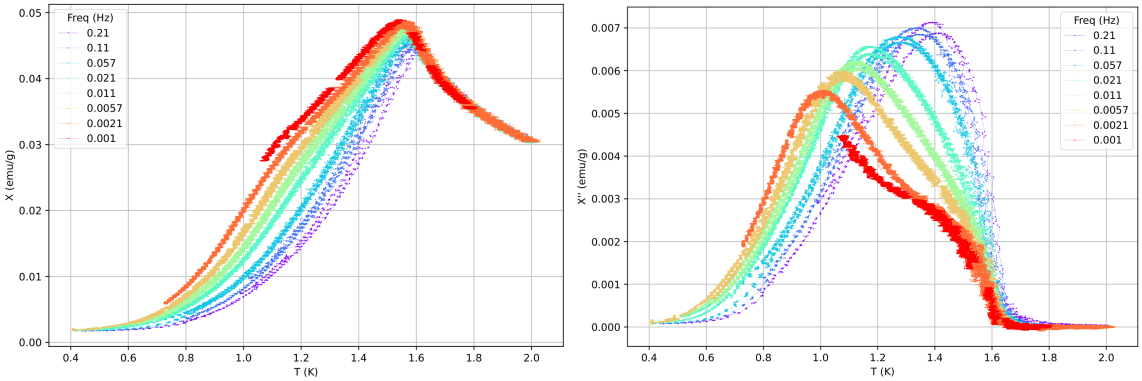

Figure 4.5.1: (left) In phase and (right) out of phase susceptibilities as a function of temperature, measured down to 1 mHz.

We then measured the AC susceptibility at fixed temperature as a function of frequency, on the low field magnetometer. A frequency sweep is performed successively in both coils, then the values subtracted to obtain the absolute susceptibility. The data is shown in Figure 4.5.2. There were significant phase difference factors caused by eddy currents above 110 Hz, causing the upturn in the data. We could not remove completely their effect and this prevented an accurate analysis to be performed. But the out of phase susceptibility χ'' again seems to exhibit two peaks, with a low frequency mode below the transition and a high frequency one above, which coexist around the transition.

To get a more definitive answer we performed a new measurement on another type of dilution magnetometer, tailored to the detection of magnetic fluctuations and noise. It achieves a very large bandwidth (1 mHz - 10 kHz) in part thanks to a Silicon sample holder which does not create eddy currents. However the measurement does not give absolute values of the susceptibility. The data were collected and corrected for phase differences by Félix Morineau, and are

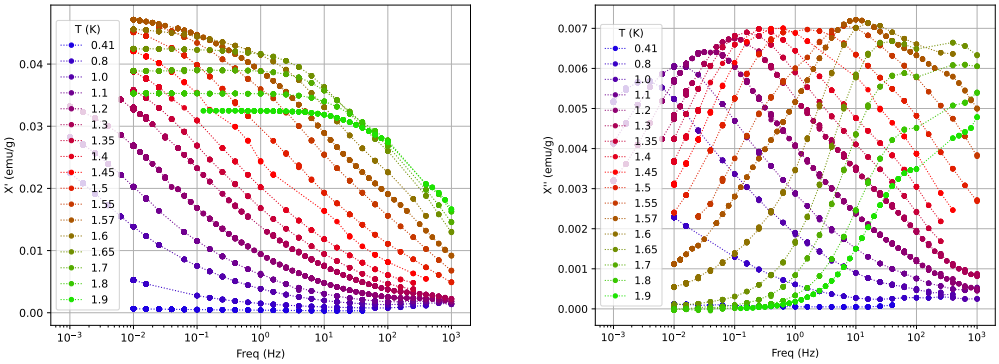

Figure 4.5.2: (left) In phase $\chi'(f)$ and (right) and out of phase $\chi''(f)$ susceptibilities measured on the low-field magnetometer.

shown in Figure 4.5.3.

This dataset makes it is clear that $Ho_2Ru_2O_7$ has two characteristic time scales. Qualitatively, the out of phase susceptibility χ'' has two bumps: one dominates below the transition at frequencies below 100 Hz, and another takes over above the transition at frequencies above 1000 Hz. Therefore, we elected to fit the data using a model with two relaxation times, each contributing a certain fraction of the total signal. We took into account a symmetric spread of relaxation times through a generalized Debye model:

$$\chi(f) = \chi_S + (\chi_T - \chi_S)\left(\frac{\eta}{1+(2i\pi f\tau_l)^{1-\alpha_l}} + \frac{1-\eta}{1+(2i\pi f\tau_s)^{1-\alpha_s}}\right) \tag{4.5.1}$$

where χ_T is the DC susceptibility, χ_S is the high frequency limit called adiabatic susceptibility. The two times τ_l and τ_s are the characteristic times for the long (or slow) and short (or fast) processes respectively, with spread parameters α_l and α_s and relative amplitude η. $\alpha = 0$ corresponds to the single time Debye model. In order to constraint the fit, the times scales were fitted on the χ'' data, then fixed to fit the rest of the parameters on the χ' data. The α parameters were also set to 0 if the amplitude of the related mode is too small. The fits are represented in Figure 4.5.3 by dashed lines. They could not be performed accurately below 1 K because the relaxation times become longer than 10^3 seconds.

In Figure 4.5.4 we show the parameters of the two modes estimated by the fits. Our main result is the characteristic time scales as a function of the inverse temperature, shown on top. It confirms that there are two separate time scales, which coexist around the transition. Below the transition, the slow process timescale can be fitted by an Arrhenius process with energy barrier $\Delta E_l = 15$ K and $\tau_{0l} = 1.1 \times 10^{-5}$ s. Above the transition, the fast mode can be fitted by an Arrhenius process between 2 and 4 K with energy barrier $\Delta E_s = 6$ K and $\tau_{0s} = 5.5 \times 10^{-7}$ s. On the bottom left we show the estimated DC susceptibilities for each mode as well as their sum. The slow mode arises very abruptly at the transition, while the fast mode only gets gradually suppressed below the transition. On the bottom right we show the spread of relaxation time of

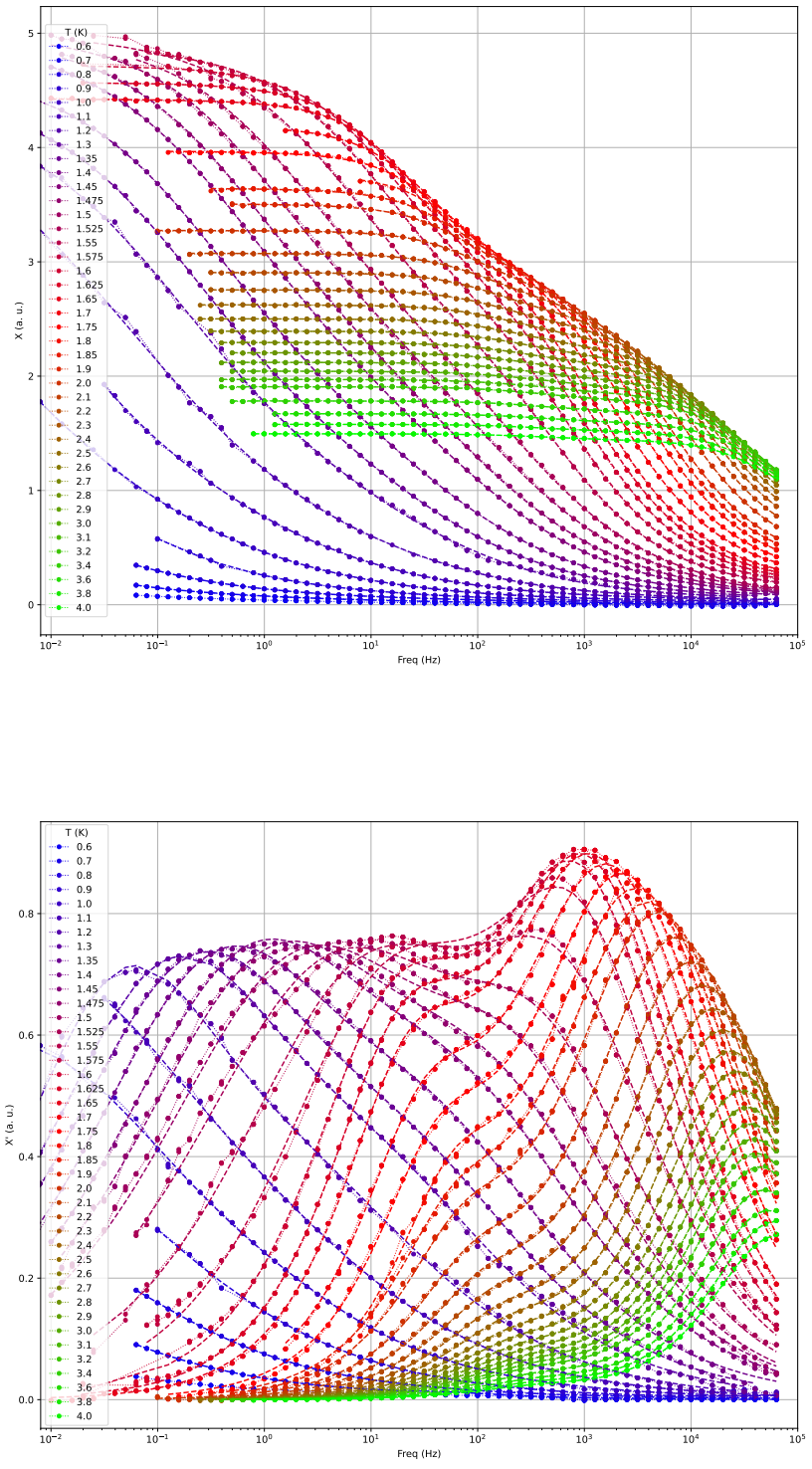

Figure 4.5.3: (Top) In phase χ' and (bottom) and out of phase χ'' susceptibilities measured on the noise magnetometer. The data points are the dots linked by thin dotted lines. The thick dashed line are a fit by the model.

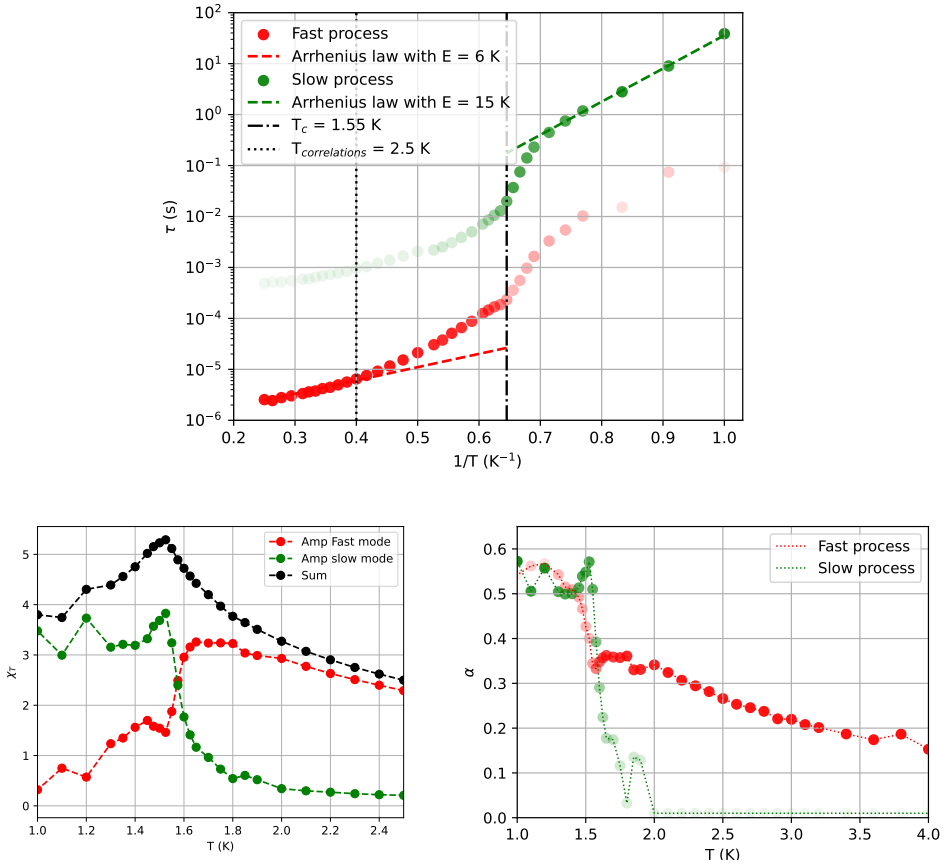

Figure 4.5.4: (top) Characteristic times as a function of the inverse temperature. The red and green dots are the results from the fit with the model, with the transparency representing their relative amplitude. The dot-dashed line is the transition temperature, and the dashed line is the temperature from which ferromagnetic correlations start to appear in neutron diffraction experiments. (bottom left) DC susceptibility of each mode in red and green, and their sum in black. (bottom right) Spread of relaxation times α of each mode.

each mode, which again shows very different behaviors for the slow and fast processes.

To our knowledge this type of coexistence of two separate time scales has not been observed in other Ising pyrochlores. At 2 K, the characteristic time scale we measure on $Ho_2Ru_2O_7$ is comparable to measurements on $Ho_2Ti_2O_7$ made by Sean Giblin on a high-frequency susceptometer[1], as well as measurements published in Ref. [Wang et al., 2021]. However at 1 K $Ho_2Ru_2O_7$ has a time scale almost 2 orders of magnitude slower than $Ho_2Ti_2O_7$. In Ref. [Wang et al., 2021], the authors identified two timescales in $Ho_2Ti_2O_7$, with energy barriers 15 and 18 K for the slow and fast processes respectively. They argued that they correspond to a single monopole diffusion process for the slow process which dominates below 1.2 K, and the creation of north / south monopole bound pairs for the fast process which dominates above 1.2 K. However the two time

[1]Private communication.

scales join in a thermal crossover, with no comparison to the sharp transition we observe. In Ref. [Matsuhira et al., 2011], the authors identified again two separate time scales in $Dy_2Ti_2O_7$, with energy barriers 9.2 and 6.3 K for the slow and fast processes respectively. Down to 0.5 K, they coexist with relative amplitudes that do not dramatically change with temperature: the slow mode has an a amplitude about twice as large as the fast mode. The authors mentioned that these two time scales could correspond to the free and bound monopole states but did not conclude affirmatively. On the contrary, in pyrochlore iridates $Ho_2Ir_2O_7$ and $Dy_2Ir_2O_7$, only a single time scale was clearly seen in alternative susceptibility measurements. The energy barriers were found to be 4.8 and 3.6 K respectively [Lefrançois et al., 2017; Cathelin et al., 2020]. In both cases the energy scale was of the same order of magnitude as that of the creation of a defect in the monopole crystal state.

In the absence of a universal picture for the characteristic time scales in Ising pyrochlores, we want to mention a possible interpretation of our data assuming the ground state is indeed a fragmented structure similar to the kagome plateau under a [111] field:

- The fast mode would correspond to the creation of single monopoles excitation from the spin ice manifold. Indeed its energy barrier between 2 and 4 K is very close to the chemical potential of monopoles in Holmium pyrochlores;
- The slow mode would correspond to the constrained motion of monopoles between kagome planes in the ordered phase. Hopping from one plane to the next requires flipping the apical spin, which should have a higher energy barrier due to the internal fields. In the ordered phase, what remains of the fast mode would be associated to the motion of excitations within kagome planes. This propagation should occur perpendicularly to the internal field created by the magnetic order and should therefore have a smaller energy scale.

4.5.2 Inelastic scattering

An especially suitable technique to access the interactions is to probe the magnetic excitations through inelastic neutron scattering measurements. We were able to perform an Xpress experiment on the time-of-flight spectrometer LET at ISIS, for a day of measurements and 3 temperatures. The data were collected by Ross Stewart.

At 100 K we see two non-dispersive excitations centered around positive energy transfers 1.5 and 4.8 meV. Similar excitations were observed in Ref. [Wiebe et al., 2004; Gardner et al., 2005]. The authors interpreted them as transitions between excited Ho^{3+} crystal field states. Indeed the first excited levels have an energy of about 200 K and so at this temperature they can be thermally populated.

At 1.5 K, we see again two flat excitations but centered around energies 1.4 and 2.7 meV. At this temperature the crystal field excited states should not be occupied so this signal could come from a splitting of the ground state doublet. Ho^{3+} is a non Kramers ion so in an effective spin 1/2 picture the doublet can only be split by a longitudinal magnetic field. By including the full crystal field structure there can be a small transverse splitting, but very small for a field of the

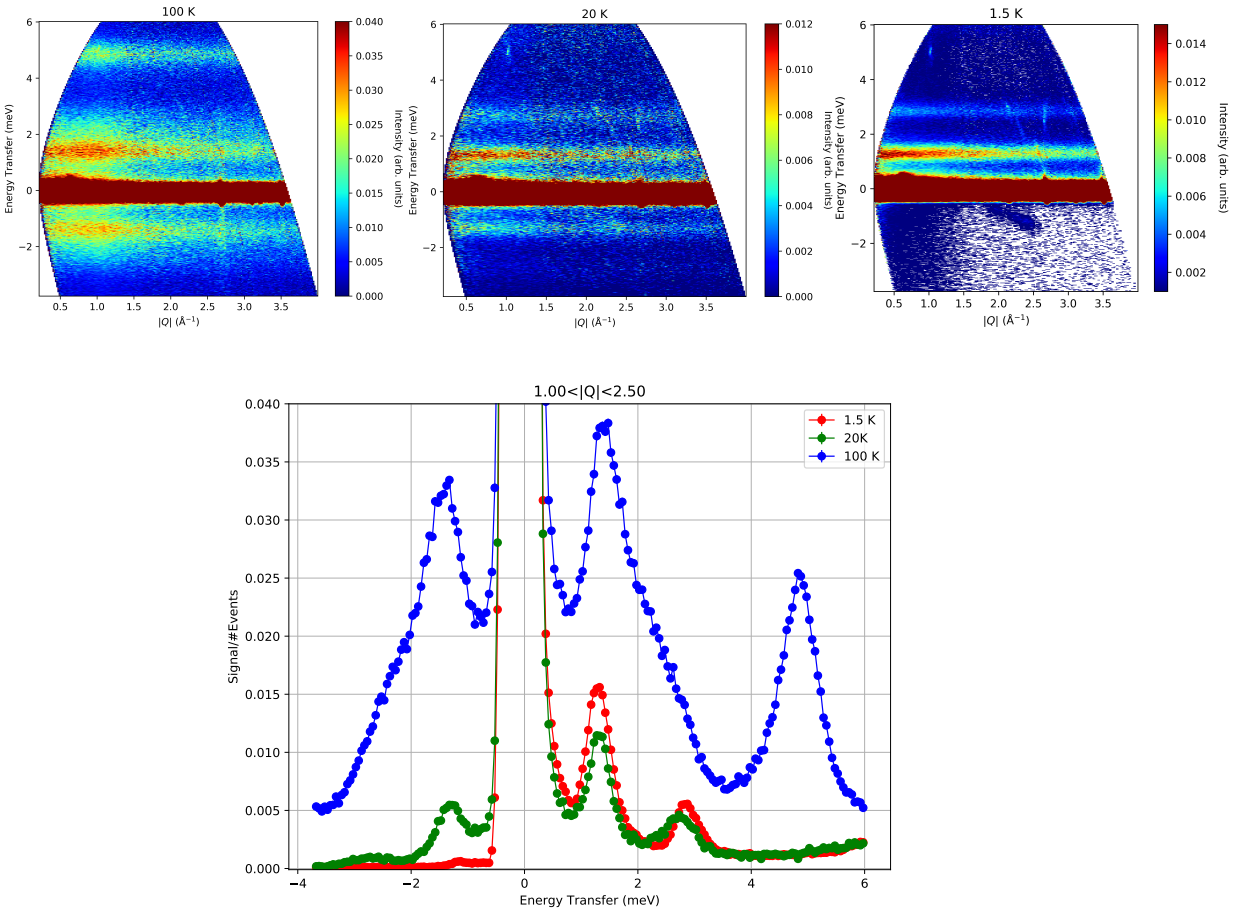

Figure 4.5.5: (top row) Inelastic scattering at temperatures of 100, 20 and 1.5 K (left to right) with 7.52 meV incoming energy. (bottom) Integration of the signal over $\mathbf{Q} \in [1, 2.5]$ Å^{-1} with 7.52 meV incoming energy.

order of magnitude of a few Teslas [Tomasello et al., 2015]. Therefore, we do not expect the direct molecular field of the Ru magnetic order to significantly affect the Ho crystal field structure. There is a interesting interpretation of these two excitations in the ground state we propose for $Ho_2Ru_2O_7$. This state creates an internal field along [111] which has a different projection along the local z axes for the apical or kagome plane spins. The kagome spins see a longitudinal field that is only 1/3 the value of that for the apical spin. So in this structure there should be two different splittings of the doublet depending on the site. However the ≈ 3 meV splitting would correspond to a unusually large internal field.

The signal measured at 20 K is the most peculiar and we have not succeeded in understanding where it originates from. We see two flat excitations again around energies 1.5 and 2.8 meV. At this temperature there should not be any significant thermal population of excited crystal field states. At the same time, the Ho sub lattice is not ordered so the signal cannot be caused by a splitting of the doublet. Therefore we need to consider other possible interactions. Two

possibilities would be the quadrupolar interactions with the phonons, or the collective effects involving several spin flips in a single excitations. Another less exciting explanation is that the two excitations at 1.5 and 20 K originate from an impurity like Ho_2O_3, since measurements in $Ho_2Ir_2O_7$ seem to show a similar signal at low temperature[2]. Further measurements with a more precise temperature dependence would be needed to confirm the simple interpretation at 1.5 K and understand the 20 K signal.

4.6 Conclusions: a classical, unsaturated, [111] ferromagnet

To conclude, we believe that we have identified the correct ground state of $Ho_2Ru_2O_7$. This work was motivated by the possibility to explore the fragmentation phase diagram thanks to the magnetism of the Ru^{4+} ions, as well as a critical analysis of existing results [Wiebe et al., 2004; Gardner et al., 2005]. This drew us to perform our own experiments which we analyzed in the framework of fragmentation.

$Ho_2Ru_2O_7$ exhibits a magnetic transition on the Ho sublattice at 1.55 K. It is characterized by a non-zero residual entropy, an incomplete ordered moment and a diffuse signal at low-Q in neutron diffraction which persists to some extent below te transition. This is consistent with a type of fragmented state similar to that of classical spin ice under a moderate [111] field. It has a unsaturated ferromagnetic order parameter, which maps onto the harmonic fragment of the Helmholtz decomposition, and a disordered part following the local rules of kagome ice. This is a new exotic state, to be contrasted with the partial antiferromagnetic ordering in the iridate pyrochlores, or the $S = 1/2$ Heisenberg antiferromagnet [Singh et al., 1992]. In the field of classical pyrochlore spin ices, a similar ferromagnetic Coulomb phase was found in a system with a uniaxial distortion and a four-spin perturbative interaction [Powell, 2015]. But the unsaturated phase appeared only as an intermediate state between the paramagnetic and fully ordered phases, with a continuously varying magnetization.

There still remains some experimental features of $Ho_2Ru_2O_7$ that we have not understood yet. AC susceptibility measurements show two distinct relaxation times which are likely associated to two different magnetic excitations. In a short inelastic scattering experiment, we saw two peculiar excitations at low temperatures but could not conclude on wether they come from the sample or from impurities. At the time of writing, we have a new diffraction experiment with a dilution fridge planned on D1B at ILL, and we have made a proposal for a longer inelastic scattering experiment.

[2] Unpublished data.

Chapter 5

Exploring the phase diagram of fragmentation

Contents

5.1 Motivation for experiments under pressure

The fragmentation phase diagram presented in Chapter 1 (Figure 1.2.6) has been useful to locate different compounds and classify they ground state. However, the presence of nearly temperature-independent phase boundaries at low temperature makes it difficult to observe a transition between the various fragmented phases. It requires moving horizontally in the phase diagram, that is to change the parameters that govern the creation of monopoles and the staggered chemical potential.

Such a test is easier to perform numerically, as is done in Refs. [Raban, 2018; Raban et al., 2019]. Here the authors performed Monte-Carlo simulations of the dumbbell model with a staggered chemical potential. They studied the out-of-equilibrium response as the staggered chemical potential was cycled at different speeds through the line of second-order phase transitions that separates spin ices from monopole crystals. The order parameter of the transition (i.e. the density of crystallized monopoles) was observed to have a hysteretic response, which grew as the cycling speed increased. They hypothesized that this was due to the critical slowing down close to the transition, as here the dynamical properties of the system are driven by the critical fluctuations. This was confirmed by the fact that the widths of the hysteresis cycle at all sweep frequencies could be collapsed onto a single scaling law, called the Kibble-Zurek scaling, introduced for condensed matter systems in Ref. [Hamp et al., 2015]. Additionally it was found that the critical exponents of a 3D Ising model could accurately describe the slowing dynamics.

The Kibble-Zurek scaling procedure could also be done with temperature sweeps with a putative material sufficiently close to the phase boundaries. Unfortunately, as seen in Figure 1.2.6 either the titanate or iridate pyrochlore are located more or less in the center of their respective regions of the phase diagram. Hence, we tried to move in the phase diagram by changing the interatomic distances and angles and therefore modify the interactions within the same model. This can be done by chemical substitution, which we tried initially with $Ho_2Ru_2O_7$ but resulted in different physics. The other popular option is to use mechanical hydrostatic pressure in a pressure cell. The first challenge it poses it that it is hard to predict how the magnetic interactions might change. As said in Equation (1.2.5) the dipolar interaction D varies as $1/r^3$ and is somewhat predictable under pressure. However, the exchange J between rare-earth is a superexchange mediated by the Oxygen atoms. It generically depends on the distance as $1/r^5$ but also on the angle between the oxygen and rare-earth atoms, whose evolution under pressure is hard to predict.

The second challenge is to choose adequate probes of the magnetic structure. The various pressure setups introduce complications in the data analysis which we will discuss. Hence we cannot expect one single probe to give a definitive answer, and our objective is to combine signals from neutron diffraction and specific heat under pressure. But this prudent approach leads to a different hurdle: the material properties of the two known examples of fragmented spin ices are not suited to both these techniques at the same time. On the one hand $Ho_2Ir_2O_7$ has a large Schottky anomaly coming from the Ho nucleus, and we only had access to polycristalline samples, which makes it complicated to study its specific heat under pressure. On the other hand some isotopes present in natural Dysprosium are major neutron absorbers, ren-

dering difficult any neutron diffraction under pressure. We therefore used each material for the technique it is the most suited for. The chapter is structured as follows. In the first section, we present an extension of the mean-field theory of fragmentation that we presented in Chapter 1. We will make use of it to compute the two observables we can measure under pressure and find how they might change as a material moves in the fragmentation phase diagram. We then move on to the experimental results. We performed specific heat measurements under pressure on $Dy_2Ir_2O_7$ using the AC technique described in Chapter 2, as well as neutron diffraction under pressure on $Ho_2Ir_2O_7$. But the specific heat data was especially hard to interpret, so we performed additional AC specific heat measurements at ambient pressure on the same crystal. These proved very important in understanding the behavior of spin ice materials and so we will discuss them first.

5.2 Extended mean-field theory of fragmented spin ices

5.2.1 New parameters

In this section our goal will be to get an understanding of how observables like the specific heat and ordered moment might change as we move through the fragmentation phase diagram across a phase boundaries. To this end we will extend the mean-field theory of the $S = 1$ Blume-Capel model developed in Chapter 1 (see Equation (1.2.31)) to address some of its limitations:

- include the energetics of the double monopoles;
- take into account the entropy of the fragmented phase.

Therefore we chose to introduce two new mean-field quantities ρ_2, ϕ_2 the density of double monopoles and the value of the symmetry breaking between the A/B diamond sites respectively. Similarly to the single monopole case detailed in Equation (1.2.25), they are defined such that the density of double positive or negative monopoles on a A or B diamond site can be written

$$\begin{aligned} \frac{N_{A,++}}{N} &= \rho_2 \frac{1+\phi_2}{2}, \quad \frac{N_{B,++}}{N} = \rho_2 \frac{1-\phi_2}{2}, \\ \frac{N_{A,--}}{N} &= \rho_2 \frac{1-\phi_2}{2}, \quad \frac{N_{B,--}}{N} = \rho_2 \frac{1+\phi_2}{2} \end{aligned} \tag{5.2.1}$$

We will work in the same reduced units presented in Equation (1.2.20). In the most general model the double monopoles could be allowed to break the symmetry in a direction opposite to the single monopoles. This would be controlled by a pair new conjugated potentials $\bar{\nu}_2$, $\bar{\Delta}_2$ for the double monopoles only. The mean-field enthalpy in Equation (1.2.27) can be readily promoted to

$$\bar{H}\left(\rho_1, \phi_1, \rho_2, \phi_2\right) = -\frac{1}{2}\left(\rho_1\phi_1 + 2\rho_2\phi_2\right)^2 + \bar{\nu}_1\rho_1 + \bar{\nu}_2\rho_2 - \bar{\Delta}_1\phi_1\rho_1 - \bar{\Delta}_2\phi_2\rho_2 \tag{5.2.2}$$

5.2.2 Computation of the entropy

As explained in Equation (1.1.5), the non-zero residual entropy of the fragmented monopole crystal phase cannot be captured in the Pauling independent tetrahedron approximation. Its true value can only be obtained from a loop expansion of the associated dimer problem [Nagle, 1966; Nagle, 2004], which as a minimum involves a six-tetrahedra loop. Inspired by a note in the appendix of Ref [Kaiser et al., 2018], and in the effort of keeping the computation as simple as possible, we choose the median route of considering the model as a set of independent bi-tetrahedra, formed of two adjacent A and B tetrahedra. We will enumerate the micro-states for these objects and perform the equivalent of the Pauling approximation to compute the entropy.

Bi-tetrahedra are formed of 7 spins, of which 1 is internal and 6 are shared with neighboring bi-tetrahedra. Therefore there are $2^7 = 128$ micro states in an isolated bi-tetrahedron. However only half of the shared spins can be chosen freely as the other half must be kept compatible with neighboring bi-tetrahedra. Hence the total number of states for a system of $N/2$ bi-tetrahedra can be approximated by

$$W = \frac{1}{2}^{3\frac{N}{2}} \frac{(N/2)!}{N_1! \cdots N_{128}!} \tag{5.2.3}$$

We now group the 128 states together depending on how what monopole charge they have on the A and B sites, which we present by the symbol $\{\alpha\beta\}$. This is where our approach diverges from Ref [Kaiser et al., 2018] as we do not consider $+/-$ and $-/+$ microstates (and all other non-symmetric monopole configurations) as participating to the same macrostate. The full enumeration is shown in Table 5.2.1.

$\emptyset\emptyset$	$+\emptyset$	$\emptyset+$	$-\emptyset$	$\emptyset-$	$+-$	$-+$	$++$	$--$	$\overset{+}{+}\emptyset$	$\emptyset\overset{+}{+}$	$\overset{-}{-}\emptyset$	$\emptyset\overset{-}{-}$
18	12	12	12	12	10	10	6	6	3	3	3	3

$\overset{+}{+}-$	$-\overset{+}{+}$	$\overset{-}{-}+$	$+\overset{-}{-}$	$\overset{+}{+}+$	$+\overset{+}{+}$	$\overset{-}{-}-$	$-\overset{-}{-}$	$\overset{+}{+}\overset{-}{-}$	$\overset{-}{-}\overset{+}{+}$
3	3	3	3	1	1	1	1	1	1

Table 5.2.1: Multiplicities of all the $\{\alpha\beta\}$ states.

We compute the entropy per tetrahedron in the thermodynamic limit using Stirling's formula:

$$\bar{S} = \frac{S}{k_B N} = -\frac{1}{2}\ln(W) = -\frac{1}{2}\sum_{\text{configs}\{\alpha\beta\}} \frac{N_{\{\alpha\beta\}}}{N/2} \ln\left(\frac{2^3 N_{\{\alpha\beta\}}}{m_{\{\alpha\beta\}} N/2}\right) \tag{5.2.4}$$

where $m_{\{\alpha\beta\}}$ is the multiplicity of a given configuration.

The next step is to relate the bi-tetrahedra densities to our single A/B tetrahedron densities. The former is proportional to the product of the latter but up to numerical coefficient accounting for the different multiplicities between the single and bi-tetrahedra charge configuration. The general rule is to divide the bi-tetrahedron multiplicity by the product of the single tetrahedron multiplicities.[1] For example, there are $10/128$ $+-$ bi-tetrahedron states, but on a single

[1] Vojtěch Kaiser, private communication

tetrahedron only 4/16 correspond to a given single + or − monopole. So

$$n_{+-} = \frac{N_{+-}}{N/2} = \frac{10}{128} / \left(\frac{4}{16} \times \frac{4}{16} \right) n_{A,+} n_{B,-} = \frac{5}{4} n_{A,+} n_{B,-}$$

. Similarly, there are 3/128 $\varnothing^{\,+}_{\,+}$ bi-tetrahedron states, but on a single tetrahedron 6/16 correspond to an empty site $\varnothing$ and only 1/16 to a double monopole $^{\,+}_{\,+}$, so

$$n_{\varnothing^{\,+}_{\,+}} = \frac{3}{128} / \left(\frac{6}{16} \times \frac{1}{16} \right) n_{A,\varnothing} n_{B,^{\,+}_{\,+}} = 1 \times n_{A,\varnothing} n_{B,^{\,+}_{\,+}}$$

. The other coefficients are computed in a similar way.

Finally we perform the mean-field step where we introduce our mean-field parameters defined in Equation (5.2.1) in place of the single tetrahedron densities. Every density of a given monopole on a given sublattice involves its respective crystallization parameter $\phi_{1,2}$. The only quantity independent of any ϕ is the density of empty tetrahedra which is symmetric with respect to A/B inversion so is replaced by $1 - \rho_1 - \rho_2$. We obtain the following expression for the

entropy per tetrahedron:

$$
\begin{aligned}
\bar{S}(\rho_1,\phi_1,\rho_2,\phi_2) = \frac{S}{k_B N} = -\frac{1}{2}\Bigg(& (1-\rho_1-\rho_2)^2 \ln\left(\frac{8(1-\rho_1-\rho_2)^2}{18}\right) \\
& + 2\rho_1\frac{(1+\phi_1)}{2}(1-\rho_1-\rho_2)\ln\left(\frac{8\rho_1\frac{(1+\phi_1)}{2}(1-\rho_1-\rho_2)}{12}\right) \\
& + 2\rho_1\frac{(1-\phi_1)}{2}(1-\rho_1-\rho_2)\ln\left(\frac{8\rho_1\frac{(1-\phi_1)}{2}(1-\rho_1-\rho_2)}{12}\right) \\
& + \frac{5}{4}\rho_1\frac{(1+\phi_1)}{2}\rho_1\frac{(1+\phi_1)}{2}\ln\left(\frac{8\rho_1\frac{(1+\phi_1)}{2}\rho_1\frac{(1+\phi_1)}{2}}{10}\right) \\
& + \frac{5}{4}\rho_1\frac{(1-\phi_1)}{2}\rho_1\frac{(1-\phi_1)}{2}\ln\left(\frac{8\rho_1\frac{(1-\phi_1)}{2}\rho_1\frac{(1-\phi_1)}{2}}{10}\right) \\
& + \frac{3}{2}\rho_1\frac{(1+\phi_1)}{2}\rho_1\frac{(1-\phi_1)}{2}\ln\left(\frac{8\rho_1\frac{(1+\phi_1)}{2}\rho_1\frac{(1-\phi_1)}{2}}{6}\right) \\
& + 2\rho_2\frac{(1+\phi_2)}{2}(1-\rho_1-\rho_2)\ln\left(\frac{8\rho_2\frac{(1+\phi_2)}{2}(1-\rho_1-\rho_2)}{3}\right) \\
& + 2\rho_2\frac{(1-\phi_2)}{2}(1-\rho_1-\rho_2)\ln\left(\frac{8\rho_2\frac{(1-\phi_2)}{2}(1-\rho_1-\rho_2)}{3}\right) \\
& + 3\rho_2\frac{(1+\phi_2)}{2}\rho_1\frac{(1+\phi_1)}{2}\ln\left(\frac{8\rho_2\frac{(1+\phi_2)}{2}\rho_1\frac{(1+\phi_1)}{2}}{3}\right) \\
& + 3\rho_2\frac{(1-\phi_2)}{2}\rho_1\frac{(1-\phi_1)}{2}\ln\left(\frac{8\rho_2\frac{(1-\phi_2)}{2}\rho_1\frac{(1-\phi_1)}{2}}{3}\right) \\
& + \rho_2\frac{(1+\phi_2)}{2}\rho_1\frac{(1-\phi_1)}{2}\ln\left(8\rho_2\frac{(1+\phi_2)}{2}\rho_1\frac{(1-\phi_1)}{2}\right) \\
& + \rho_2\frac{(1-\phi_2)}{2}\rho_1\frac{(1+\phi_1)}{2}\ln\left(8\rho_2\frac{(1-\phi_2)}{2}\rho_1\frac{(1+\phi_1)}{2}\right) \\
& + \rho_2\frac{(1+\phi_2)}{2}\rho_2\frac{(1+\phi_2)}{2}\ln\left(8\rho_2\frac{(1+\phi_2)}{2}\rho_2\frac{(1+\phi_2)}{2}\right) \\
& + \rho_2\frac{(1-\phi_2)}{2}\rho_2\frac{(1-\phi_2)}{2}\ln\left(8\rho_2\frac{(1-\phi_2)}{2}\rho_2\frac{(1-\phi_2)}{2}\right)\Bigg)
\end{aligned}
\tag{5.2.5}
$$

Such an expression requires some sanity checks:

- For a vacuum of monopoles, $\bar{S}(0,0,0,0) = \ln\left(\frac{3}{2}\right) \approx 0.405$ per tetrahedron is the same entropy as obtained with the simple Pauling approximation;
- For a crystal of monopoles, $\bar{S}(1,1,0,0) \approx \ln(1.15) = 0.203$ has a non zero value contrary to the single tetrahedron approximation. Our approach allows to consider the intrinsic entropy of the fragmented phase, despite giving only a qualitative approximation to the true value of about $\ln(1.3)$;

- For a crystal of double monopoles, $\bar{S}(0,0,1,1) \approx -1.04$. This is erroneous because the entropy cannot be negative, and the entropy of this particular state is known to be 0. This artefact arises for the same reasons as in the single tetrahedron entropy discussed in Chapter 1, that is when the number of microstates W is too small and Stirling's approximation breaks down. It indicates that our entropy approximation cannot be trusted anymore when the density of double monopoles becomes large.
- Even when discounting the double monopoles and setting $\rho_2, \phi_2 = 0$, we recover an expression which is more complex than the simple lattice gas in Chapter 1 and includes some pair correlations.

5.2.3 Grand potential and obtention of the phase diagram

Going back to the case of spin ice we can impose some restrictions on the expression of the enthalpy in Equation (5.2.2). From the nearest-neighbor model of spin ice we know that isolated double monopoles have an energy creation cost 4 times that of a single monopole, so we choose $\bar{\nu}_2 = 4\bar{\nu}$. Additionally, the origin of the staggered chemical potential as a molecular field from the Ir^{4+} ions forces $\bar{\Delta}_2 = 2\bar{\Delta}$. Thus, we will numerically minimize the following free energy to obtain a complete phase diagram of spin ice.

$$\bar{\Omega}(\rho_1, \phi_1, \rho_2, \phi_2) = -\frac{1}{2}(\rho_1\phi_1 + 2\rho_2\phi_2)^2 + \bar{\nu}(\rho_1 + 4\rho_2) - \bar{\Delta}(\phi_1 + 2\phi_2\rho_2) - \bar{T}\bar{S}(\rho_1, \phi_1, \rho_2, \phi_2) \quad (5.2.6)$$

This function is not straightforward to minimize numerically as the parameters are constrained by strong bounds ($\rho \in [0,1], \phi \in [-1,1]$) where the global minimum is often located. As such any single pass of a minimization algorithm has a high chance of getting stuck in a local minimum, and incorrectly identify the phase boundaries at low temperature. Not finding any elegant solution to this issue, we decided to brute-force the problem by employing the Basin-hopping method [Wales et al., 1997]: it consists in performing multiple local minimization from randomly chosen starting points, and accepting the new minimum according to a Metropolis-like criterion. The only downside of this approach is the extended computation time. Using SciPy, we found that the `L-BFGS-B` algorithm worked best for the local minimization step and performed the global minimization to obtain the following phase diagrams, where we plot our order parameter: the crystallized density of monopoles $\rho_1\phi_1 + 2\rho_2\phi_2$.

In Figure 5.2.1 (left) we show the phase diagram in the $(\bar{\nu}, \bar{T})$ plane obtained at $\bar{\Delta} = 0$. We recover a qualitative feature of what is expected for the dumbbell model phase diagram: a low density fluid phase (spin ice, in black) for $\bar{\nu} > 0.5$, and a crystal of double monopoles (in yellow) for lower $\bar{\nu}$, separated by a line of second-order transitions at temperatures $\bar{T}$ above 0.25 approximately. Interestingly, we find a small intermediate region of stability for the crystal of (single) monopoles (in purple) below this temperature, which is not expected in the dumbbell model [Guruciaga et al., 2014]. It does however exist in the Blume-Capel $S = 2$ model [Lara et al., 1998]. We think that its existence in our model is a result our the erroneous entropy given to the double monopole crystal: because its value is so low, it loses out in the competition with

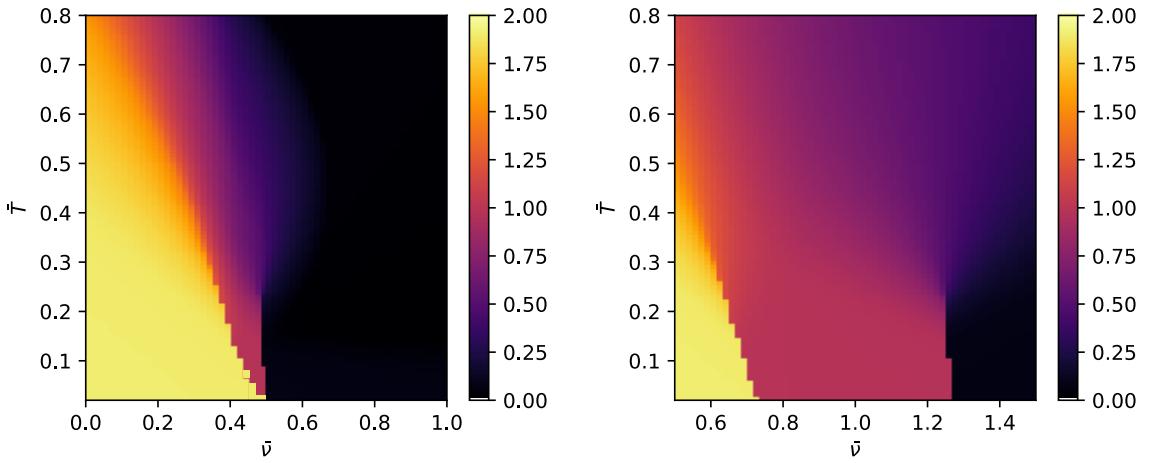

Figure 5.2.1: Density of crystallized monopoles as a color scale, for $\bar{\Delta} = 0$ (Left) and $\bar{\Delta} = 0.8$ (Right)

the single monopole crystal apart from at the lowest temperatures. This artefact can however be tuned out of our model by changing the ratio $\bar{\nu}_2/\bar{\nu}_1$ away from 4 towards lower values.

Contrary to what was anticipated in Ref [Raban, 2018], we notice that the temperature of the critical end point between the fluid phase is lower (at ≈ 0.23, corresponding to $T = u(a)\alpha\bar{T} \approx 1.1$ K) than what was obtained without the inclusion of the monopole crystal residual entropy (≈ 0.33, see Figure 1.2.7). Indeed it was expected to stabilize this phase more and push the mean-field critical point to even higher temperatures. We believe that this is thanks to the fact that our approach favors the formation of pairs from a purely entropic viewpoint, as detailed above, which favors the melting of the monopole crystal phase through defects. Therefore this enabled us to include pair correlations without investigating the full effect of the dipolar interactions between charges. This is the main limitation of our analysis: the long range dipolar interactions only contribute through the $-\frac{1}{2}\left(\rho_1\phi_1 + 2\rho_2\phi_2\right)^2$ term. In the fluid phase, or when defects start to proliferate, they are mostly ignored because $\rho_1\phi_1 + 2\rho_2\phi_2$ is close to 0. As a comparison, the temperature of the critical point found in Dumbbell model simulations is about $\bar{T} \approx 0.07$ or $T \approx 400$ mK

In Figure 5.2.1 (right) we show the phase diagram for $\bar{\Delta} = 0.8$. As expected we find that the monopole crystal now occupies an extended region of the phase diagram. Each of the first order transition boundaries between the various ground states is terminated by a critical point where a second-order transition occurs. The most interesting feature is the fact that the lines of first order transition between phases are not vertical. In fact this is what is expected from the Clausius-Clapeyron relation presented in Equation (1.2.32) when the low-temperature phases have different entropies. The spin-ice / monopole crystal phase boundary is nearly vertical, as expected from the relatively low difference in entropy, but the double / single monopole crystal boundary should be steeper, again because of the erroneous value of the double monopole crystal entropy. From all this discussion, we conclude that our approximation of the free energy

should be most satisfactory when computed as far as possible from a phase boundary.

We believe our approach could be extended to include the last dimension of fragmentation: the harmonic field and the overall macroscopic magnetization. Because the bi-tetrahedra unit cell breaks the symmetry along a [111] cubic symmetry it could indeed be used to include the effect of the magnetic field along this direction. This would require introducing the [111] magnetization as a new order parameter, and further decomposing the 128 bi-tetrahedron states in the entropy according to which magnetization they have. This will remain outside the scope of this work.

5.2.4 Computation of observables when moving through the phase diagram

Keeping in mind this limitation, we would like to add some experimental relevance to our model by computing the two observables we will study under pressure, namely the specific heat and the density of crystallized monopoles. We want to simulate how they will change with parameters $(\bar{\nu}), \bar{\Delta}$ modified under pressure. The chemical potential $\bar{\nu}$ represent the order of magnitude of the interactions in the system. So if it increases, we can expect the peak of the specific heat, as well as the temperature below which the ordered moment arises, to increase accordingly. Here we want to investigate another effect: how do the observables of a fragmented phase change when $\bar{\Delta}$ is modified at fixed $\bar{\nu}$ and the system changes phases. We will start deep within the monopole crystal phase at $\bar{\nu} = 1.2, \bar{\Delta} = 1.0$ and decrease $\bar{\Delta}$ to go towards the spin ice phase. In order to avoid numerical problems we will not run the calculation close to the phase boundaries.

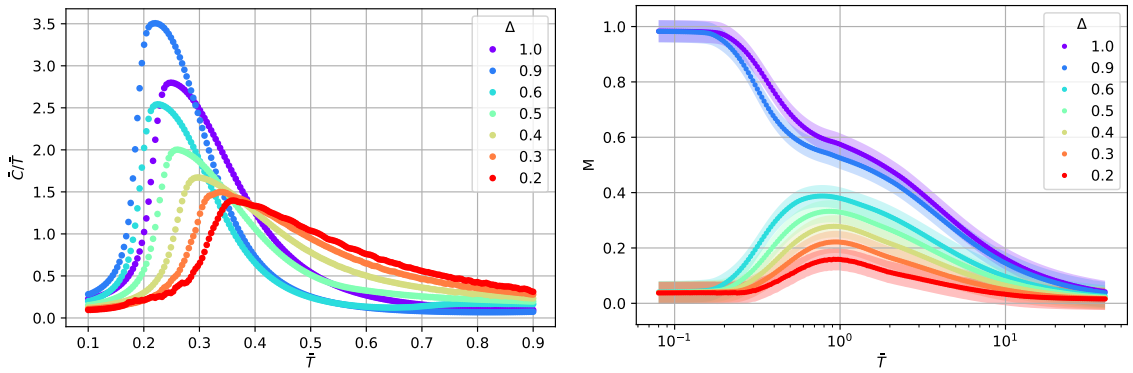

Figure 5.2.2: (left) $\bar{C}/\bar{T}$ and (right) density of crystallized monopoles as a function of temperature, for various $\bar{\Delta}$ at $\bar{\nu} = 1.2$. For $\bar{\Delta} > 0.75$ (< 0.75) the system is in the monopole crystal phase (in the spin ice phase respectively)

The specific heat is calculated from the equilibrium entropy with $\bar{C}/\bar{T} = \partial\bar{S}/\partial\bar{T}$. As the phase boundaries for $\bar{\Delta} \neq 0$ are nearly vertical, no phase transitions appear when doing temperature sweeps. Instead we find a broad bump corresponding to the proliferation of defects. But it can also be affected by the presence of a phase boundary even at an inaccessibly low temperature, as shown in Figure 5.2.2 (left). On this graph we plot $\bar{C}/\bar{T}$ as a function of temperature, for a

fixed $\bar{\nu} = 1.2$ and various $\bar{\Delta}$. As $\bar{\Delta}$ gets below ≈ 0.75 the system transitions from a monopole crystal to a spin ice, and the change of ground state can be spotted in two ways. First, the value of the maximum of $\bar{C}/\bar{T}$ (and overall area under the curves) diminishes, because the spin ice phase has a higher residual entropy. Second, the position of this maximum is greatly influenced by the critical point at much lower temperatures. The closer we probe to the critical $\bar{\Delta}$, the lower in temperature the maximum is; as $\bar{\Delta}$ is decreased far from the critical value the location of the maximum increases again.

In Figure 5.2.2 (right) we plot the density of crystallized monopoles $\rho_1\phi_1 + 2\rho_2\phi_2$ which we chose as an order parameter. This quantity is proportional to the ordered all-in / all-out moment (of the Γ_3 representation). The graph shows a sudden change in the zero temperature value which defines a phase change. But even at temperatures an order of magnitude higher than the critical point, ($\bar{T} > 3$) we can see that the ordered moment is slightly suppressed as the staggered chemical potential decreases. At the end of this chapter, we will present data from measurements of these two observables measured under pressure, which we will try to interpret

5.3 AC calorimetry at ambient pressure

Before discussing the more complex pressure experiments, we want to characterize the behavior of $Dy_2Ir_2O_7$ in an AC specific heat measurement. The measurement was performed at Institut Néel by Thierry Klein and Christophe Marcenat.

5.3.1 Experimental setup and thermal model

The specific heat is often measured with the goal of probing phase transitions, where they appear as sharp peaks. However as shown in the previous section, there are few possible phase transitions as a function of temperature in the case of fragmented spin ices, and so the entry into the spin ice or monopole crystal regimes is rather characterized by a broad feature. Therefore such materials require a more detailed thermal model than the simple Equation (2.2.5).

In Ref. [Michon, 2017], Bastien Michon validated a more refined model where the heater and thermometer are connected only by a finite internal thermal leak K_i. Furthermore, it also considers the possibility of a thermal decoupling of the sample itself: the sample assembly is divided into the addenda from the sample assembly and the actual sample. C_{add} and K_c are the addenda specific heat and the thermal leak to the sample respectively. Finally the assembly is connected to the thermal bath with a thermal leak K_e. This model is pictured in Figure 5.3.1. The authors solved the thermal model and found that the temperature oscillations at the thermometer do not involve the K_i thermal leak, and can be written in a simple form similar to the standard model:

$$T_{ac} = \frac{P_{AC}}{K_{eff} + 2j\omega C_{eff}} \tag{5.3.1}$$

which introduces *effective* heat capacity and thermal conductivity that are a mix of the true

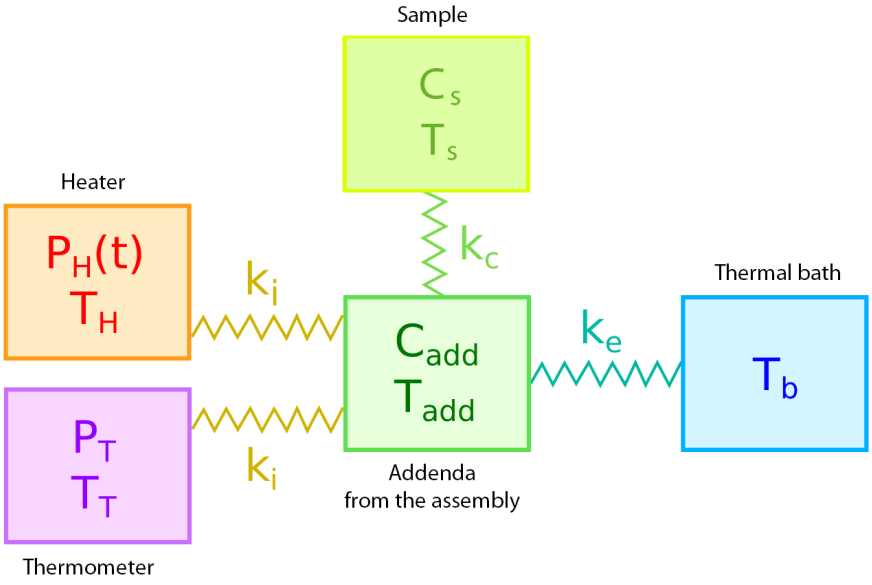

Figure 5.3.1: Thermal model used to describe the AC measurement and sample decoupling

specific heat of the sample C_s and K_c:

$$\begin{aligned} K_{eff} &= K_e + K_c(1-\beta(\omega)) \\ C_{eff} &= C_{\text{add}} + \beta(\omega) C_s \\ \text{with } \beta(\omega) &= \frac{1}{1+(2\omega C_s/K_c)^2} \end{aligned} \tag{5.3.2}$$

This model highlights the fact that above a certain frequency, the sample cannot be detected anymore because it becomes decoupled. However using a frequency too low results in more noise, as the optimal working point of the lock-in amplifier is to have ϕ around 45°, where ωC_{eff} and K_{eff} are of the same order of magnitude. However this model in itself cannot say where the decoupling originates from: it could come from the assembly compound having a small conductivity, or from the sample itself having a small conductivity or some slow degrees of freedom.

In the custom setup at Institut Néel, this experiment is connected to a ^{3}He sorption pump allowing to measure down to 300 mK. A magnetic field can be applied, and the entire setup can be rotated perpendicularly to the magnetic field. The sample is a cut of a single crystal of $Dy_2Ir_2O_7$to a size of about $150 \times 150 \times 30$ μm, originally used for the experiment under pressure. It is stuck to the experimental chip with a bit of Apiezon N grease. Its mass was too small to be measured directly with the scales available at the laboratory, and in the cutting process we also lost any information on the crystalline orientation.

5.3.2 Evidence of an intrinsic thermal decoupling in $Dy_2Ir_2O_7$

In Figure 5.3.2 we show the effective specific heat C_{eff} divided by temperature, extracted from the temperature oscillations with Equation (5.3.1). We measured its specific heat between 300 mK and 4 K, for fields of 0, 1 and 3 T and two frequencies for each field. We compare the AC measurements to one done at zero field in Ref. [Cathelin et al., 2020] with the relaxation method on the commercial PPMS instrument. By scaling the curves at zero field to match the PPMS measurement, the mass of our small crystal can be estimated to be about 5 μg. We observe that for all fields, the effective specific heat at a higher frequency is markedly lower than that at a lower frequency. This could be a sign of the decoupling discussed above.

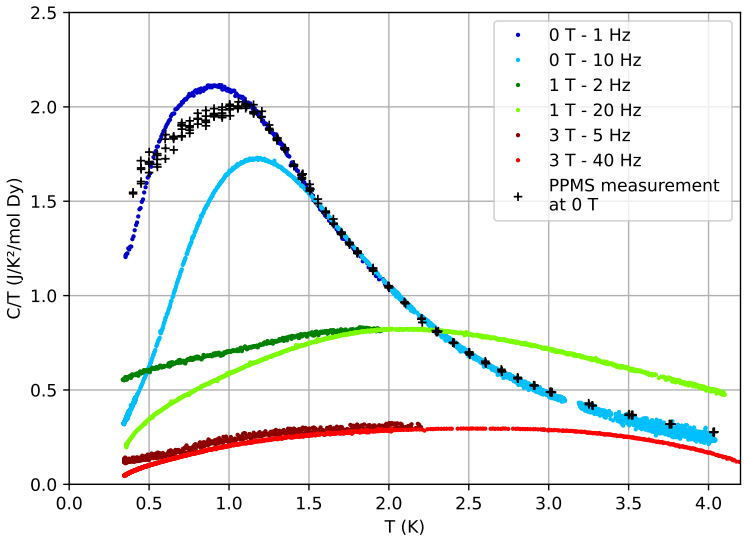

Figure 5.3.2: C_{eff}/T as a function of temperature, for three fields (blue: 0T, green: 1T and red: 3T) and two frequencies by field (dark or light hue). The black crosses corresponds to the data measured on another crystal on the PPMS.

To test this hypothesis, we performed measurements at zero field as a function of frequency at temperatures below 1 K, and measured the effective specific heat C_{eff} and thermal leak K_{eff}, shown in Figure 5.3.3 with the square points. We then fitted these measurements using the model in Equation (5.3.2), with a thermal leak to the sample K_c, and a sample specific heat C_s that do not depend on frequency. The square are the measurements and the dotted lines the best fit by the thermal model.

The agreement between the data points and the model means that we can make sense of the measurements by considering a thermal decoupling of the sample and introducing a finite thermalization time $\tau_c = C_s/K_c$ at each temperature. It is interesting to note that the PPMS measurement in Figure 5.3.2 deviates from the low frequency data at 0 T below $\approx 1.1K$, indicating that the sample may have decoupled in the PPMS measurement as well. However there are two possible physical origins to the decoupling:

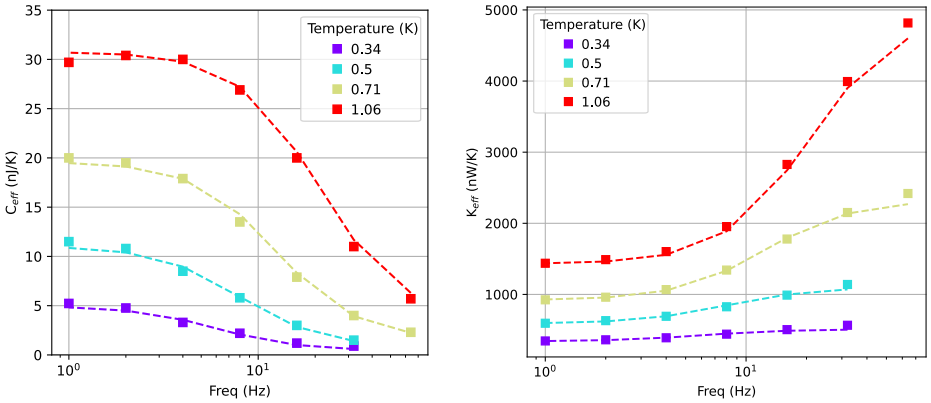

Figure 5.3.3: Effective specific heat (left) and thermal leak (right) at several temperatures at zero field. The squares are the measured data points and the dashed lines corresponds to the fit by the thermal model in Equation (5.3.2).

- The first one is the most common: below a certain temperature, the conductivity of the grease becomes too small compared to the specific heat of the sample and the entire sample decouples from the experimental apparatus;
- The second one depends on the sample's intrinsic relaxation times. If some degrees of freedom of the material become decoupled from other and have diverging relaxation time, the entire sample cannot be considered at thermal equilibrium above a certain frequency.

In order to find the correct scenario, we performed another experiment on the same sample with another material to ensure a better contact between the sample and the chip. We chose to use General Electric Varnish, thinned in ethanol in order to deposit a minimum amount on the sample. It has a thermal conductivity about 30 times that of Apiezon N grease at 1 K [Cryotronics, 2022], so we should expect a large increase in the thermal leak to the sample K_c. In Figure 5.3.4 we show the measurement of K_c estimated by fitting the model for both the measurements done with grease (in blue) or the varnish (in green). To get a point of comparison we plot the values of K_c obtained for a measurement of UTe_2 with grease. This material is a very good metal at low temperature and can be assumed to be intrinsically coupled to the experimental chip. The first observation is that our sample of $Dy_2Ir_2O_7$ is relatively badly coupled compared to UTe_2 below 1 K, with a thermal contact 3 times smaller at 300 mK. More importantly, this difference is not greatly reduced in the measurement done with GE varnish. This proves that the thermal decoupling comes from the sample and not the thermal contact by which it is connected to the experimental assembly.

5.3.3 Magnetic nature of the thermalization time

The intrinsic thermal decoupling could originate from the magnetic degrees of freedom, or from other material properties. In the case of a spin ice like pyrochlore, we can imagine a situation

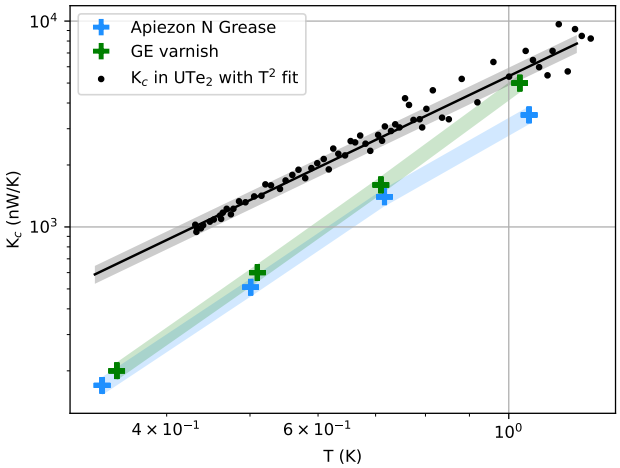

Figure 5.3.4: K_c estimated by the model as a function of temperature at zero field, for both the Apiezon N grease (blue) and GE varnish (green).

where the sample's lattice is still coupled, but the magnetic degrees of freedom, which make up the majority of the specific heat at these temperatures, cannot thermalize fast enough [Jaubert et al., 2011]. It has been shown that below about 700 mK, spin ice materials stay frozen into the same spin-ice configuration, with metastable pairs of monopoles called non-contractible pairs [Raban et al., 2019]. First of all, we notice in Figure 5.3.2 that the specific heat value at which the thermal decoupling is visible varies a function of the field; this would not be expected if the decoupling came from non-magnetic degrees of freedom.

To get a more precise answer, we have performed the same frequency measurements as in Figure 5.3.3 with fields of 1 and 3 T. We show the resulting decoupling time $\tau_c = C_s/K_c$ in Figure 5.3.5. As the field increases, the absolute specific heat, associated at these temperatures to the magnetic degrees of freedom, decreases as well. If the decoupling was caused by non-magnetic degrees of freedom, we would expect K_c to change as well in order to keep the decoupling time more or less constant as a function of the field. However this is not what we observe: τ_c decreases even more than the specific heat, providing stronger evidence that the decoupling is caused by the slow magnetic degrees of freedom.

For spin ice like pyrochlores, it has been shown that the magnetic properties, and especially the specific heat, are strongly anisotropic with regard to the direction of an applied field [Tabata et al., 2006; Ramirez et al., 1999; Yoshida et al., 2004]. This is due to the different magnetic states reached under different field directions as shown in Figure 1.1.8. So as a final experiment, we will study how the thermal leak to the sample K_c changes when rotating the sample perpendicularly to an applied field, which is possible in the setup. Unfortunately, the sample is not oriented due to its size and the way it was prepared. With applied field of 1 T, we found that the specific heat varied with a period of about 90°. Thus we chose to compare K_c between two angles where the absolute difference in specific heat is the largest; this amounts to a 45° rotation

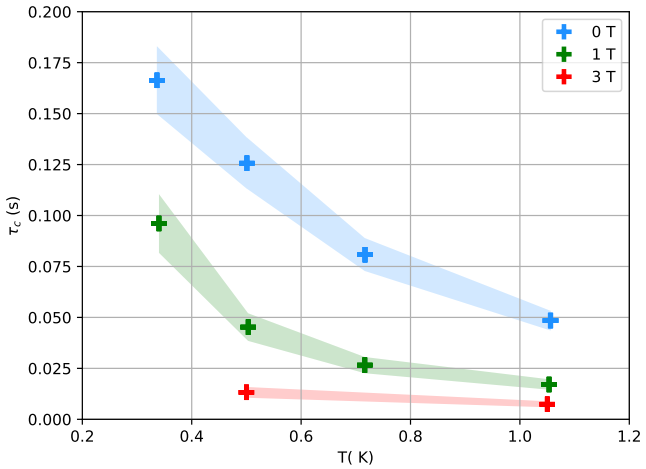

Figure 5.3.5: Decoupling time τ_c as a function of temperature, for various fields. The shaded areas correspond to the relative uncertainty in the fit of the model.

perpendicular to the field. The result is shown in Figure 5.3.6. We observe that K_c varies as much when rotating the sample relative to the field as when changing the assembly compound. This indicates that the thermal leak to the sample is influenced in part by the orientation relative to a magnetic field.

To conclude, we have demonstrated that in $Dy_2Ir_2O_7$ below 1 K the slow dynamics of the magnetic degrees of freedom lead to a partial thermal decoupling of the sample in AC specific heat measurement. This result should have a precautionary use as a reminder to choose the slowest available frequency or longest relaxation time when measuring the specific heat of fragmented spin ice compounds, but is also interesting in itself. Indeed it is a indirect signature that in these materials the magnetic excitations participate significantly to the thermal conductivity, and that as the temperature is lowered the magnetic relaxation times diverge and it becomes difficult to fully thermalise the sample.

This picture is consistent with direct measurements of the thermal conductivity on spin ice materials. In Refs [Toews et al., 2013] the authors measure the thermal conductivity of a thin single crystal of $Ho_2Ti_2O_7$grown along $\langle 111 \rangle$, under a field applied in the same direction. They measure the phononic conductivity by applying a strong magnetic field (> 6 T) which polarizes the system into an 3 in / 1 out state. They then compare the high-field values to the zero-field one. They find that monopoles excitations are responsible for an increase in thermal conductivity below 0.6 K, where they are in low enough number. But as their number grows they provide a significant scattering mechanism for the phonons and so decrease the conductivity compared to the high-field value. Interestingly, under application of a moderate field (< 0.5 T) so that the system is in the kagome ice phase, the first effect disappears but the second remains. This can be explained by the fact that in this state monopoles are confined to the kagome planes perpendicular to $\langle 111 \rangle$, and therefore do not contribute themselves to the thermal conductivity, but can

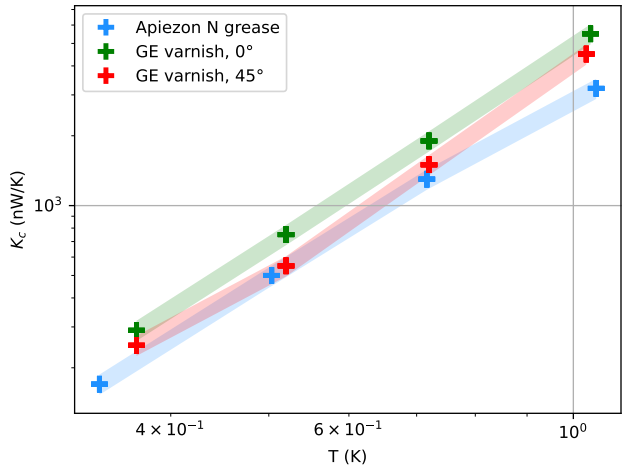

Figure 5.3.6: K_c estimated by the model as a function of temperature with an applied field of 1 T, for both the Apiezon N grease (blue) and two angles for the GE varnish (green and red).

still scatter the phonons. In Refs [Kolland et al., 2012; Kolland et al., 2013; Klemke et al., 2011] the authors performed similar experiments on $Dy_2Ti_2O_7$ and observed evidence of monopole heat transport. Such results support the continuation of the AC specific heat measurements presented in this section on $Ho_2Ti_2O_7$ or $Dy_2Ti_2O_7$ samples. Indeed in these compounds the thermal decoupling caused by the freezing of the magnetic degrees of freedom is expected to be larger because of the lower thermal conductivity compared to $Dy_2Ir_2O_7$.

5.4 Measurements of fragmented spin ices under pressure

In this final section we present our results for two measurements under pressure: specific heat for $Dy_2Ir_2O_7$ and neutron diffraction for $Ho_2Ir_2O_7$.

5.4.1 AC specific heat under pressure

The specific heat of $Dy_2Ir_2O_7$ under pressure was measured at CEA with Daniel Braithwaite. The experimental setup is composed of a helium bellows and levers, mounted at the end of a dilution cane, that can be loaded with diamond pressure cells going up to 10 GPa. The experimental assembly on the diamond table is shown in Figure 5.4.1 (left). The sample (which is the same as the one in the ambient pressure AC measurements presented before) is at the center, between a heater on top and a thermocouple on the bottom, assembled with a conductive silver lacquer. The thermometer is built from a resistive contact between two gold wires, and a gold wire and a $AuFe_{0.07\%}$ alloy wire are pressed together to form the hot junction of a thermocouple. The heater is a resistive contact between two gold wires with a small quantity of black Stycast epoxy. The gasket between the two diamonds is filled with argon that acts as a hydrostatic pres-

sure medium. The pressure is measured in situ by tracking the fluorescence line of a small piece of ruby placed in the cell.

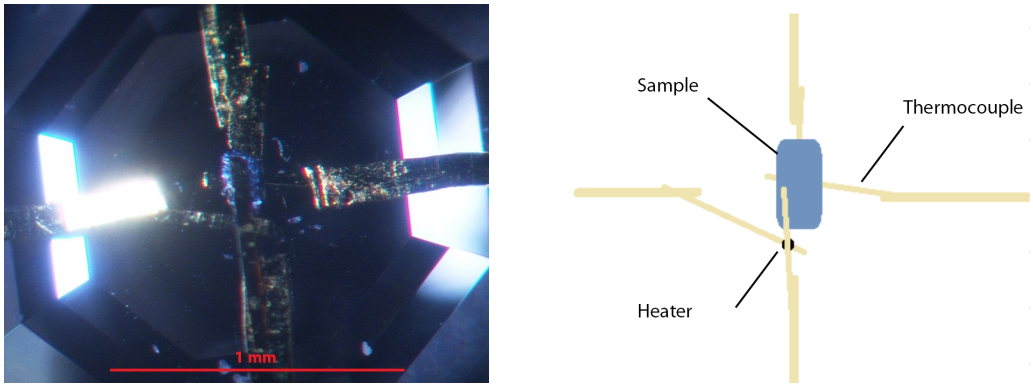

Figure 5.4.1: (left) Sample assembly on the diamond table. (right) Schematic view.

The thermal model of such an experiment is expected to be different from the one in Equations (5.3.1) and (5.3.2) [Méasson, 2005]. Namely, there is a direct thermal contact between the thermal bath, the heater and thermocouple. Additionally, the various thermal losses cannot be characterized beforehand as they will change with every experimental assembly. At low frequency, the signal is very low because of the more important losses to the environment; while at high frequency the signal is very low because the sample becomes decoupled. An important assumption is the that the losses to the environment should not depend significantly on the pressure. This makes it possible to choose one frequency of temperature oscillations for the whole experiment, chosen by searching for the maximum in the frequency response. We chose a value of 277 Hz. This frequency is rather high considering the sample's intrinsic relaxation times shown in Figure 5.3.5. This pressure experiment was realized first, before having the evidence for a decoupling in AC calorimetry at ambient pressure. However, it would not have been possible to measure with a frequency of a few Hz in the pressure experiment due to the large losses to the environment.

Similarly, the amplitude of the oscillations is tuned so that the sample is able to thermalize at low temperatures, while still having a workable signal over noise ratio. We used a signal to the heater of amplitude 0.11 V. The resistance of the heater can be measured in real time, in order to normalize the temperature oscillations by the power sent. The signal is sent to several preamplifiers, then the temperature oscillations and the phase difference relative to the square of the applied voltage is measured with a lock-in amplifier. Unfortunately this means that we do not know the value of the phase difference in situ.

The temperature oscillations per unit of power and the raw phase difference at zero field are represented on figure 5.4.2. To compute an effective specific heat, one must interpret the data relative to a particular thermal model. In this regard, the raw values of the phase difference make little sense. They are influenced by a variety of parameters, including the nature of the amplifiers. First, we assume that the phase at all pressures must have the same small value at 5 K. This is where the sample specific heat C_s should be low and where the losses to the envi-

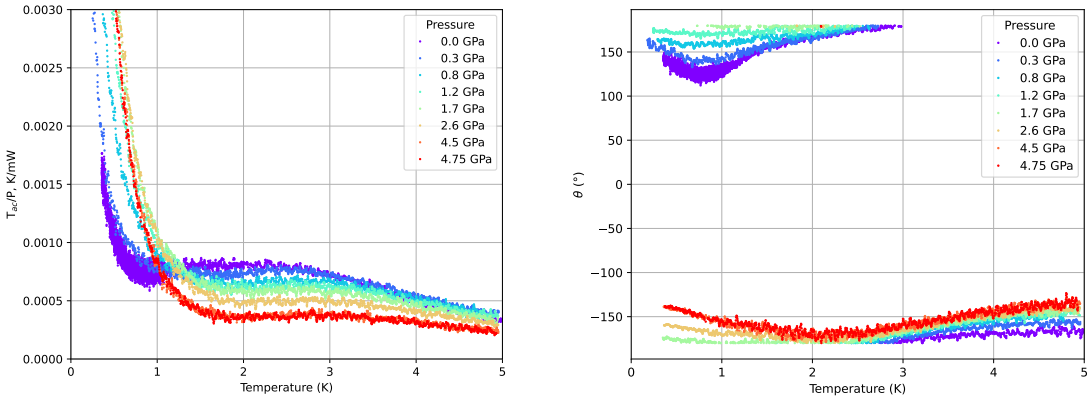

Figure 5.4.2: (left) Amplitude of temperature oscillations per unit of power and (right) Raw phase difference at zero field

ronment will be high. Therefore the ratio C_s/K representing the thermalization time should be the smallest. The general shape of the phase curves can therefore be explained as follow:

- Below 1 K, the sample's specific heat is low, and at the frequency of 277 Hz we use to measure, its magnetic degrees of freedom most likely out of equilibrium. The losses to the environment are comparatively high, so we expect the phase difference to decrease in absolute value as the temperature is decreased.
- Between about 1 and 2 K, the sample is coupled well because its specific heat is bigger than the thermal leak, and so the phase difference has a maximum in absolute value;
- Above 2 K, the sample becomes decoupled because its specific heat decreases as the thermal conductivity of the leak increases, and so the phase decreases in absolute value as well.

We also performed measurements under a 4 T field, but have not been able to analyze it in the same way. The corresponding temperature oscillations and raw phase difference are shown on figure 5.4.3.

As such we focus on the zero field measurement, which we will try to compare to the low frequency measurement made on the same sample. We chose to shift all the phases curves to a common reference at 5 K, then use the simple Equation (2.2.5) to compute the specific heat. The best agreement with the ambient pressure data was found with a reference of $-15°$. The corresponding phase differences and C/T data are shown in Figure 5.4.4. We notice that 0 and 0.3 GPa below 1.3 K, the effective C/T computed this way is significantly larger than the ambient pressure reference shown in black. In addition, the 0 GPa data has a strange frequency shift between 1.5 and 4 K that disappeared as soon as a small pressure was applied. Hence we believe that the 0 GPa data is spurious, as the sample was probably not well stuck to the experimental assembly. With respect to the large values measured at low temperature, we think that they

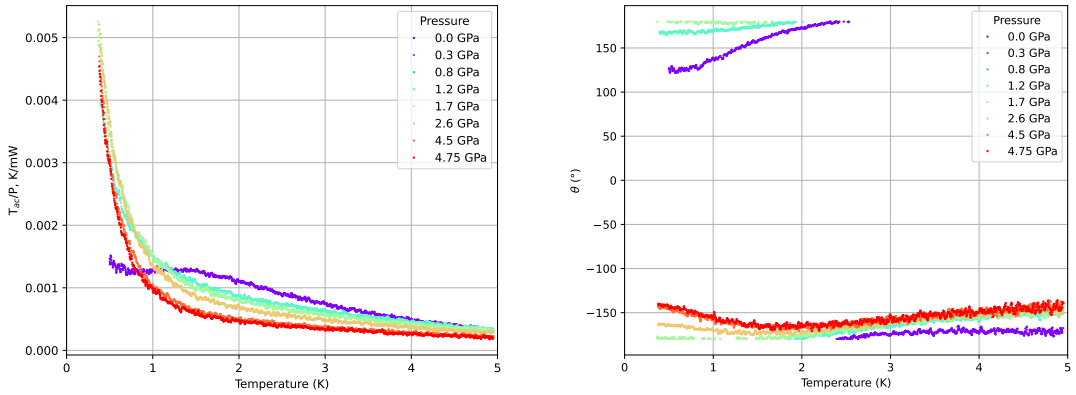

Figure 5.4.3: (left) Amplitude of temperature oscillations per unit of power and (right) Raw phase difference at 4 T

may be an artefact of the simple thermal model we have used. For example, it is possible that at these temperatures the detected temperature oscillations are not from the sample but from part of pressure medium itself, leading to an overestimated contribution [Méasson, 2005].

Therefore, we focus on temperatures above about 1.3 K. Our data analysis suggests that the pressure decreases the specific heat, and moves its peak to higher temperatures. Consequently, the magnetic entropy released on heating seems to decrease. This is similar to the case we have investigated with our mean-field computation in Figure 5.2.2 (left), where the staggered chemical potential decreases at fixed $\bar{\nu}$. Our measurement could be a signature of a change of phase from a monopole crystal to a spin ice phase under pressure, but remains a preliminary result. New measurements of the specific heat under pressure with a better choice of frequency would be needed to draw a more definitive conclusion.

5.4.2 Neutron diffraction under pressure on $Ho_2Ir_2O_7$

We performed neutron diffraction under pressure on the D20 instrument at ILL. About 50 mg of $Ho_2Ir_2O_7$ powder was mounted into a boron nitride anvils pressure cell, capable of pressures up to 10 GPa. The pressure medium is a 4 : 1 mix of methanol and ethanol. The pressure cell is in a standard ^{4}He cryostat and can go down to 5 K. The pressure is measured in situ with a small piece of lead added to the sample, whose lattice parameter is calibrated as a function of pressure. The experiment was done in collaboration with Sylvain Petit and ran by Thomas Hansen.

$Ho_2Ir_2O_7$ has an all-in / all-out ordered moment, belonging to the Γ_3 representation. At ambient pressure, it starts to appear below 20 K and saturates below 3 K at about 5 μ_B, half of the single-ion Ho moment [Lefrançois et al., 2017]. In our experiment, we could not go below 17 K at ambient pressure due to a temperature regulation issue. In Figure 5.4.5 (left) we show the diffraction spectra at 5 K for three pressures: 4, 8 and 10 GPa with 3 hours of counting time. They exhibits three peaks: (220), (311) and (222) of which the first two are magnetic and the last

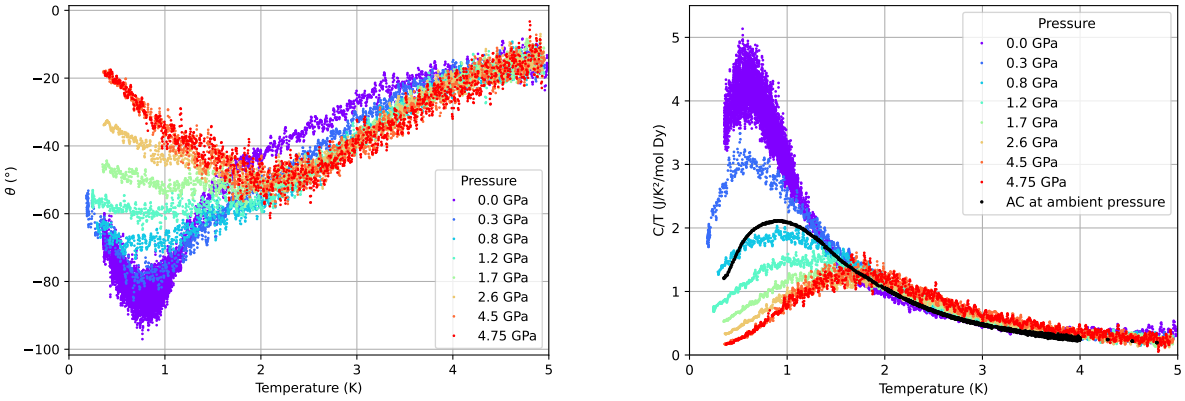

Figure 5.4.4: (left) Phase differences as a function of temperature for various pressures, offset so that they all are at -15° at 5 K. (right) Effective C/T using the adjusted phase differences. The data was scaled to match as well as possible with the lowest frequency data discussed in the previous section, shown in black.

one is only nuclear in this representation. We have offset the spectra to match the background but, we see that the signal from the sample is overall lower as the pressure is increased. This caused by the sample volume decreasing and the environment background signal increasing with pressure. We have also measured at higher temperatures of 7, 10, 15 K but for a shorter duration because of time constraints.

In order to extract the value of the ordered moment, we have used two methods. On our side, we have fitted the signal with a Rietveld refinement using the FullProf Program. Sylvain Petit computed the differences of the spectra with a reference signal measured at 80 K. He then fitted the remaining magnetic peaks manually, comparing their amplitude with that of the nuclear peaks, to get a value of the moment. In Figure 5.4.5 (right) we show the results of the two analysis methods. The two methods are in agreement at the lowest temperature of 5 K where we had the best statistics. For the intermediate temperatures, which were noisier because of a shorter counting time, the FullProf refinement tends to overestimate the ordered moment. The differences method seems the most sensible, especially for the 10 GPa data. The ordered moment we measured at ambient pressure at 17 K was in agreement with the literature [Lefrançois et al., 2017].

Similarly to the case of $Dy_2Ir_2O_7$ under pressure, these measurements seem to show that the pressure suppresses the fragmented monopole crystal phase and pushes the system towards the spin ice phase, with a smaller ordered moment; however this result remains preliminary. In order to give a more definitive answer, we have a new diffraction experiment planned on D20 at ILL at the time of writing. It will use diamond anvils pressure cells which should be able to go to 20 GPa, with a longer beam time.

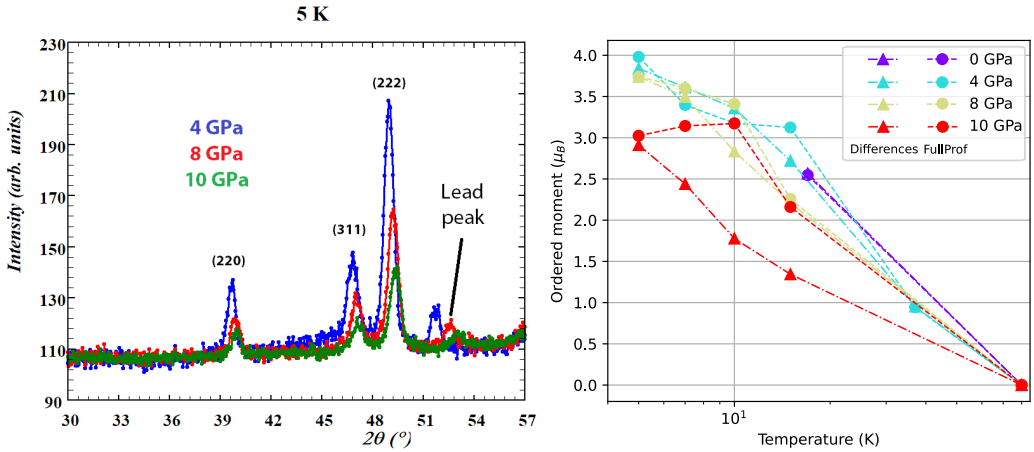

Figure 5.4.5: (left) Diffraction spectra under pressure focused on the two lowest angle magnetic peaks ((220) and (311)). (right) Ordered moment as a function of temperature for all pressures, obtained with two different methods discussed in the text.

5.5 Conclusions

In this chapter, our goal was to explore the fragmentation phase diagram from both a theoretical and experimental point of view. We have produced an extension of a mean-field theory of fragmentation centered around a combinatoric computation of the entropy for a set of two adjacent tetrahedra. This allowed us to numerically minimize the grand potential for the entire fragmentation phase diagram and obtain the qualitative features only seen in Monte-Carlo simulations up to now. Since the actual phase transitions are located at very low temperatures (about 400 mK), we have focused on the signatures of a phase change in experiments that could appear at higher temperatures. We computed the specific heat and ordered moments as a function of temperature, and showed that a ground state change can be seen qualitatively at temperatures of a few Kelvins.

The measurement of specific heat under pressure is done with an AC method which had not been used before on spin ice like materials. We have characterized the behavior of $Dy_2Ir_2O_7$ in this type of experiment and shown that the choice of frequency is crucial to get an accurate measurement. Due to the large magnetic relaxation times at low temperature, the sample can be effectively decoupled from the measurement even with a perfect thermal contact with the chip. This effect is an indirect signature of the fact that magnetic excitations participate to the thermal conductivity in spin ice materials.

Finally, we have performed challenging measurements of the specific heat and ordered moment under pressure, on $Dy_2Ir_2O_7$ and $Ho_2Ir_2O_7$ respectively. In both cases, the complexity inherent to pressure experiments prevented us from drawing strong conclusions. Nevertheless, the preliminary results seem to point towards the same physics: the application of pressure seems to suppress the partially ordered fragmented phase and push towards a less ordered spin ice state. This motivates further experiments under pressure, like the measurement of the

AC susceptibility which can be performed at dilution temperatures at CEA-Pheliqs.

General conclusion

This thesis has been centered around the concept of magnetic fragmentation, its theoretical consequences and its experimental signatures. It is still a relatively new concept in the field of frustrated magnetism and we have strived to show its merits in analyzing data, shining a new light on known magnetic structures and testing paradigms of statistical mechanics. Here we want to provide some perspectives for further investigations.

In Chapter 3 we have applied the fragmentation formalism to the analysis of neutrons scattering data. It allows for a straightforward mapping as each fragment of the decomposition gives a separate contribution to the neutron scattering intensity. We have used this understanding to design a measurable order parameter in the case of a transition between two ground states of quantum kagome ice. But the low energy scales associated with quantum spin ice have so far made identification of experimental systems extremely difficult. One promising example is $Pr_2Hf_2O_7$ [Sibille et al., 2018] which shows some evidence of a quantum spin liquid ground state from inelastic neutron scattering of single crystal samples. Experiments in a [111] field could be of interest in the quest to observe the two-dimensional quantum phases predicted in Ref. [Bojesen et al., 2017] and discussed in detail above. The stacked kagomé layer material $Ho_3Mg_2Sb_3O_{14}$ also appears to show quantum corrections to a classical fragmented magnetic structure closely related to the KII phase of kagomé ice [Dun et al., 2020], although for the moment only powder samples exist and the synthesis of pure samples appears challenging. Extending our analysis to the case of a powder would be of interest, as the signal from the quantum spin$-P$ phase would be distinct from the alternative quantum phases predicted by Dun *et. al.*. From a more general point of view, our work motivates a classification of fragmented phases and their respective experimental signatures.

In Chapter 4, we have performed a detailed study of the $Ho_2Ru_2O_7$ pyrochlore. Our measurements of the specific heat and ordered moment are in agreement to propose that the ground state of this compound is fragmented in a new way. The ordered fragment is ferromagnetic, contrary to the antiferromagnetic partial moment in pyrochlore iridates. Futhermore, AC susceptibility measurements showed the existence of two modes with separate relaxation times, which coexist at the transition. We do not know yet if these two modes can be associated with different kinds of magnetic correlations in the system, and further neutron diffraction and inelastic scattering at dilution temperatures are planned. The search for exotic fragmentation in Ising pyrochlores could turn its focus toward other materials like $Dy_2Ru_2O_7$ or $Nd_2Ru_2O_7$ [Rams et al., 2011; Ku et al., 2018] to see if some experimental results are better taken into account in a fragmentation picture. Moreover, there exists other pyrochlore oxides where the B-site is occupied by a magnetic atom, like the molybdenate pyrochlores, which have not been studied at low temperatures [Gardner et al., 2010].

In Chapter 5 we have combined theory and experiments to explore the existing phase diagram of fragmentation with pressure. We have managed to write an extension of a mean field theory taking into account the entropy of the fragmented phase and the double monopoles, and made use of it to compute observables at different points of the phase diagram. We then measured the ordered moment of $Ho_2Ir_2O_7$ and the specific heat of $Dy_2Ir_2O_7$ under pressure, which were both challenging to analyze but pointed towards a suppression of the fragmented phase under pressure, possibly crossing into the spin ice regime. In order to better understand the behavior of $Dy_2Ir_2O_7$ in an AC specific heat measurement, we performed an additional experiment at ambient pressure. It showed that this compound can become intrinsically out of equilibrium above a certain frequency because the magnetic relaxation times are large. This warrants new experiments at a lower measuring frequency for $Dy_2Ir_2O_7$ and going to higher pressures for $Ho_2Ir_2O_7$. However, we believe that the best candidate material to see the evolution of fragmentation under pressure is $Ho_2Ru_2O_7$, as its sharp transition at 1.55 K would be much easier to track in specific heat or susceptibility measurements.

Bibliography

Arnold, O. et al. (Nov. 11, 2014). Mantid—Data Analysis and Visualization Package for Neutron Scattering and μ SR Experiments. In: *Nuclear Instruments and Methods in Physics Research Section A: Accelerators, Spectrometers, Detectors and Associated Equipment* 764, pp. 156–166. ISSN: 0168-9002. DOI: 10.1016/j.nima.2014.07.029.

Bansal, C. et al. (Aug. 5, 2002). Structure and Magnetic Properties of the Pyrochlore Ho 2 Ru 2 O 7 : A Possible Dipolar Spin Ice System. In: *Physical Review B* 66.5, p. 052406. ISSN: 0163-1829, 1095-3795. DOI: 10.1103/PhysRevB.66.052406.

Bègue, Frédéric (2012). "Gauge Mean Field Theory in a Highly Frustrated Ferromagnet". MSc Thesis. ENS de Lyon.

Benton, Owen, Olga Sikora, and Nic Shannon (Aug. 30, 2012). Seeing the Light : Experimental Signatures of Emergent Electromagnetism in a Quantum Spin Ice. In: *Physical Review B* 86.7, p. 075154. ISSN: 1098-0121, 1550-235X. DOI: 10.1103/PhysRevB.86.075154. arXiv: 1204.1325.

Bergman, Doron L., Gregory A. Fiete, and Leon Balents (Apr. 3, 2006). Ordering in a Frustrated Pyrochlore Antiferromagnet Proximate to a Spin Liquid. In: *Physical Review B* 73.13. ISSN: 1098-0121, 1550-235X. DOI: 10.1103/PhysRevB.73.134402.

Bergman, Doron L. et al. (Mar. 2, 2007a). Degenerate Perturbation Theory of Quantum Fluctuations in a Pyrochlore Antiferromagnet. In: *Physical Review B* 75.9, p. 094403. ISSN: 1098-0121, 1550-235X. DOI: 10.1103/PhysRevB.75.094403. arXiv: cond-mat/0607210.

– (Apr. 11, 2007b). Effective Hamiltonians for Some Highly Frustrated Magnets. In: *Journal of Physics: Condensed Matter* 19.14, p. 145204. ISSN: 0953-8984, 1361-648X. DOI: 10.1088/0953-8984/19/14/145204. arXiv: cond-mat/0608131.

Bojesen, Troels Arnfred and Shigeki Onoda (Nov. 29, 2017). Quantum Spin Ice under a [111] Magnetic Field: From Pyrochlore to Kagome. In: *Physical Review Letters* 119.22, p. 227204. ISSN: 0031-9007, 1079-7114. DOI: 10.1103/PhysRevLett.119.227204.

Bramwell, S T et al. (Jan. 31, 2000). Bulk Magnetization of the Heavy Rare Earth Titanate Pyrochlores - a Series of Model Frustrated Magnets. In: *Journal of Physics: Condensed Matter* 12.4, pp. 483–495. ISSN: 0953-8984, 1361-648X. DOI: 10.1088/0953-8984/12/4/308.

Bramwell, S. T. et al. (July 10, 2001). Spin Correlations in Ho 2 Ti 2 O 7 : A Dipolar Spin Ice System. In: *Physical Review Letters* 87.4, p. 047205. ISSN: 0031-9007, 1079-7114. DOI: 10.1103/PhysRevLett.87.047205.

Brooks-Bartlett, M. E. et al. (Jan. 24, 2014). Magnetic-Moment Fragmentation and Monopole Crystallization. In: *Physical Review X* 4.1, p. 011007. ISSN: 2160-3308. DOI: 10.1103/PhysRevX.4.011007.

Canals, Benjamin et al. (Sept. 2016). Fragmentation of Magnetism in Artificial Kagome Dipolar Spin Ice. In: *Nature Communications* 7.1. ISSN: 2041-1723. DOI: 10.1038/ncomms11446.

Castelnovo, Claudio, Roderich Moessner, and Shivaji L. Sondhi (Jan. 2008). Magnetic Monopoles in Spin Ice. In: *Nature* 451.7174, pp. 42–45. ISSN: 0028-0836, 1476-4687. DOI: 10.1038/nature06433. arXiv: 0710.5515.

Cathelin, V. et al. (Sept. 29, 2020). Fragmented Monopole Crystal, Dimer Entropy, and Coulomb Interactions in Dy 2 Ir 2 O 7. In: *Physical Review Research* 2.3, p. 032073. ISSN: 2643-1564. DOI: 10.1103/PhysRevResearch.2.032073.

Chern, Gia-Wei, Paula Mellado, and O. Tchernyshyov (May 20, 2011). Two-Stage Ordering of Spins in Dipolar Spin Ice on the Kagome Lattice. In: *Physical Review Letters* 106.20, p. 207202. ISSN: 0031-9007, 1079-7114. DOI: 10.1103/PhysRevLett.106.207202.

Cryotronics, Lake Shore (2022). *LSTC_epoxygv_l.Pdf*. URL: https://indico.fnal.gov/event/11540/contributions/8781/attachments/5872/7606/LSTC_epoxygv_l.pdf (visited on 12/06/2022).

Dubovik, V. M. and V. V. Tugushev (Mar. 1, 1990). Toroid Moments in Electrodynamics and Solid-State Physics. In: *Physics Reports* 187.4, pp. 145–202. ISSN: 0370-1573. DOI: 10.1016/0370-1573(90)90042-Z.

Dun, Zhiling et al. (Sept. 29, 2020). Quantum Versus Classical Spin Fragmentation in Dipolar Kagome Ice Ho 3 Mg 2 Sb 3 O 14. In: *Physical Review X* 10.3, p. 031069. ISSN: 2160-3308. DOI: 10.1103/PhysRevX.10.031069.

Fennell, T. et al. (Oct. 16, 2009). Magnetic Coulomb Phase in the Spin Ice Ho2Ti2O7. In: *Science* 326.5951, pp. 415–417. ISSN: 0036-8075, 1095-9203. DOI: 10.1126/science.1177582.

Gardner, J S et al. (Nov. 9, 2005). Spin Dynamics in $Ho_2Ru_2O_7$. In: *Journal of Physics: Condensed Matter* 17.44, pp. 7089–7095. ISSN: 0953-8984, 1361-648X. DOI: 10.1088/0953-8984/17/44/002.

Gardner, Jason S., Michel J. P. Gingras, and John E. Greedan (Jan. 26, 2010). Magnetic Pyrochlore Oxides. In: *Reviews of Modern Physics* 82.1, pp. 53–107. ISSN: 0034-6861, 1539-0756. DOI: 10.1103/RevModPhys.82.53.

Gaulin, B. D. et al. (Oct. 3, 2011). Lack of Evidence for a Singlet Crystal-Field Ground State in the Magnetic Pyrochlore Tb 2 Ti 2 O 7. In: *Physical Review B* 84.14, p. 140402. ISSN: 1098-0121, 1550-235X. DOI: 10.1103/PhysRevB.84.140402.

Gingras, M J P and P A McClarty (May 1, 2014). Quantum Spin Ice: A Search for Gapless Quantum Spin Liquids in Pyrochlore Magnets. In: *Reports on Progress in Physics* 77.5, p. 056501. ISSN: 0034-4885, 1361-6633. DOI: 10.1088/0034-4885/77/5/056501.

Gingras, Michel J. P. and Byron C. den Hertog (Dec. 14, 2000). Origin of Spin Ice Behavior in Ising Pyrochlore Magnets with Long Range Dipole Interactions: An Insight from Mean-Field Theory. In: *ArXivcond-Mat0012275*. DOI: 10.1139/cjp-79-11-12-1339. arXiv: cond-mat/0012275.

Goswami, Pallab, Bitan Roy, and Sankar Das Sarma (Feb. 16, 2017). Competing Orders and Topology in the Global Phase Diagram of Pyrochlore Iridates. In: *Physical Review B* 95.8, p. 085120. ISSN: 2469-9950, 2469-9969. DOI: 10.1103/PhysRevB.95.085120.

Gray, Callum, Steven T Bramwell, and Peter C W Holdsworth (Sept. 1, 2021). Electric Field Fluctuations in the Two-Dimensional Coulomb Fluid. In: *New Journal of Physics* 23.9, p. 093039. ISSN: 1367-2630. DOI: 10.1088/1367-2630/ac0c52.

Guruciaga, P. C., S. A. Grigera, and R. A. Borzi (Nov. 21, 2014). Monopole Ordered Phases in Dipolar and Nearest-Neighbors Ising Pyrochlore: From Spin Ice to the All-in–All-out Antiferromagnet. In: *Physical Review B* 90.18, p. 184423. ISSN: 1098-0121, 1550-235X. DOI: 10.1103/PhysRevB.90.184423.

Hamp, James et al. (Aug. 28, 2015). Emergent Coulombic Criticality and Kibble-Zurek Scaling in a Topological Magnet. In: *Physical Review B* 92.7, p. 075142. ISSN: 1098-0121, 1550-235X. DOI: 10.1103/PhysRevB.92.075142. arXiv: 1506.03472 [cond-mat].

Hao, Zhihao, Alexandre G. R. Day, and Michel J. P. Gingras (Dec. 18, 2014). Bosonic Many-Body Theory of Quantum Spin Ice. In: *Physical Review B* 90.21. ISSN: 1098-0121, 1550-235X. DOI: 10.1103/PhysRevB.90.214430.

Harris, M. J. et al. (Sept. 29, 1997). Geometrical Frustration in the Ferromagnetic Pyrochlore Ho 2 Ti 2 O 7. In: *Physical Review Letters* 79.13, pp. 2554–2557. ISSN: 0031-9007, 1079-7114. DOI: 10.1103/PhysRevLett.79.2554.

Henelius, P. et al. (Jan. 7, 2016). Refrustration and Competing Orders in the Prototypical Dy 2 Ti 2 O 7 Spin Ice Material. In: *Physical Review B* 93.2. ISSN: 2469-9950, 2469-9969. DOI: 10.1103/PhysRevB.93.024402.

Henley, Christopher L. (Aug. 10, 2010). The "Coulomb Phase" in Frustrated Systems. In: *Annual Review of Condensed Matter Physics* 1.1, pp. 179–210. ISSN: 1947-5454, 1947-5462. DOI: 10.1146/annurev-conmatphys-070909-104138. arXiv: 0912.4531.

Hermele, Michael, Matthew P. A. Fisher, and Leon Balents (Feb. 12, 2004). Pyrochlore Photons: The U (1) Spin Liquid in a S = 1 2 Three-Dimensional Frustrated Magnet. In: *Physical Review B* 69.6. ISSN: 1098-0121, 1550-235X. DOI: 10.1103/PhysRevB.69.064404.

Huse, David A. et al. (Oct. 16, 2003). Coulomb and Liquid Dimer Models in Three Dimensions. In: *Physical Review Letters* 91.16. ISSN: 0031-9007, 1079-7114. DOI: 10.1103/PhysRevLett.91.167004.

Isakov, S. V. et al. (Oct. 14, 2004). Dipolar Spin Correlations in Classical Pyrochlore Magnets. In: *Physical Review Letters* 93.16. ISSN: 0031-9007, 1079-7114. DOI: 10.1103/PhysRevLett.93.167204.

Jaubert, L D C and P C W Holdsworth (Apr. 27, 2011). Magnetic Monopole Dynamics in Spin Ice. In: *Journal of Physics: Condensed Matter* 23.16, p. 164222. ISSN: 0953-8984, 1361-648X. DOI: 10.1088/0953-8984/23/16/164222.

Jaubert, L. D. C. (June 2015). Monopole Holes in a Partially Ordered Spin Liquid. In: *SPIN* 05.02, p. 1540005. ISSN: 2010-3247, 2010-3255. DOI: 10.1142/S2010324715400056.

Jülich, Forschungszentrum (2007). *Neutron Scattering: Lectures of the JCNS Laboratory Course Held at Forschungszentrum Jülich and the Research Reactor FRM II of TU Munich*. Ed. by Thomas Brückel et al. Schriften Des Forschungszentrums Jülich Reihe Materie Und Material 38. Jülich: Forschungszentrum Jülich. ISBN: 978-3-89336-489-3.

Kaiser, Vojtěch et al. (Oct. 9, 2018). Emergent Electrochemistry in Spin Ice: Debye-Hückel Theory and Beyond. In: *Physical Review B* 98.14, p. 144413. ISSN: 2469-9950, 2469-9969. DOI: 10.1103/PhysRevB.98.144413. arXiv: 1803.04668.

Klemke, B. et al. (June 2011). Thermal Relaxation and Heat Transport in the Spin Ice Material Dy2Ti2O7. In: *Journal of Low Temperature Physics* 163.5-6, pp. 345–369. ISSN: 0022-2291, 1573-7357. DOI: 10.1007/s10909-011-0348-y.

Kolland, G. et al. (Aug. 8, 2012). Thermal Conductivity and Specific Heat of the Spin-Ice Compound Dy$_2$Ti$_2$O$_7$: Experimental Evidence for Monopole Heat Transport. In: *Physical Review B* 86.6, p. 060402. ISSN: 1098-0121, 1550-235X. DOI: 10.1103/PhysRevB.86.060402. arXiv: 1205.5700.

Kolland, G. et al. (Aug. 9, 2013). Anisotropic Heat Transport via Monopoles in the Spin-Ice Compound Dy 2 Ti 2 O 7. In: *Physical Review B* 88.5, p. 054406. ISSN: 1098-0121, 1550-235X. DOI: 10.1103/PhysRevB.88.054406.

Ku, S T et al. (Apr. 18, 2018). Low Temperature Magnetic Properties of Nd $_2$ Ru $_2$ O $_7$. In: *Journal of Physics: Condensed Matter* 30.15, p. 155601. ISSN: 0953-8984, 1361-648X. DOI: 10.1088/1361-648X/aab398.

Ladovrechis, Konstantinos, Tobias Meng, and Bitan Roy (June 25, 2021). Competing Magnetic Orders and Multipolar Weyl Fermions in 227 Pyrochlore Iridates. In: *Physical Review B* 103.24, p. L241116. ISSN: 2469-9950, 2469-9969. DOI: 10.1103/PhysRevB.103.L241116.

Lara, D. Peña and J. A. Plascak (Aug. 10, 1998). The Critical Behavior of the General Spin Blume–Capel Model. In: *International Journal of Modern Physics B* 12.20, pp. 2045–2061. ISSN: 0217-9792, 1793-6578. DOI: 10.1142/S0217979298001198.

Lefrançois, E. (2016). "Synthèse de composés à base d'oxydes d'iridium à forte intrication spin-orbite". Université Grenoble Alpes.

Lefrançois, E. et al. (Dec. 2017). Fragmentation in Spin Ice from Magnetic Charge Injection. In: *Nature Communications* 8.1, p. 209. ISSN: 2041-1723. DOI: 10.1038/s41467-017-00277-1.

Lhotel, Elsa, Ludovic D. C. Jaubert, and Peter C. W. Holdsworth (Dec. 2020). Fragmentation in Frustrated Magnets: A Review. In: *Journal of Low Temperature Physics* 201.5-6, pp. 710–737. ISSN: 0022-2291, 1573-7357. DOI: 10.1007/s10909-020-02521-3.

Li, Fei-Ye and Gang Chen (July 5, 2018). Competing Phases and Topological Excitations of Spin-1 Pyrochlore Antiferromagnets. In: *Physical Review B* 98.4, p. 045109. ISSN: 2469-9950, 2469-9969. DOI: 10.1103/PhysRevB.98.045109.

Lounasmaa, O. V. (Nov. 1, 1962). Specific Heat of Holmium Metal between 0.38 and 4.2°K. In: *Physical Review* 128.3, pp. 1136–1139. ISSN: 0031-899X. DOI: 10.1103/PhysRev.128.1136.

Lv, Jian-Ping et al. (July 14, 2015). Coulomb Liquid Phases of Bosonic Cluster Mott Insulators on a Pyrochlore Lattice. In: *Physical Review Letters* 115.3, p. 037202. ISSN: 0031-9007, 1079-7114. DOI: 10.1103/PhysRevLett.115.037202. arXiv: 1502.04788.

Matsuhira, Kazuyuki et al. (Dec. 15, 2011). Spin Dynamics at Very Low Temperature in Spin Ice $Dy_2Ti_2O_7$. In: *Journal of the Physical Society of Japan* 80.12, p. 123711. ISSN: 0031-9015, 1347-4073. DOI: 10.1143/JPSJ.80.123711.

Méasson, Marie-Aude (Jan. 1, 2005). "La Skutterudite PrOs4Sb12 : Supraconductivité et Corrélations". These de doctorat. Université Joseph Fourier (Grenoble ; 1971-2015).

Melko, Roger G., Byron C. den Hertog, and Michel J. P. Gingras (July 20, 2001). Long-Range Order at Low Temperatures in Dipolar Spin Ice. In: *Physical Review Letters* 87.6. ISSN: 0031-9007, 1079-7114. DOI: 10.1103/PhysRevLett.87.067203.

Mennenga, G., L.J. de Jongh, and W.J. Huiskamp (Sept. 1984). Field Dependent Specific Heat Study of the Dipolar Ising Ferromagnet LiHoF4. In: *Journal of Magnetism and Magnetic Materials* 44.1-2, pp. 59–76. ISSN: 03048853. DOI: 10.1016/0304-8853(84)90047-7.

Michon, Bastien (Oct. 2017). "Point Critique Quantique de La Phase Pseudogap Dans Les Cuprates Supraconducteurs". Institut Néel: Université Grenoble Alpes.

Mizoguchi, Tomonari et al. (Oct. 31, 2018). Magnetic Clustering, Half-Moons, and Shadow Pinch Points as Signals of a Proximate Coulomb Phase in Frustrated Heisenberg Magnets. In: *Physical Review B* 98.14. ISSN: 2469-9950, 2469-9969. DOI: 10.1103/PhysRevB.98.144446.

Moessner, R. and K. S. Raman (Sept. 18, 2008). Quantum Dimer Models. In: *ArXiv08093051 Cond-Mat*. arXiv: 0809.3051 [cond-mat].

Moessner, R. and S. L. Sondhi (Aug. 12, 2003a). Theory of the [111] Magnetization Plateau in Spin Ice. In: *Physical Review B* 68.6, p. 064411. ISSN: 0163-1829, 1095-3795. DOI: 10.1103/PhysRevB.68.064411.

– (Nov. 18, 2003b). Three-Dimensional Resonating-Valence-Bond Liquids and Their Excitations. In: *Physical Review B* 68.18, p. 184512. ISSN: 0163-1829, 1095-3795. DOI: 10.1103/PhysRevB.68.184512.

Moessner, R., S. L. Sondhi, and P. Chandra (Sept. 19, 2001). Phase Diagram of the Hexagonal Lattice Quantum Dimer Model. In: *Physical Review B* 64.14. ISSN: 0163-1829, 1095-3795. DOI: 10.1103/PhysRevB.64.144416.

Moessner, R., S. L. Sondhi, and M. O. Goerbig (Mar. 22, 2006). Quantum Dimer Models and Effective Hamiltonians on the Pyrochlore Lattice. In: *Physical Review B* 73.9, p. 094430. ISSN: 1098-0121, 1550-235X. DOI: 10.1103/PhysRevB.73.094430. arXiv: cond-mat/0508504.

Möller, G. and R. Moessner (Oct. 22, 2009). Magnetic Multipole Analysis of Kagome and Artificial Spin-Ice Dipolar Arrays. In: *Physical Review B* 80.14, p. 140409. ISSN: 1098-0121, 1550-235X. DOI: 10.1103/PhysRevB.80.140409.

Nagle, J. F. (Dec. 22, 2004). Lattice Statistics of Hydrogen Bonded Crystals. I. The Residual Entropy of Ice. In: *Journal of Mathematical Physics* 7.8, p. 1484. ISSN: 0022-2488. DOI: 10.1063/1.1705058.

Nagle, John F. (Dec. 2, 1966). New Series-Expansion Method for the Dimer Problem. In: *Physical Review* 152.1, pp. 190–197. ISSN: 0031-899X. DOI: 10.1103/PhysRev.152.190.

Nilsen, G J et al. (June 2017). Polarisation Analysis on the LET Time-of-Flight Spectrometer. In: *Journal of Physics: Conference Series* 862, p. 012019. ISSN: 1742-6588, 1742-6596. DOI: 10.1088/1742-6596/862/1/012019.

Nisoli, Cristiano (Nov. 1, 2020). The Concept of Spin Ice Graphs and a Field Theory for Their Charges. In: *AIP Advances* 10.11, p. 115102. ISSN: 2158-3226. DOI: 10.1063/5.0010079.

Paddison, Joseph A. M. et al. (Dec. 2016). Emergent Order in the Kagome Ising Magnet Dy3Mg2Sb3O14. In: *Nature Communications* 7.1. ISSN: 2041-1723. DOI: 10.1038/ncomms13842.

Petrenko, O. A., M. R. Lees, and G. Balakrishnan (July 14, 2003). Magnetization Process in the Spin-Ice Compound Ho 2 Ti 2 O 7. In: *Physical Review B* 68.1, p. 012406. ISSN: 0163-1829, 1095-3795. DOI: 10.1103/PhysRevB.68.012406.

Powell, Stephen (Mar. 27, 2015). Ferromagnetic Coulomb Phase in Classical Spin Ice. In: *Physical Review B* 91.9, p. 094431. ISSN: 1098-0121, 1550-235X. DOI: 10.1103/PhysRevB.91.094431.

Raban, V. et al. (June 19, 2019). The Multiple Symmetry Sustaining Phase Transitions of Spin Ice. In: *Physical Review B* 99.22, p. 224425. ISSN: 2469-9950, 2469-9969. DOI: 10.1103/PhysRevB.99.224425. arXiv: 1903.02778.

Raban, Valentin (2018). "Dynamique hors équilibre des monopôles magnétiques dans la glace de spin". ENS de Lyon - Université de Lyon.

Ramirez, A. P. et al. (May 1999). Zero-Point Entropy in 'Spin Ice'. In: *Nature* 399.6734 (6734), pp. 333–335. ISSN: 1476-4687. DOI: 10.1038/20619.

Rams, M. et al. (June 1, 2011). Magnetic Order and Crystal Field in Dy2Ru2O7 and Yb2Ru2O7. In: *Journal of Magnetism and Magnetic Materials* 323.11, pp. 1490–1494. ISSN: 0304-8853. DOI: 10.1016/j.jmmm.2011.01.005.

Rodríguez-Carvajal, Juan (Oct. 1, 1993). Recent Advances in Magnetic Structure Determination by Neutron Powder Diffraction. In: *Physica B: Condensed Matter* 192.1, pp. 55–69. ISSN: 0921-4526. DOI: 10.1016/0921-4526(93)90108-I.

Ryzhkin, I. A. (Sept. 2005). Magnetic Relaxation in Rare-Earth Oxide Pyrochlores. In: *Journal of Experimental and Theoretical Physics* 101.3, pp. 481–486. ISSN: 1063-7761, 1090-6509. DOI: 10.1134/1.2103216.

Sachdev, Subir (Feb. 1995). "Quantum Antiferromagnets in Two Dimensions". In: *Low-Dimensional Quantum Field Theories for Condensed Matter Physicists*. Lecture Notes of ICTP Summer Course. Trieste, Italy: World Scientific, pp. 553–611. ISBN: 978-981-4447-02-7. DOI: 10.1142/9789814447027_0009.

– (2011). *Quantum Phase Transitions*. Second edition. Cambridge ; New York: Cambridge University Press. 501 pp. ISBN: 978-0-521-51468-2.

Savary, Lucile and Leon Balents (Jan. 19, 2012). Coulombic Quantum Liquids in Spin- 1 / 2 Pyrochlores. In: *Physical Review Letters* 108.3. ISSN: 0031-9007, 1079-7114. DOI: 10.1103/PhysRevLett.108.037202.

– (May 22, 2013). Spin Liquid Regimes at Nonzero Temperature in Quantum Spin Ice. In: *Physical Review B* 87.20, p. 205130. DOI: 10.1103/PhysRevB.87.205130.

– (Feb. 23, 2017a). Disorder-Induced Entanglement in Spin Ice Pyrochlores. In: *Physical Review Letters* 118.8, p. 087203. ISSN: 0031-9007, 1079-7114. DOI: 10.1103/PhysRevLett.118.087203. arXiv: 1604.04630.

– (Jan. 1, 2017b). Quantum Spin Liquids: A Review. In: *Reports on Progress in Physics* 80.1, p. 016502. ISSN: 0034-4885, 1361-6633. DOI: 10.1088/0034-4885/80/1/016502.

Schlittler, Thiago M., Rémy Mosseri, and Thomas Barthel (Nov. 21, 2017). Phase Diagram of the Hexagonal Lattice Quantum Dimer Model: Order Parameters, Ground-State Energy, and Gaps. In: *Physical Review B* 96.19, p. 195142. ISSN: 2469-9950, 2469-9969. DOI: 10.1103/PhysRevB.96.195142.

Sibille, Romain et al. (July 2018). Experimental Signatures of Emergent Quantum Electrodynamics in Pr2Hf2O7. In: *Nature Physics* 14.7, pp. 711–715. ISSN: 1745-2473, 1745-2481. DOI: 10.1038/s41567-018-0116-x.

Sikora, Olga et al. (Sept. 21, 2011). Extended Quantum U (1) -Liquid Phase in a Three-Dimensional Quantum Dimer Model. In: *Physical Review B* 84.11. ISSN: 1098-0121, 1550-235X. DOI: 10.1103/PhysRevB.84.115129.

Singh, Rajiv R. P. and David A. Huse (Mar. 16, 1992). Three-Sublattice Order in Triangular- and Kagomé-lattice Spin-Half Antiferromagnets. In: *Physical Review Letters* 68.11, pp. 1766–1769. ISSN: 0031-9007. DOI: 10.1103/PhysRevLett.68.1766.

Spaldin, Nicola A, Manfred Fiebig, and Maxim Mostovoy (Oct. 29, 2008). The Toroidal Moment in Condensed-Matter Physics and Its Relation to the Magnetoelectric Effect. In: *Journal of Physics: Condensed Matter* 20.43, p. 434203. ISSN: 0953-8984, 1361-648X. DOI: 10.1088/0953-8984/20/43/434203.

Tabata, Y. et al. (Dec. 21, 2006). Kagom\'{e} Ice State in the Dipolar Spin Ice Dy$_{2}$Ti$_{2}$O$_{7}$. In: *Physical Review Letters* 97.25, p. 257205. ISSN: 0031-9007, 1079-7114. DOI: 10.1103/PhysRevLett.97.257205. arXiv: cond-mat/0607808.

Toews, W. H. et al. (May 23, 2013). Thermal Conductivity of Ho 2 Ti 2 O 7 along the [111] Direction. In: *Physical Review Letters* 110.21, p. 217209. ISSN: 0031-9007, 1079-7114. DOI: 10.1103/PhysRevLett.110.217209.

Tomasello, Bruno et al. (Oct. 12, 2015). Single-Ion Anisotropy and Magnetic Field Response in the Spin-Ice Materials Ho 2 Ti 2 O 7 and Dy 2 Ti 2 O 7. In: *Physical Review B* 92.15, p. 155120. ISSN: 1098-0121, 1550-235X. DOI: 10.1103/PhysRevB.92.155120.

– (Aug. 2019). Correlated Quantum Tunneling of Monopoles in Spin Ice. In: *Physical Review Letters* 123.6, p. 067204. DOI: 10.1103/PhysRevLett.123.067204.

Turrini, A. A. et al. (Mar. 2, 2022). Tunable Critical Correlations in Kagome Ice. In: *Physical Review B* 105.9, p. 094403. ISSN: 2469-9950, 2469-9969. DOI: 10.1103/PhysRevB.105.094403.

Udagawa, M. et al. (Sept. 15, 2016). Out-of-Equilibrium Dynamics and Extended Textures of Topological Defects in Spin Ice. In: *Physical Review B* 94.10, p. 104416. ISSN: 2469-9950, 2469-9969. DOI: 10.1103/PhysRevB.94.104416.

Udagawa, Masafumi and Ludovic Jaubert, eds. (2021). *Spin Ice*. Vol. 197. Springer Series in Solid-State Sciences. Cham: Springer International Publishing. ISBN: 978-3-030-70860-3. DOI: 10.1007/978-3-030-70860-3.

Wales, David and Jonathan Doye (July 1, 1997). Global Optimization by Basin-Hopping and the Lowest Energy Structures of Lennard-Jones Clusters Containing up to 110 Atoms. In: *The Journal of Physical Chemistry A* 101.28, pp. 5111–5116. ISSN: 1089-5639, 1520-5215. DOI: 10.1021/jp970984n. arXiv: cond-mat/9803344.

Wang, Yishu et al. (June 18, 2021). Monopolar and Dipolar Relaxation in Spin Ice Ho $_2$ Ti $_2$ O $_7$. In: *Science Advances* 7.25, eabg0908. ISSN: 2375-2548. DOI: 10.1126/sciadv.abg0908.

Wen, Xiao-Gang (Dec. 4, 2017). Zoo of Quantum-Topological Phases of Matter. In: *Reviews of Modern Physics* 89.4, p. 041004. ISSN: 0034-6861, 1539-0756. DOI: 10.1103/RevModPhys.89.041004. arXiv: 1610.03911.

Wiebe, C. et al. (Aug. 2004). Magnetic Ordering in the Spin-Ice Candidate Ho2Ru2O7. In: *Physical Review Letters* 93.7, p. 076403. ISSN: 0031-9007, 1079-7114. DOI: 10.1103/PhysRevLett.93.076403.

Yan, Han et al. (Mar. 17, 2017). Theory of Multiple-Phase Competition in Pyrochlore Magnets with Anisotropic Exchange with Application to Yb 2 Ti 2 O 7 , Er 2 Ti 2 O 7 , and Er 2 Sn 2 O 7. In: *Physical Review B* 95.9. ISSN: 2469-9950, 2469-9969. DOI: 10.1103/PhysRevB.95.094422.

Yoshida, Shun-ichi, Koji Nemoto, and Koh Wada (July 15, 2004). Ordered Phase of Dipolar Spin Ice under [110] Magnetic Field. In: *Journal of the Physical Society of Japan* 73.7, pp. 1619–1622. ISSN: 0031-9015, 1347-4073. DOI: 10.1143/JPSJ.73.1619.